A Wall Model for Large-Eddy Simulation of Compressible Channel Flows

Barrett T. McCann

A thesis submitted in partial fulfillment of the requirements for the degree of

Doctor of Philosophy in Aeronautics & Astronautics

University of Washington

2014

Reading Committee:

Antonino Ferrante

Dana Dabiri

James Riley

Program Authorized to Offer Degree:
Aeronautics & Astronautics

University of Washington

Abstract

A Wall Model for Large-Eddy Simulation of Compressible Channel Flows

Barrett T. McCann

Chair of the Supervisory Committee:
Assistant Professor Antonino Ferrante
Aeronautics & Astronautics

A wall model for the large-eddy simulation (LES) of compressible channel flows with isothermal walls is presented, which extends the incompressible model of Chung and Pullin (*Journal of Fluid Mechanics*, 2009). The wall model computes the local, instantaneous wall shear stress and heat flux, which are then applied as wall boundary conditions, by solving two time-dependent, parameter-free ordinary differential equations (ODEs) at each time step. These ODEs are obtained by integrating the LES momentum and internal energy equations in the wall-normal direction from the wall to the first grid point placed in the log layer. In contrast to so-called wall-resolved LES, employment of this wall model allows use of relatively coarse computational meshes of fixed size, independent of Reynolds number. The wall model is first validated by comparing the LES results at $M = 0.15$ and $Re_\tau = 2003$ to the direct numerical simulation (DNS) results of Hoyas and Jiménez (*Physics of Fluids*, 2006), and at $M = 0.7$ and $Re_\tau = 186$ to the DNS results of Wei and Pollard (*Computers & Fluids*, 2011). Results are then presented for LES of channel flows at $M = 0.15$ and $M = 0.7$, over a three-order-of-magnitude range of friction Reynolds numbers, on a uniform mesh with $256 \times 32 \times 128$ grid points in the streamwise, wall-normal, and spanwise directions.

TABLE OF CONTENTS

Page

List of Figures iii

List of Tables vi

Chapter 1: Introduction and Background 1
1.1 The Energy Cascade in Turbulence 1
1.2 Turbulence Modeling and Simulation 2
1.2.1 Reynolds-Averaged Navier–Stokes Methods 2
1.2.2 Direct Numerical Simulation 4
1.2.3 Large-Eddy Simulation 5
1.3 Fully Developed Turbulent Channel Flows 5
1.3.1 Incompressible Turbulent Channel Flows 6
1.3.2 Compressible Turbulent Channel Flows 7
1.4 LES of Wall-Bounded Turbulent Flows 8

Chapter 2: Mathematical Formulation 10
2.1 LES Equations 10
2.1.1 Continuity Equation 10
2.1.2 Momentum Equation 11
2.1.3 Internal Energy Equation 11
2.2 Subgrid-Scale Turbulence Models 13
2.2.1 The Smagorinsky Model 13
2.2.2 Lundgren's strained spiral vortex model of fine turbulence . . 14
2.2.3 A stretched vortex-based LES subgrid-scale model 16
2.3 LES Wall Modeling 17
2.3.1 Wall Model of Pantano et al. (2008) 18
2.3.2 Wall Model of Chung and Pullin (2009) 18

2.3.3 Present Wall Model for LES of Compressible Channel Flows . 22
2.4 Numerical Method 39
2.4.1 Initial Conditions 39
2.4.2 Boundary Conditions 41
2.4.3 Simulation Conditions 44

Chapter 3: Results 46
3.1 LES of Low-Mach Number Channel Flow Using Pantano et al. Wall Model 46
3.2 LES of Low-Mach Number Channel Flow Using Chung and Pullin Wall Model 49
3.2.1 Computational Details 49
3.2.2 Results 51
3.3 LES of Low-Mach Number Channel Flow Using the Present Wall Model 56
3.4 LES of Compressible Channel Flow at M = 0.7 Using the New Wall Model 64

Chapter 4: Conclusions and Recommendations for Future Research 71
4.1 Summary of Research 71
4.2 Recommendations 73

Bibliography 77

LIST OF FIGURES

Figure Number — Page

2.1 Selected orientation of the coordinate axis system 17

2.2 Temperature profiles, mean (—) and fluctuating (– –) components: (a) $M = 1.5$, (b) $M = 3$. (Reproduced from Fig. 4 in Huang, Coleman and Bradshaw, 1995 [31].) 24

2.3 Initial conditions: mean profiles (•) with minimum and maximum perturbations (+), for $\tilde{u}$, $\tilde{v}$ and $\tilde{w}$ 40

2.4 Initial condition: contours of resolved streamwise velocity $\tilde{u}/U_{center}$ in the horizontal plane $y = \Delta y/2$ 41

2.5 Temperature histories over 40 flow-throughs: one bottom wall-adjacent cell (red) and one top wall-adjacent cell (blue), $M = 0.15$, adiabatic-wall boundary condition 43

2.6 Temperature histories over 40 flow-throughs: one bottom wall-adjacent cell (red) and one top wall-adjacent cell (blue), $M = 0.15$, isothermal-wall boundary condition 43

2.7 Specification of ghost-cell properties to apply boundary conditions . . 44

3.1 $M = 0.15$, $Re_\tau = 2003$ mean velocity profile of the baseline LES using the wall model of Pantano et al., 2008 [21], described in Sec. 2.3.1 (∘), compared with the incompressible DNS results of Hoyas and Jiménez, 2006 [9] (—) 47

3.2 $M = 0.15$, $Re_\tau = 2003$ turbulent statistics of the baseline LES using the wall model of Pantano et al., 2008 [21], described in Sec. 2.3.1, compared with the incompressible DNS results of Hoyas and Jiménez, 2006 [9]: (a) streamwise intensity; (b) wall-normal intensity; (c) spanwise intensity; (d) Reynolds shear stress (∘ total, □ subgrid, — DNS) 48

3.3 $M = 0.15$, $Re_\tau = 2003$ turbulence kinetic energy profile of the baseline LES using the wall model of Pantano et al., 2008 [21], described in Sec. 2.3.1, compared with the incompressible DNS results of Hoyas and Jiménez, 2006 [9] (∘ resolved, □ subgrid, ⋄ total, — DNS) 49

3.4 $M = 0.15$, $Re_\tau = 2003$ mean velocity profile of the LES using the wall model of Chung and Pullin, 2009 [1], described in Sec. 2.3.2 (∘), compared with the incompressible DNS results of Hoyas and Jiménez, 2006 [9] (—) 52

3.5 $M = 0.15$, $Re_\tau = 2003$ turbulent statistics of the LES using the wall model of Chung and Pullin, 2009 [1], described in Sec. 2.3.2, compared with the incompressible DNS results of Hoyas and Jiménez, 2006 [9]: (a) streamwise intensity; (b) wall-normal intensity; (c) spanwise intensity; (d) Reynolds shear stress (∘ total, □ subgrid, — DNS) 53

3.6 $M = 0.15$, $Re_\tau = 2003$ turbulence kinetic energy profile of the LES using the wall model of Chung and Pullin, 2009 [1], described in Sec. 2.3.2, compared with the incompressible DNS results of Hoyas and Jiménez, 2006 [9] (∘ resolved, □ subgrid, ⋄ total, — DNS) 54

3.7 Mean velocity profiles for LES using the wall model of Chung and Pullin [1] in AMROC, Re_τ spanning three orders of magnitude 55

3.8 $M = 0.15$, $Re_\tau = 2003$ mean velocity profile using the compressible wall model (∘), compared with the LES of Chung and Pullin [1] (△) and the DNS of Hoyas and Jiménez [9] (—) 57

3.9 $M = 0.15$, $Re_\tau = 2003$ turbulent statistics using the compressible wall model, compared with the LES of Chung and Pullin [1] and the incompressible DNS of Hoyas and Jiménez [9]: (a) streamwise intensity; (b) wall-normal intensity; (c) spanwise intensity; (d) Reynolds shear stress (∘ total, □ subgrid, △ Chung and Pullin, — DNS) 58

3.10 $M = 0.15$, $Re_\tau = 2003$ mean turbulence kinetic energy profile using the compressible wall model, compared with the incompressible DNS results of Hoyas and Jiménez [9] (∘ resolved, □ subgrid, ⋄ total, — DNS) 59

3.11 $M = 0.15$, $Re_\tau = 2003$ mean rates of (a) production and (b) dissipation of turbulence kinetic energy using the compressible wall model, compared with the incompressible DNS results of Hoyas and Jiménez [9] (△ production, ∘ resolved dissipation, □ subgrid dissipation, ⋄ total dissipation, — DNS) 60

3.12 $M = 0.15$ mean velocity profiles using the compressible wall model (□ $Re_\tau = 2003$, ⋄ $Re_\tau = 2 \times 10^4$, △ $Re_\tau = 2 \times 10^5$, ∘ $Re_\tau = 2 \times 10^6$, — log law, $\kappa = 0.4$, $B = 5$) 61

3.13 $M = 0.15$ turbulent statistics using the compressible wall model: (a) streamwise intensity; (b) wall-normal intensity; (c) spanwise intensity; (d) Reynolds shear stress ($\square$ $Re_\tau = 2003$, $\diamond$ $Re_\tau = 2 \times 10^4$, $\triangle$ $Re_\tau = 2 \times 10^5$, $\circ$ $Re_\tau = 2 \times 10^6$, — incompressible DNS $Re_\tau = 2003$ [9]) . . 62

3.14 $M = 0.15$ mean turbulence kinetic energy profiles using the compressible wall model ($\square$ $Re_\tau = 2003$, $\diamond$ $Re_\tau = 2 \times 10^4$, $\triangle$ $Re_\tau = 2 \times 10^5$, $\circ$ $Re_\tau = 2 \times 10^6$, — incompressible DNS $Re_\tau = 2003$ [9]) 63

3.15 (a) Mean pressure and (b) pressure fluctuation profiles of the LES at $M = 0.7$, $Re_\tau = 186$ 65

3.16 Temperature histories over 40 flow-throughs: one bottom wall-adjacent cell (red) and one top wall-adjacent cell (blue), $M = 0.7$, $Re_\tau = 186$, isothermal wall boundary condition 66

3.17 $M = 0.7$, $Re_\tau = 186$ mean velocity profile using the compressible wall model ($\circ$), compared with the DNS results of Wei and Pollard, 2011 [37] (—) 66

3.18 $M = 0.7$, $Re_\tau = 186$ turbulent statistics using the compressible wall model, compared with the DNS results of Wei and Pollard, 2011 [37]: (a) mean Mach number ($\circ$ LES, — DNS); (b) streamwise turbulent intensity ($\circ$ total, $\square$ subgrid, — DNS); (c) Reynolds shear stress ($\circ$ total, $\square$ subgrid, — DNS); (d) turbulence kinetic energy ($\diamond$ resolved, $\square$ subgrid, $\circ$ total, — DNS) 68

3.19 $M = 0.7$, $Re_\tau = 186$ mean profiles of pressure (top), density (middle) and temperature (bottom), LES using the compressible wall model ($\circ$) compared with the DNS results of Wei and Pollard, 2011 [37] (—) . . 69

3.20 $M = 0.7$ turbulent statistics using the compressible wall model: (a) mean velocity profiles; (b) streamwise turbulent intensity; (c) Reynolds shear stress; (d) turbulence kinetic energy ($\square$ $Re_\tau = 186$, $\diamond$ $Re_\tau = 2 \times 10^3$, $\triangle$ $Re_\tau = 2 \times 10^4$, $\circ$ $Re_\tau = 2 \times 10^5$, — compressible log law, - - - DNS $Re_\tau = 186$ [37]) 70

LIST OF TABLES

Table Number Page

2.1 Orders of magnitude of right-hand side terms in Eq. 2.97 39

3.1 Run parameters of the $M = 0.15$ LES 56

3.2 Run parameters of the $M = 0.7$ LES 64

ACKNOWLEDGMENTS

I would like to thank my research advisor, Professor Antonino Ferrante, for his active involvement in and continual discussions concerning this research program. His time spent collaborating, brainstorming, explaining, advising, challenging, demanding and encouraging were essential; I could not have completed this dissertation without his constant guidance. I also want to thank the other members of the Computational Fluid Mechanics group, especially Hezky, Eric, Keegan and Chris, for lending a hand whenever I asked; I hope I was able to do the same for you.

I am especially grateful to Professor Carlos Pantano at UIUC for his many fruitful (and patient) exchanges regarding the use and performance of AMROC, and for providing access to the latest version of the code. I learned much about turbulent flows, not just how to use the code, from our conversations.

I am grateful to Professor Dale Pullin at Caltech, and Dr. Daniel Chung, formerly at GALCIT, for clearly and kindly answering all my questions about their novel wall model. I enjoyed the opportunity to meet Prof. Pullin and briefly discuss my research; his encouragement was helpful.

I am also grateful to Professor Andrew Pollard at Queen's University at Kingston and to Dr. Liang Wei at Iowa State, who kindly (and promptly!) provided detailed profiles from their direct numerical simulations. They provided necessary results for validating my wall model.

This material is based upon work supported by the National Science Foundation Graduate Research Fellowship Program under Grant No. DGE-0718124 and by the U.S. Air Force Institute of Technology.

This work was facilitated through the use of advanced computational, storage, and networking infrastructure provided by the Hyak supercomputer system at the University of Washington.

DEDICATION

At long last, this dissertation is dedicated to Hollyann, Andrew and Hannah, three great kids who make every day a "fun adventure." Mostly to Suzann, my wife, partner, love of my life and best friend, who always knew I'd succeed, even when I fretted—early mornings and late nights—that I'd never get it to work. To Mom, Dad, Verla and Harv, who were unflagging in their encouragement; I'm sorry I was so frequently reluctant to discuss my progress (or seeming lack thereof). To Mark, Matt, Steve, and all the Northshore guys for your prayers and friendship—let's go on a hike as soon as the snow melts. And to my heavenly Father, from whom come all good gifts, including (some degree of) ability, energy, insight, perseverence, and maybe even wisdom. Thank you for my amazing family, my friends, my career, and all the great experiences you've blessed us with.

Chapter 1
INTRODUCTION AND BACKGROUND

This thesis describes a wall model for the large-eddy simulation (LES) of compressible, fully developed, turbulent channel flows. This appears to be the first wall model for LES of compressible channel flows without resolving the near-wall region. The wall model was inspired by the incompressible model of Chung and Pullin [1], and is parameter-free—that is, it uses no empirically derived constants. T. S. Lundgren's strained spiral vortex model of small turbulence scales [2] is used as the LES subgrid-scale model and as input to the wall model. In contrast to so-called "resolved" LES, the new wall model allows the use of relatively coarse grids of fixed size (as few as 32 grid points across the channel height) across a three-order-of-magnitude range of Reynolds numbers. The derivation of the wall model and its application to LES of compressible channel flows are described.

1.1 The Energy Cascade in Turbulence

Lewis F. Richardson first expressed the concept of a turbulent energy cascade in 1922 [3], poetically summarizing by, "We realize thus that: big whirls have little whirls that feed on their velocity, and little whirls have lesser whirls and so on to viscosity—in the molecular sense" [4]. In other words, kinetic energy is transferred locally from larger turbulent eddies to successively smaller eddies until, at the smallest turbulence scales, it is dissipated as heat. Andrey Kolmogorov quantified this process in 1941, determining the small scales at which the viscous dissipation occurs and the dependence on Reynolds number of the range of eddy scales. A key result of Kolmogorov's theory concerns the ratio of the length scale of the smallest turbulent

eddies, η, to the scale of the largest eddies, l_0: $\eta/l_0 \sim Re^{-3/4}$. That is, whereas the length scale of the largest eddies is comparable to the characteristic length of the flow geometry, the length scale of the smallest eddies becomes exponentially smaller with increasing Reynolds number [3]. This result has a direct bearing on the grid resolution requirements for detailed numerical simulations of turbulence.

Kolmogorov used a dimensional argument to predict a turbulence energy spectrum. In the inertial subrange—that is, in the range of turbulence scales smaller than the scales of the anisotropic, energy-containing eddies, and larger than the small scales at which viscous dissipation occurs—the energy spectrum is of the form

$$E(\kappa) = C\varepsilon^{2/3}\kappa^{-5/3} \tag{1.1}$$

where $\int_0^\infty E(\kappa)d\kappa$ is the the turbulence kinetic energy, κ the wavenumber, ε the rate of dissipation of turbulence kinetic energy, and C the Kolmogorov constant [3]. Although the Kolmogorov spectrum has not been derived from first principles (i.e., the Navier–Stokes equations), it has been verified experimentally [2]. Numerical models of turbulence, then, are informed by the energy cascade and Kolmogorov spectrum, and their performance judged by their ability to predict these physical results.

1.2 Turbulence Modeling and Simulation

There are three main techniques for numerical modeling and simulation of turbulent flows: Reynolds-averaged Navier-Stokes (RANS), direct numerical simulation (DNS), and large-eddy simulation (LES). A hybrid technique, detached-eddy simulation (DES), combines characteristics of LES and RANS.

1.2.1 Reynolds-Averaged Navier–Stokes Methods

RANS methods calculate the unsteady behavior of the mean flow by solving the Reynolds equations. These equations employ the Reynolds decomposition of the

velocity field $\mathbf{U}(\mathbf{x},t)$ into the mean field $\langle\mathbf{U}(\mathbf{x},t)\rangle$ and the fluctuating field $\mathbf{u}(\mathbf{x},t)$:

$$\mathbf{U}(\mathbf{x},t) = \langle\mathbf{U}(\mathbf{x},t)\rangle + \mathbf{u}(\mathbf{x},t) \tag{1.2}$$

where $\langle\ \rangle$ is a time average over a period of time that is large compared to the period of the turbulent fluctuations. To provide a brief example, the incompressible Reynolds equations describing mass and momentum conservation are

$$\nabla \cdot \langle\mathbf{U}\rangle = 0 \tag{1.3}$$

and

$$\frac{\bar{D}\langle U_i\rangle}{\bar{D}t} = -\frac{1}{\rho}\frac{\partial\langle p\rangle}{\partial x_i} + \nu\frac{\partial^2\langle U_i\rangle}{\partial x_j \partial x_j} - \frac{\partial\langle u_i u_j\rangle}{\partial x_j}. \tag{1.4}$$

where the fluid density ρ and kinematic viscosity ν are constant, body forces have been neglected, and the mean material derivative $\bar{D}(\ )/\bar{D}t \equiv \partial(\ )/\partial t + \langle\mathbf{U}\rangle \cdot \nabla(\ )$ indicates the rate of change of a property of a fluid element convected by the mean velocity [3]. These RANS equations are identical in form to the full continuity and momentum (Navier–Stokes) equations,

$$\nabla \cdot \mathbf{U} = 0 \tag{1.5}$$

and

$$\frac{DU_i}{Dt} = -\frac{1}{\rho}\frac{\partial p}{\partial x_i} + \nu\frac{\partial^2 U_i}{\partial x_j \partial x_j}, \tag{1.6}$$

except for the presence of an additional term containing the so-called Reynolds stresses, $\langle u_i u_j\rangle$. The RANS method seeks to numerically solve equations 1.3 and 1.4 for the mean velocity and pressure fields, but the Reynolds stress term presents a closure problem: this additional term, for which no exact physical description is available, must be modeled in order to close the system of equations. Popular approaches to modeling the Reynolds stresses include using a turbulent viscosity model, or solving a transport equation for the Reynolds stresses in order to close the system of equations. Descriptions of these classes of Reynolds stress models can be found in many fluid mechanics textbooks (see, e.g., [5] and [3]).

Because RANS methods do not attempt to resolve the turbulent fluctuations, with their wide range of length and time scales, these methods are computationally efficient (i.e., they can employ relatively coarse grids and large time steps) and can be used to simulate high-Reynolds-number flows about complex geometries. Unfortunately, however, since they do not calculate the unsteady turbulent behavior, they are unable to provide any detailed information about the turbulence in the flow and, as a result, are known to generally perform poorly in predicting such phenomena as unsteady flow separation. Additionally, RANS methods lack generality, and typically must be calibrated (by experimental results, for example) for a specific type of application or class of flow geometries [6].

1.2.2 Direct Numerical Simulation

At the other end of the range of numerical techniques for predicting turbulent flows is direct numerical simulation. In DNS, the Navier-Stokes equations are solved numerically, using a computational mesh and time step fine enough to resolve all turbulence scales in space and time, respectively. Thus, the instantaneous velocity field is calculated, from which turbulent statistics can be determined, and complete flow visualization performed. DNS is being used successfully for turbulence phenomenological research, and knowledge of turbulence behavior has been gained that could not be acquired via experimental techniques [3].

Unfortunately, as the mesh size requirement of DNS increases as $Re^{9/4}$ (Reynolds number based on characteristic length and velocity scales of the large eddies)—recall Kolmogorov's η/l_0 relationship from the previous section—and overall computational cost increases as Re^3, the technique will be limited for the foreseeable future to fairly simple flows at low-to-moderate Reynolds numbers [7, 3, 8]. For example, the DNS of fully developed, incompressible, turbulent channel flow by Hoyas and Jiménez, at a moderate Reynolds number (based on channel half-height δ and bulk velocity $\bar{U}$) $Re = 2\delta\bar{U}/\nu = 87,180$, required nearly *18 billion* computational cells and 6 million

processor hours—that is, some four months on 2048 processors [9]. Even assuming that advancement in computer processing speed and storage capacity (memory) continues on its current pace, it has been estimated that DNS will not be a practical design tool, capable of full aircraft simulations at flight Reynolds numbers, until approximately 2070 [10].

1.2.3 Large-Eddy Simulation

Large-eddy simulation lies between RANS and DNS. LES simulates a turbulent flow on a mesh fine enough to directly resolve the larger turbulent motions, but too coarse to resolve the smaller-scale turbulence; thus, the effects of the smaller turbulence scales must be modeled [1]. Because the large-scale motions are resolved, LES can be expected to predict unsteady turbulence phenomena better than can RANS. But because much of the computational cost of DNS is due to the calculation of the smallest turbulence scales, which are not resolved in large-eddy simulations, LES can significantly improve on the challenging mesh size and time step requirements of DNS, making simulation of higher Reynolds number flows more feasible.

The foundational work in large-eddy simulation was performed for meteorological applications, beginning in 1963 with Joseph Smagorinsky, who used large-eddy concepts to simulate the circulation of the earth's atmosphere [11]. James Deardorff first applied LES to high-Reynolds number turbulent channel flow in 1970; applying the law of the wall to model near-wall subgrid-scale (sgs) turbulence, and using a 6720-cell grid, his simulation exhibited streamwise elongation of eddies and the frequent appearance of helical vortices which transported momentum toward the wall, although its velocity profiles did not compare well with experimental data [12].

1.3 Fully Developed Turbulent Channel Flows

The present research considers channel flow, in which a streamwise (negative) pressure gradient drives the flow. The channel's streamwise and spanwise dimensions, L_x and

L_z, respectively, are large compared to the channel height $L_y = 2\delta$, and the fully developed region far from the channel entrance is considered. Thus, mean velocities are invariant in x and z—that is, the flow is statistically one-dimensional in y. Such flows are fully turbulent for Reynolds numbers $Re \equiv 2\delta\bar{U}/\nu > 1800$, where

$$\bar{U} \equiv \frac{1}{2\delta}\int_0^{2\delta} \langle U \rangle \, dy$$

is the bulk velocity [3].

1.3.1 Incompressible Turbulent Channel Flows

From the mean (Reynolds) equations for incompressible turbulent flows, and application of the no-slip condition $\mathbf{U}_{y=0} = \mathbf{U}_{y=2\delta} = 0$, it can be shown that the mean velocity profile is a function of flow density ρ and kinematic viscosity ν, the channel height, and the friction velocity $u_\tau \equiv \sqrt{\tau_w/\rho}$ only, where $\tau_w \equiv \rho\nu \left(d\langle U \rangle/dy\right)_{y=0}$ is the shear stress at the wall. Ludwig Prandtl theorized the presence of a near-wall inner layer, $y/\delta \lesssim 0.1$, in which the mean velocity profile is a function of only the viscous velocity scale u_τ and the viscous lengthscale $\delta_\nu \equiv \nu\sqrt{\rho/\tau_w} = \nu/u_\tau$ (and is thus independent of such overall flow parameters as channel height and centerline velocity). A consequence is that, near the wall, the normalized mean streamwise velocity, $\langle U \rangle^+ \equiv \langle U \rangle/u_\tau$, is a function only of the normalized distance from the wall, $y^+ \equiv y/\delta_\nu$. For small y^+ (recalling again that $\mathbf{U}_{y=0} = 0$), the relation is simply

$$\langle U \rangle^+ = y^+ + \mathcal{O}\left(y^{+4}\right), \tag{1.7}$$

and DNS confirms the validity of the relation $\langle U \rangle^+ \approx y^+$ for $y^+ \lesssim 5$, the viscous sublayer [3].

Within the inner layer but farther from the wall, however, the effect of viscosity diminishes, and the relation becomes logarithmic [13]:

$$\langle U \rangle^+ = \frac{1}{\kappa}\ln y^+ + B \tag{1.8}$$

where κ is called the von Kármán constant and B is a constant intercept; empirically derived values are $\kappa \approx 0.41$ and $B \approx 5$. DNS shows good agreement for $y^+ \gtrsim 30$ [3]. Equations 1.7 and 1.8 comprise the so-called "law of the wall." Between the viscous sublayer and the log-law region is a buffer layer, within which the mean velocity profile is observed to transition smoothly from Eq. 1.7 to Eq. 1.8; the two curves intersect at $y^+ \approx 11$ (although neither 1.7 nor 1.8 correctly predicts u^+ near $y^+ = 11$).

1.3.2 Compressible Turbulent Channel Flows

Understanding and predicting compressible, turbulent, wall-bounded flows is important in many practical engineering applications. As one example, the standard propulsion text of Hill and Peterson, *Mechanics and Thermodynamics of Propulsion*, points out that gas-turbine engine inlets are typically designed to deliver flow to the compressor face in the Mach number range $0.4 \leq M \leq 0.6$ [14]. But in contrast to incompressible, turbulent, wall-bounded flows, for which theory, supplemented by experimental and numerical study, provides insight into many important phenomena, "[t]here is still no universal theory for wall-bounded compressible turbulent flow. Consequently, understanding has usually been obtained from comparison with the incompressible case, for instance the Van Driest transformation" [15]. E. R. Van Driest in 1951 developed a law-of-the-wall transformation for compressible flows, applying Prandtl's mixing length hypothesis to compressible flows. The mixing length concept supposes that the Reynolds stress is proportional to the velocity gradient via a "turbulent viscosity" (or "eddy viscosity") coefficient, $-\rho\langle uv\rangle = \mu_t \left(\partial\langle U\rangle/\partial y\right)$, where, in an analogy to molecular viscosity, μ_t is assumed to be a product of density, a turbulence velocity scale, and a length scale: $\mu_t = \rho u_t l_m$; in the log-law region, the mixing length $l_m = \kappa y$. Additionally, the turbulent velocity scale is assumed to be a product of the mixing length and the velocity gradient, $u_t = l_m \left(\partial\langle U\rangle/\partial y\right)$. With these ideas, combined with a Mach number-dependent temperature-velocity relationship for Prandtl numbers near unity, Van Driest developed a velocity profile transformation

of the form

$$\frac{\langle U^* \rangle}{u_\tau} = \frac{1}{\kappa} \ln \frac{y u_\tau}{\nu_w} + F \tag{1.9}$$

(where U^* is the transformed streamwise velocity, ν_w is the kinematic viscosity at the wall, and F is an intercept), which matches the log law, Eq. 1.8 [16, 17]. Velocity profile measurements in turbulent boundary layers at Mach numbers 4.47, 4.50 and 7.20 and three different Reynolds numbers, when transformed via Eq. 1.9, collapse onto the log law in the inner layer [17]. The Van Driest transformation is here utilized to create the initial conditions for the LES of compressible channel flows, as described in section 2.3.3.

Isothermal Walls

It is noted that achievement of a fully developed, compressible channel flow requires the use of isothermal (cooled) walls because, at compressible Mach numbers, high rates of viscous dissipation of turbulence kinetic energy occur near the walls [17, 15]. Use of adiabatic walls, then, would cause the temperature in the channel to continually rise over time. The development and implementation of the compressible wall model in the present research simulates cooled walls to achieve statistically stationary flow conditions.

1.4 LES of Wall-Bounded Turbulent Flows

The key underlying assumption of LES is that only the large turbulent eddies, which contain most of the turbulence kinetic energy and are primarily responsible for the transfer of mass and momentum, are affected by the flow geometry; whereas small-scale turbulence is universal and can be modeled. This is a reasonable assumption for free shear flows, for example. But for wall-bounded flows, there are no "large" eddies near the wall; here, small-scale eddies carry the turbulence kinetic energy and accomplish momentum transfer. Thus, the underlying assumption fails close to the

wall [1, 18].

Use of a near-wall mesh fine enough to resolve the momentum transfer behavior and most (say, 80%) of the turbulence kinetic energy—large-eddy simulation with near-wall resolution (LES–NWR), in the terminology of Pope [3]—would impose a mesh resolution requirement nearly as restrictive as DNS, with mesh size increasing as $Re^{9/5}$ at low to intermediate Reynolds numbers, and as $Re^{13/7}$ at high Reynolds numbers [8]. Thus, LES–NWR will remain impractical for high-Reynolds number flows for all but the simplest geometries for many years to come. The alternative is large-eddy simulation with near-wall modeling (LES–NWM), where no attempt is made to resolve the turbulent eddies in the thin near-wall region, relying instead purely on a wall model—the quality of which can be expected to have a significant effect on the accuracy of the simulation [18]. The benefit is the ability to use mesh sizes that scale with the flow geometry, weakly dependent on or potentially independent of Reynolds number—an attractive feature [1].

For these reasons, the present research employs LES–NWM, proposing and applying a novel compressible-flow wall model. This compressible wall model will be shown to work well on a relatively coarse mesh of fixed size, over a range of Reynolds numbers. Here, the model is implemented in a finite-difference LES code and applied to simulations of fully developed, compressible channel flows with isothermal walls.

The following chapter will derive the LES governing equations; briefly describe Lundgren's stretched-vortex fine turbulence model [2] and an LES subgrid-scale model based upon it [19]–[20]; describe a log law-based LES wall treatment used successfully by Pantano et al. [21]; summarize the development of the incompressible wall model of Chung and Pullin [1]; and describe the present wall model for application to compressible wall-bounded flows. Later chapters will report the results of large-eddy simulations of $M = 0.15$ and $M = 0.7$ channel flows and evaluate the effectiveness of the new wall model (chapter 3), and recommend future research (chapter 4).

Chapter 2

MATHEMATICAL FORMULATION

2.1 LES Equations

In large-eddy simulation, the flow field variables are low-pass filtered to remove the small-scale turbulence and allow use of a relatively coarse grid. Such a filtered quantity is denoted by an overbar:

$$\bar{f} = \int_D G\left(\mathbf{x} - \mathbf{x}'\right) f\left(\mathbf{x}'\right) d\mathbf{x}' \tag{2.1}$$

where G is a spatial filter and D the flow domain. A flow variable, such as velocity $\mathbf{u}$, can then be decomposed into a resolved component $\bar{\mathbf{u}}$ and a subgrid-scale component $\mathbf{u}'$: $\mathbf{u}(\mathbf{x},t) = \bar{\mathbf{u}}(\mathbf{x},t) + \mathbf{u}'(\mathbf{x},t)$.

2.1.1 Continuity Equation

The continuity (mass conservation) equation for compressible flows is

$$\frac{\partial \rho}{\partial t} + \frac{\partial\left(\rho u_k\right)}{\partial x_k} = 0, \tag{2.2}$$

where ρ is the density and u_k the velocity component in the x_k direction. Filtering Equation 2.2 using Eq. 2.1 gives

$$\frac{\partial \bar{\rho}}{\partial t} + \frac{\partial \overline{\rho u_k}}{\partial x_k} = 0. \tag{2.3}$$

In LES of compressible flows, it is convenient to employ the Favre filter (or density weighting) $\tilde{f} = \overline{\rho f}/\bar{\rho}$. Using $\tilde{u}_k = \overline{\rho u_k}/\bar{\rho}$, Eq. 2.3 becomes

$$\frac{\partial \bar{\rho}}{\partial t} + \frac{\partial\left(\bar{\rho}\tilde{u}_k\right)}{\partial x_k} = 0. \tag{2.4}$$

2.1.2 Momentum Equation

The Navier–Stokes (or momentum conservation) equation for compressible flows is

$$\frac{\partial(\rho u_i)}{\partial t} + \frac{\partial(\rho u_i u_k)}{\partial x_k} = -\frac{\partial p}{\partial x_i} + \frac{\partial \sigma_{ik}}{\partial x_k} \tag{2.5}$$

where p is the dynamic pressure field, and the viscous stresses are

$$\sigma_{ik} = \mu\left(\frac{\partial u_i}{\partial x_k} + \frac{\partial u_k}{\partial x_i}\right) - \frac{2}{3}\mu\frac{\partial u_j}{\partial x_j}\delta_{ik}; \tag{2.6}$$

δ_{ik} is the Kronecker delta. The filtered momentum equation is therefore

$$\frac{\partial \overline{\rho u_i}}{\partial t} + \frac{\partial \overline{\rho u_i u_k}}{\partial x_k} = -\frac{\partial \bar{p}}{\partial x_i} + \frac{\partial \bar{\sigma}_{ik}}{\partial x_k}. \tag{2.7}$$

Using $\widetilde{u_i u_k} = \overline{\rho u_i u_k}/\bar{\rho}$, Eq. 2.7 becomes

$$\frac{\partial \bar{\rho}\tilde{u}_i}{\partial t} + \frac{\partial \bar{\rho}\tilde{u}_i\tilde{u}_k}{\partial x_k} = -\frac{\partial \bar{p}}{\partial x_i} + \frac{\partial \bar{\sigma}_{ik}}{\partial x_k} + \frac{\partial \tau_{ik}}{\partial x_k}. \tag{2.8}$$

This equation is identical in form to Eq. 2.5, except for the presence of the additional term containing

$$\tau_{ik} \equiv -\bar{\rho}\left(\widetilde{u_i u_k} - \tilde{u}_i\tilde{u}_k\right), \tag{2.9}$$

which is the subgrid stress tensor. This term represents the effects of the unresolved turbulence scales, and must be modeled. Moin et al. [22] represent $\bar{\sigma}_{ik}$ as in Eq. 2.6, but using Favre-filtered variables.

2.1.3 Internal Energy Equation

The internal energy equation can be expressed as

$$\rho\frac{De}{Dt} = -p\frac{\partial u_k}{\partial x_k} + \frac{\partial}{\partial x_k}\left(\kappa\frac{\partial T}{\partial x_k}\right) + \sigma_{ik}\frac{\partial u_k}{\partial x_i} + q_H \tag{2.10}$$

where e is the internal energy, T is the temperature field, κ is the thermal conductivity, and q_H represents external heat sources [23]. Assuming that $q_H = 0$ and using Eq. 2.2, Eq. 2.10 can be written as

$$\frac{\partial(\rho e)}{\partial t} + \frac{\partial(\rho e u_k)}{\partial x_k} = -p\frac{\partial u_k}{\partial x_k} + \frac{\partial}{\partial x_k}\left(\kappa\frac{\partial T}{\partial x_k}\right) + \sigma_{ik}\frac{\partial u_k}{\partial x_i}. \tag{2.11}$$

Using $e = c_v T$, where c_v is the specific heat at constant volume, Eq. 2.11 becomes

$$\frac{\partial\left(\rho c_v T\right)}{\partial t} + \frac{\partial\left(\rho c_v T u_k\right)}{\partial x_k} = -p\frac{\partial u_k}{\partial x_k} + \frac{\partial}{\partial x_k}\left(\kappa\frac{\partial T}{\partial x_k}\right) + \sigma_{ik}\frac{\partial u_k}{\partial x_i}. \tag{2.12}$$

Applying the spatial filter to Eq. 2.12; employing $\tilde{T} = \overline{\rho T}/\bar{\rho}$ and $\widetilde{u_k T} = \overline{\rho u_k T}/\bar{\rho}$; and assuming constant c_v (i.e., calorically perfect gas), the filtered energy equation is

$$c_v\frac{\partial\left(\bar{\rho}\tilde{T}\right)}{\partial t} + c_v\frac{\partial\left(\bar{\rho}\widetilde{u_k T}\right)}{\partial x_k} = -\overline{p\frac{\partial u_k}{\partial x_k}} + \overline{\sigma_{ik}\frac{\partial u_k}{\partial x_i}} + \frac{\partial}{\partial x_k}\left(\overline{\kappa\frac{\partial T}{\partial x_k}}\right). \tag{2.13}$$

Using the perfect gas law $p = \rho R T$, with fixed gas constant R, and

$$\widetilde{T\frac{\partial u_k}{\partial x_k}} = \overline{\rho T\frac{\partial u_k}{\partial x_k}}/\bar{\rho},$$

the pressure dilatation term in Eq. 2.13 can be rewritten

$$\overline{p\frac{\partial u_k}{\partial x_k}} = \bar{\rho}R\widetilde{T\frac{\partial u_k}{\partial x_k}} = \bar{\rho}R\tilde{T}\frac{\partial \tilde{u}_k}{\partial x_k} + \bar{\rho}R\left(\widetilde{T\frac{\partial u_k}{\partial x_k}} - \tilde{T}\frac{\partial \tilde{u}_k}{\partial x_k}\right).$$

Moin et al. [22] argue that the term in parentheses, representing the subgrid-scale contribution to dilatation, is negligible, since "the fluctuation Mach number for the small scales is small," and the term is neglected. Similarly, the viscous dissipation and heat diffusion terms

$$\overline{\sigma_{ik}\frac{\partial u_k}{\partial x_i}} = \tilde{\sigma}_{ik}\frac{\partial \tilde{u}_k}{\partial x_i} + \left(\overline{\sigma_{ik}\frac{\partial u_k}{\partial x_i}} - \tilde{\sigma}_{ik}\frac{\partial \tilde{u}_k}{\partial x_i}\right)$$

and

$$\overline{\kappa\frac{\partial T}{\partial x_k}} = \tilde{\kappa}\frac{\partial \tilde{T}}{\partial x_k} + \left(\overline{\kappa\frac{\partial T}{\partial x_k}} - \tilde{\kappa}\frac{\partial \tilde{T}}{\partial x_k}\right)$$

retain only the resolved components and neglect the subgrid-scale components (in parentheses), resulting in

$$c_v\frac{\partial\left(\bar{\rho}\tilde{T}\right)}{\partial t} + c_v\frac{\partial\left(\bar{\rho}\tilde{u}_k\tilde{T}\right)}{\partial x_k} = -\bar{p}\frac{\partial \tilde{u}_k}{\partial x_k} + \tilde{\sigma}_{ik}\frac{\partial \tilde{u}_k}{\partial x_i} + \frac{\partial}{\partial x_k}\left(\tilde{\kappa}\frac{\partial \tilde{T}}{\partial x_k}\right) - c_v\frac{\partial q_k}{\partial x_k}. \tag{2.14}$$

Here, $q_k \equiv \bar{\rho}\left(\widetilde{u_k T} - \tilde{u}_k\tilde{T}\right)$ is the subgrid heat flux, which must be modeled.

In practice, often no explicit filtering operation is performed in establishing the mathematical model for the LES. Rather, the decomposition of $\mathbf{u}$ into $\bar{\mathbf{u}}$ and $\mathbf{u}'$ is the result of the mesh spacing used—see, for example, references [21] and [1].

2.2 Subgrid-Scale Turbulence Models

In this section, the LES subgrid-scale (sgs) models of Smagorinski, Lundgren and Pullin are presented. In the present reseach, the LES were performed adopting the sgs stretched vortex model developed by Pullin and his collaborators.

2.2.1 The Smagorinsky Model

The first subgrid-scale model, upon which the most popular current models are based, was that proposed by Smagorinsky in his seminal LES research [11]. Borrowing the mixing length concepts developed by Prandtl for the mean flow equations, and applying them to the filtered LES equations, he related the anisotropic part of the subgrid stress tensor, τ_{ij}^r, to the resolved rate of strain tensor, $\tilde{S}_{ij}$, via an sgs eddy viscosity coefficient, ν_{sgs}:

$$\tau_{ij}^r = -2\nu_{sgs}\tilde{S}_{ij} \tag{2.15}$$

where

$$\tilde{S}_{ij} \equiv \frac{1}{2}\left(\frac{\partial \tilde{u}_i}{\partial x_j} + \frac{\partial \tilde{u}_j}{\partial x_i}\right). \tag{2.16}$$

The model calculates the eddy viscosity using a Smagorinsky length scale, l_S, which is analogous to the mixing length:

$$\nu_{sgs} = {l_S}^2\bar{\mathcal{S}}, \tag{2.17}$$

where the characteristic resolved strain rate tensor $\bar{\mathcal{S}} \equiv \left(\tilde{S}_{ij}\tilde{S}_{ij}\right)^{1/2}$; the Smagorinsky length scale is taken to be $C_S\Delta$, with Δ the filter width (or grid spacing). C_S is a Smagorinsky constant, typically in the range of 0.1 to 0.2, but varying with the particular flow geometry (for example, homogeneous turbulence versus wall-bounded turbulence, where C_S should be adjusted lower); this is a result of the model being too dissipative for non-homogeneous turbulence, removing too much turbulence kinetic energy from the resolved flow and transferring it to the subgrid scales [3, 19]. The

need to adjust values of C_S to the type of flow being simulated is a shortcoming of the model.

The Smagorinsky model has other weaknesses. Using a fixed Smagorinsky constant $C_S \neq 0$ causes the model to incorrectly predict non-zero sgs stresses in regions of locally laminar flow; $C_S = 0$ would be correct in these regions. And near walls, LES employing a fixed Smagorinsky constant cannot correctly predict both the transfer of energy from resolved to subgrid scales, and the subgrid shear stress simultaneously. Finally, the Smagorinsky model with $C_S > 0$ allows no backscatter—the transfer of turbulence kinetic energy from subgrid to resolved scales [3]. Filtering DNS turbulent fields shows that some backscatter is correct [19]. The dynamic model and its variations have been developed to calculate locally an appropriate Smagorinsky constant, at the cost of additional complexity, in order to overcome these shortcomings of the original model [18, 19]. However, recognition of these drawbacks leads to selection of a different subgrid-scale model, based on Lundgren's strained spiral vortex concept, for the present research.

2.2.2 Lundgren's strained spiral vortex model of fine turbulence

Observing the formation of "rod-like" or elongated, vortical structures in measurements and LES of small-scale turbulence, T. S. Lundgren [2] proposed a fine turbulence model consisting of an ensemble of vortex tubes, each strained axially by the velocity field of the other tubes, providing local solutions to the Navier-Stokes equation. Since experiments show the spatial distribution of fine turbulence to be intermittent, Lundgren proposed a spiral (rather than axisymmetric) distribution of vorticity in the vortex tubes.

Lundgren's model provides a solution to the incompressible vorticity equation, which is derived by taking the curl of the Navier-Stokes equation:

$$\frac{\partial \vec{\omega}}{\partial t} + \mathbf{u} \cdot \nabla \vec{\omega} = \vec{\omega} \cdot \nabla \mathbf{u} + \nu \nabla^2 \vec{\omega} \tag{2.18}$$

where $\vec{\omega}$ is the vorticity vector. In cylindrical coordinates, a flow described by

$$u_r = -ar/2, \quad u_\theta = 0, \quad u_z = az \tag{2.19}$$

with a being a constant strain rate, would produce axial straining of a vortex tube aligned with the z-axis, concentrating vorticity along the vortex axis. If the vortex tube is specified to possess only a z-component of vorticity, which is independent of z; and to induce an additional velocity, v_r, v_θ, small compared to the background flow (Eq. 2.19), then Eq. 2.18 becomes

$$\frac{\partial \omega}{\partial t} + \left(-\frac{ar}{2} + v_r\right)\frac{\partial \omega}{\partial r} + \frac{v_\theta}{r}\frac{\partial \omega}{\partial \theta} = \omega a + \nu \nabla^2 \omega \tag{2.20}$$

which, with the continuity equation for the induced velocity,

$$\frac{\partial r v_r}{\partial r} + \frac{\partial v_\theta}{\partial \theta} = 0, \tag{2.21}$$

can be solved (via introduction of a stream function):

$$\omega\,(r, \theta, t) = S(t)\,\omega_2\left(S(t)^{1/2} r, \theta, \int_0^t S(t')dt'\right) \tag{2.22}$$

where

$$S(t) = \exp\left(\int_0^t a\,dt'\right) \tag{2.23}$$

is the ratio of the length of a vortex at time t to its initial length, and ω_2 is a known 2-D solution of Eq. 2.20 and Eq. 2.21 with initial conditions matching those of the straining vortex tube.

Defining ω_2 such that the vorticity in a tube is distributed in a spiral structure, Lundgren [2] showed that the spiral region of vorticity is pulled radially inward as the flow axially stretches the tube, with the vorticity intensifying while the wavenumber associated with the tube increases—simulating the energy cascade from large (low-wavenumber) scales to small (high-wavenumber) scales. Eventually, the radius of the strained tube becomes small enough for viscosity to cause decay of the vorticity distribution.

Additionally, Lundgren [2] showed that the resulting energy spectrum for this fine turbulence model is

$$E(\kappa) = A\kappa^{-5/3} \exp\left(-2\nu\kappa^2/3a\right). \tag{2.24}$$

Although this spectrum does not contain the $\varepsilon^{2/3}$ behavior, it does include the $\kappa^{-5/3}$ factor. Finally, Lundgren pointed to experimental results, where hot-wire anemometer measurements of turbulence produce intermittent signals matching those that would be produced by spiral layers of vorticity. Thus, there are compelling reasons to adapt this fine turbulence model for use in large-eddy simulation.

2.2.3 A stretched vortex-based LES subgrid-scale model

Pullin and Saffman [24] began a computational research effort to employ Lundgren's model as a subgrid-scale model for large-eddy simulation, focusing first on a probability-based transformation of vorticity from local vortex-based to fixed laboratory-based axis systems, with a probability density function P, describing the anisotropy of the turbulence, being determined by effects of the resolved-scale velocity field on the particular subgrid vortex tube. From this local probability density (and the associated axis transformation) and an assumed subgrid energy spectrum, they determined a model subgrid stress tensor τ_{ij}.

Misra and Pullin [19] modeled the distribution of local vortex structures (i.e., the probability density function) as a product of delta functions, giving

$$\tau_{ij} = \left(\delta_{ij} - e_i^v e_j^v\right) \int_{k_c}^{\infty} E(k)dk = \left(\delta_{ij} - e_i^v e_j^v\right) K, \tag{2.25}$$

where $k_c = \pi/\Delta$ is the cutoff wavenumber, above which the small-scale turbulence is modeled (Δ being the grid spacing); $\mathbf{e}^v$ is the unit vector describing the orientation of the local subgrid vortex (alignment of $\mathbf{e}^v$ with the most extensional eigenvector of the resolved strain rate tensor was shown to work well in [25] although, unlike other alignment models proposed there, it does not contain backscatter); and $K = \tau_{ii}/2$ is the local subgrid kinetic energy. Kosović, Pullin and Samtaney [26] recast

Lundgren's energy spectrum (Eq. 2.24) as $E(k) = \mathcal{K}_0 \varepsilon^{2/3} k^{-5/3} \exp\left[-2\nu k^2 / \left(3\left|\tilde{a}\right|\right)\right]$, where $\tilde{a} = e_i^v e_j^v \tilde{S}_{ij}$ is the subgrid vortex axial stretching due to the local resolved flow, and used the six-point structure function estimation procedure of Voelkl, Pullin and Chan [25] to calculate $\mathcal{K}_0 \varepsilon^{2/3}$. Using Pullin's model for the subgrid flux of a passive scalar [20], they then presented a corresponding model for the subgrid heat flux (per unit mass),

$$q_i = \widetilde{Tu_i} - \tilde{T}\tilde{u}_i = \frac{1}{2}\Delta K^{1/2}\left(\delta_{ij} - e_i^v e_j^v\right)\frac{\partial \tilde{T}}{\partial x_j}. \tag{2.26}$$

In the present work, Pullin's model for the subgrid stress tensor (Eq. 2.25) and subgrid heat flux (2.26) is adopted.

2.3 LES Wall Modeling

Throughout this thesis, the following terminology will be used: x, u represent the streamwise direction and velocity, respectively; y, v represent the wall-normal (vertical) direction and velocity; and z, w represent the spanwise direction and velocity—see Figure 2.1. The wall models of Pantano et al., 2008 [21] and of Chung and Pullin, 2009 [1] for incompressible channel flows are presentented in sections 2.3.1 and 2.3.2, respectively. In section 2.3.3, the present wall model for compressible channel flow is presented.

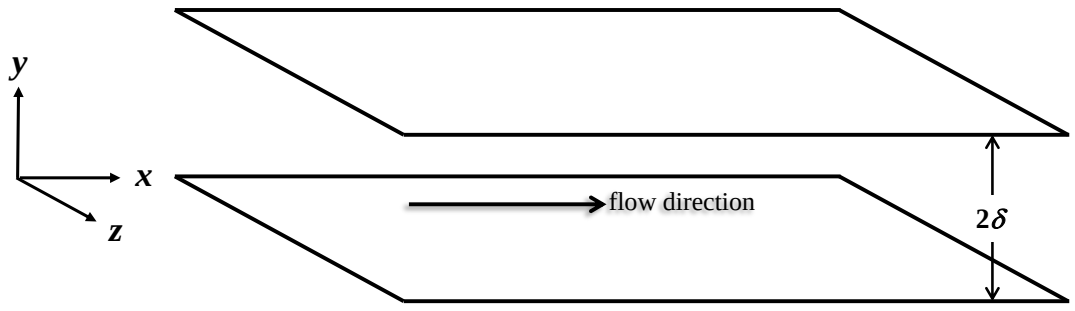

Figure 2.1: Selected orientation of the coordinate axis system

2.3.1 Wall Model of Pantano et al. (2008)

The concept of using the law of the wall to determine a shear stress boundary condition remains a popular approach to wall treatment within LES. For example, Pantano et al. [21] perform LES of a low-Mach number turbulent channel, using the law of the wall to relate the streamwise and spanwise velocities to the wall shear stress. That is, they assume that the first grid point off the wall lies within the log-law region of the flow, and that the law of the wall holds locally and instantaneously for the resolved velocity field. In each wall-adjacent grid cell, they use the local resolved streamwise velocity $\tilde{u}$ and an iterative (Newton-Raphson) method to determine the local friction velocity u_τ such that

$$\frac{\tilde{u}}{u_\tau} = \frac{1}{\kappa} \ln\left(\frac{y u_\tau}{\nu}\right) + B,$$

selecting $\kappa = 0.4$ and $B = 5$. Then the wall shear stress, $\tau_w = \rho u_\tau^2$, is used as the wall boundary condition. Using a computational mesh of 5.7 million grid points, Pantano et al. compare their $Re_\tau = 2003$ results with the incompressible DNS of Hoyas and Jiménez, which used nearly 18 billion grid points [9]; their predicted velocity profiles, turbulence intensities, and Reynolds stress statistics match the DNS results well. However, this wall treatment relies on empirically derived values for κ and B, and adjusting these parameters can be expected to change the turbulence properties of the simulation. Key results in Pantano et al., 2008 [21] will be presented in section 3.1.

2.3.2 Wall Model of Chung and Pullin (2009)

Chung and Pullin [1] adopt the stretched-vortex sgs model described in section 2.2.3 to develop a near-wall model for use in large-eddy simulation of high-Reynolds number turbulent channel flows. They seek a parameter-free method to determine the local wall shear stress without having to resolve the sharp velocity gradient at the wall. The filtered, streamwise momentum equation for LES of incompressible flows can be

written from Eq. 2.8 as

$$\frac{\partial \tilde{u}}{\partial t} + \frac{\partial \widetilde{uu}}{\partial x} + \frac{\partial \widetilde{uv}}{\partial y} + \frac{\partial \widetilde{uw}}{\partial z} = -\frac{\partial \tilde{p}}{\partial x} + \nu \frac{\partial^2 \tilde{u}}{\partial y^2}. \tag{2.27}$$

The lateral diffusion terms are asserted to be small, due to the relatively large size of the filter width (grid spacing), and are neglected. $\tilde{p}$ is the kinematic resolved pressure (i.e., pressure per unit density), and $-\partial\tilde{p}/\partial x$ includes the mean pressure gradient $f(t)$ driving the flow in the channel.

Defining a wall-adjacent averaging filter of arbitrary thickness h,

$$\langle \phi \rangle (x,z,t) \equiv \frac{1}{h} \int_0^h \tilde{\phi}\,(x,y,z,t)\,dy \tag{2.28}$$

(with the wall at $y = 0$) and applying it to Eq. 2.27 gives

$$\frac{\partial \langle u \rangle}{\partial t} + \frac{\partial \langle uu \rangle}{\partial x} + \frac{\partial \langle uw \rangle}{\partial z} + \frac{1}{h}\left(\widetilde{uv}|_h - \widetilde{uv}|_0\right) = -\frac{1}{h}\left(\frac{\partial \tilde{p}}{\partial x} y\right)_0^h + \frac{\nu}{h}\left(\left.\frac{\partial \tilde{u}}{\partial y}\right|_h - \left.\frac{\partial \tilde{u}}{\partial y}\right|_0\right) \tag{2.29}$$

with the local streamwise pressure gradient assumed constant through the wall-adjacent layer; applying the no-slip and no-penetration conditions $\tilde{u}(x,0,z,t) = \tilde{v}(x,0,z,t) = \tilde{w}(x,0,z,t) = 0$ gives

$$\frac{\partial \langle u \rangle}{\partial t} + \frac{\partial \langle uu \rangle}{\partial x} + \frac{\partial \langle uw \rangle}{\partial z} = -\frac{1}{h}\,\widetilde{uv}|_h - \left.\frac{\partial \tilde{p}}{\partial x}\right|_h + \frac{\nu}{h}\left(\left.\frac{\partial \tilde{u}}{\partial y}\right|_h - \eta_0\right) \tag{2.30}$$

with

$$\eta_0 \equiv \left.\frac{\partial \tilde{u}}{\partial y}\right|_0 \tag{2.31}$$

the wall-normal gradient of the resolved streamwise velocity. Note that $\nu\eta_0 = \tau_w/\rho = {u_\tau}^2$.

Next, Chung and Pullin [1] make the assumption that the turbulence in each wall-adjacent computational cell can be characterized by the friction velocity u_τ and the viscous lengthscale δ_ν. Since $\delta_\nu = \nu/u_\tau$ and $\nu\eta_0 = {u_\tau}^2$, this is equivalent to assuming that the local turbulence can be characterized by ν and the local η_0, such that

$$\tilde{u}(x,y,z,t) = (\nu\eta_0(x,z,t))^{1/2}\, F(y^+) \tag{2.32}$$

where $y^+ \equiv y/\delta_\nu$ and F is a non-dimensional velocity profile shape function (or local "law of the wall") whose shape need not be specified, as will be seen. Differentiating Eq. 2.32 gives

$$\frac{\partial \tilde{u}}{\partial \eta_0} = \frac{1}{2} F \nu^{1/2} {\eta_0}^{-1/2} + \nu^{1/2} {\eta_0}^{1/2} \frac{\partial F}{\partial \eta_0} \tag{2.33}$$

or, using the chain rule $\partial F/\partial \eta_0 = (\partial F/\partial y^+)(\partial y^+/\partial \eta_0)$,

$$\frac{\partial \tilde{u}}{\partial \eta_0} = \frac{1}{2} \left(\frac{\nu}{\eta_0}\right)^{1/2} F + \frac{1}{2} F' y = \frac{1}{2} \left(\frac{\nu}{\eta_0}\right)^{1/2} \left(F + F' y^+\right) \tag{2.34}$$

where $F' \equiv \partial F/\partial y^+$.

Applying the near-wall averaging (Eq. 2.28) to Eq. 2.34 gives

$$\begin{aligned} \frac{\partial \langle u \rangle}{\partial \eta_0} &= \frac{1}{2h} \left(\frac{\nu}{\eta_0}\right)^{1/2} \left[\int_0^h F(y^+) dy + \int_0^h y^+ F'(y^+) dy\right] \\ &= \frac{1}{2h^+} \left[\int_0^h F(y^+) dy + \int_0^h y^+ F'(y^+) dy\right] \\ &= \frac{1}{2h^+} \left[\int_0^{h^+} F(y^+) \left(\frac{\nu}{\eta_0}\right)^{1/2} dy^+ + \int_0^{h^+} y^+ F'(y^+) \left(\frac{\nu}{\eta_0}\right)^{1/2} dy^+\right] \end{aligned} \tag{2.35}$$

using the change of variable $dy^+ = (\eta_0/\nu)^{1/2} dy$. Integration by parts gives

$$\frac{\partial \langle u \rangle}{\partial \eta_0} = \frac{1}{2} \left(\frac{\nu}{\eta_0}\right)^{1/2} F(h^+) = \frac{1}{2\eta_0} \, \tilde{u}|_h \tag{2.36}$$

using Eq. 2.32. Since (using the chain rule)

$$\frac{\partial \langle u \rangle}{\partial t} = \frac{\partial \langle u \rangle}{\partial \eta_0} \frac{\partial \eta_0}{\partial t} = \frac{\tilde{u}|_h}{2\eta_0} \frac{\partial \eta_0}{\partial t}, \tag{2.37}$$

Eq. 2.30 becomes

$$\frac{\tilde{u}|_h}{2\eta_0} \frac{\partial \eta_0}{\partial t} + \frac{\partial \langle uu \rangle}{\partial x} + \frac{\partial \langle uw \rangle}{\partial z} = -\frac{1}{h} \, \widetilde{uv}|_h - \left.\frac{\partial \tilde{p}}{\partial x}\right|_h + \frac{\nu}{h} \left(\left.\frac{\partial \tilde{u}}{\partial y}\right|_h - \eta_0\right). \tag{2.38}$$

Finally, Chung and Pullin [1] approximate

$$\frac{\partial \langle uu \rangle}{\partial x} \approx \frac{\partial \widetilde{uu}|_h}{\partial x}, \quad \frac{\partial \langle uw \rangle}{\partial z} \approx \frac{\partial \widetilde{uw}|_h}{\partial z}, \tag{2.39}$$

resulting in

$$\frac{\partial \eta_0}{\partial t} = \frac{2\eta_0}{\tilde{u}|_h}\left[-\frac{1}{h}\,\widetilde{uv}|_h - \frac{\partial \widetilde{uu}|_h}{\partial x} - \frac{\partial \widetilde{uw}|_h}{\partial z} - \left.\frac{\partial \tilde{p}}{\partial x}\right|_h + \frac{\nu}{h}\left(\left.\frac{\partial \tilde{u}}{\partial y}\right|_h - \eta_0\right)\right] \tag{2.40}$$

which is an ordinary differential equation describing the time evolution of the local wall velocity gradient (or, equivalently, shear stress). In the LES, the terms on the r.h.s. of Eq. 2.40 can be calculated purely from the values computed at $z = h$. The stretched-vortex sgs model provides $\widetilde{uu}$, $\widetilde{uv}$ and $\widetilde{uw}$; h is chosen to be the distance from the wall to the first grid point in the computational mesh of the LES. Thus, at every time step and at every wall-adjacent grid point, Eq. 2.40 is integrated (using a third-order Runge-Kutta method) to find η_0, which is used as a boundary condition.

Further, Chung and Pullin [1] develop a streamwise slip velocity boundary condition, which they apply at a "lifted virtual wall" a small distance above the physical wall, and at which location spanwise no-slip and vertical no-penetration velocity BCs are also enforced. The lifted virtual wall is placed at a height of either 18% or 36% of the wall-normal grid spacing; for their lowest-Re_τ simulations, these correspond to $y^+ \approx 15$ and $y^+ \approx 30$, respectively. They evaluate their wall model in 13 large-eddy simulations, on 442,368-cell and 3.5 million-cell grids, at Reynolds numbers (based on mean centerline velocity and channel half-height) ranging from 49×10^3 to 990×10^6, and friction Reynolds numbers Re_τ from 2×10^3 to 20×10^6. At $Re_\tau = 2003$, their mean streamwise velocity profile, turbulence intensities and Reynolds stress predictions generally match the DNS of Hoyas and Jiménez well, with the predictions of spanwise and vertical fluctuations being least successful, likely due to the selection of the corresponding velocity boundary conditions at the lifted virtual wall. These results will be summarized in section 3.2.

It is again emphasized that this wall model, Eq. 2.40, is parameter-free, and the specifics of channel flow geometry do not factor into its development. Therefore, the model can be expected to apply to any smooth-wall turbulent flow, and need not be "dialed in" for a specific class of flow geometries via experimentally derived but

somewhat arbitrary constants. For these reasons, this model serves as the inspiration for the present compressible-flow wall model, given in the following section. It is noted, though, that the resulting ordinary differential equation will be applied directly through the τ_w boundary condition, as in Pantano et al., 2008 [21], rather than via the streamwise slip velocity used by Chung and Pullin [1].

2.3.3 Present Wall Model for LES of Compressible Channel Flows

Relatively few large-eddy simulations of compressible channel flows have been reported in the literature [27, 28, 29, 30], and all use grid point clustering near the wall to achieve near-wall resolution (LES-NWR). None to date have developed a wall model in the sense of LES-NWM, and so the severe mesh resolution restrictions described in section 1.4 would apply when simulating high-Reynolds number flows. Therefore, a new wall model for large-eddy simulation of compressible flows is now developed from the LES compressible momentum and energy equations.

Momentum Equation

The filtered, streamwise momentum equation for LES of compressible flows can be written from Eq. 2.8 as

$$\frac{\partial\left(\bar{\rho}\tilde{u}\right)}{\partial t}+\frac{\partial\left(\bar{\rho}\widetilde{uu}\right)}{\partial x}+\frac{\partial\left(\bar{\rho}\widetilde{uv}\right)}{\partial y}+\frac{\partial\left(\bar{\rho}\widetilde{uw}\right)}{\partial z}=-\frac{\partial\bar{p}}{\partial x}+\frac{\partial\bar{\sigma}_{ii}}{\partial x}+\frac{\partial\bar{\sigma}_{ij}}{\partial y}+\frac{\partial\bar{\sigma}_{ik}}{\partial z}. \tag{2.41}$$

Expanding all terms gives

$$\begin{aligned}\frac{\partial\left(\bar{\rho}\tilde{u}\right)}{\partial t}+\frac{\partial\left(\bar{\rho}\widetilde{uu}\right)}{\partial x}+\frac{\partial\left(\bar{\rho}\widetilde{uv}\right)}{\partial y}+\frac{\partial\left(\bar{\rho}\widetilde{uw}\right)}{\partial z}=&\\ -\frac{\partial\bar{p}}{\partial x}+\frac{4}{3}\left(\tilde{\mu}\frac{\partial^2\tilde{u}}{\partial x^2}+\frac{\partial\tilde{u}}{\partial x}\frac{\partial\tilde{\mu}}{\partial x}\right)+\tilde{\mu}\left(\frac{\partial^2\tilde{u}}{\partial y^2}+\frac{\partial^2\tilde{v}}{\partial x\partial y}\right)+&\\ \left(\frac{\partial\tilde{u}}{\partial y}+\frac{\partial\tilde{v}}{\partial x}\right)\frac{\partial\tilde{\mu}}{\partial y}+\tilde{\mu}\left(\frac{\partial^2\tilde{u}}{\partial z^2}+\frac{\partial^2\tilde{w}}{\partial x\partial z}\right)+\left(\frac{\partial\tilde{u}}{\partial z}+\frac{\partial\tilde{w}}{\partial x}\right)\frac{\partial\tilde{\mu}}{\partial z}.&\end{aligned} \tag{2.42}$$

As in Chung and Pullin, 2009 [1], the lateral diffusion, "which is justifiably small, given the relative size of the filter width," will be neglected. Additionally, using this

reasoning, streamwise and spanwise gradients of velocity and viscosity are relatively small, so products of these in-plane gradients are negligible. Therefore, the terms

$$\frac{4}{3}\tilde{\mu}\frac{\partial^2\tilde{u}}{\partial x^2}, \quad \frac{4}{3}\frac{\partial\tilde{u}}{\partial x}\frac{\partial\tilde{\mu}}{\partial x}, \quad \tilde{\mu}\frac{\partial^2\tilde{u}}{\partial z^2}, \quad \tilde{\mu}\frac{\partial^2\tilde{w}}{\partial x\partial z}, \quad \frac{\partial\tilde{u}}{\partial z}\frac{\partial\tilde{\mu}}{\partial z}, \quad \frac{\partial\tilde{w}}{\partial x}\frac{\partial\tilde{\mu}}{\partial z}$$

will be neglected, and Eq. 2.42 is thus simplified to

$$\frac{\partial\bar{\rho}\tilde{u}}{\partial t} + \frac{\partial\bar{\rho}\widetilde{uu}}{\partial x} + \frac{\partial\bar{\rho}\widetilde{uv}}{\partial y} + \frac{\partial\bar{\rho}\widetilde{uw}}{\partial z} = - \frac{\partial\bar{p}}{\partial x} + \tilde{\mu}\left(\frac{\partial^2\tilde{u}}{\partial y^2} + \frac{\partial^2\tilde{v}}{\partial x\partial y}\right) + \left(\frac{\partial\tilde{u}}{\partial y} + \frac{\partial\tilde{v}}{\partial x}\right)\frac{\partial\tilde{\mu}}{\partial y}. \quad (2.43)$$

Defining the averaging filter[1] in the wall-adjacent layer of thickness h,

$$\{f\}(x,z,t) \equiv \frac{1}{h}\int_0^h f(x,y,z,t)\,dy, \quad (2.44)$$

and applying it to Eq. 2.43 gives

$$\frac{\partial\{\bar{\rho}\tilde{u}\}}{\partial t} + \frac{\partial\{\bar{\rho}\widetilde{uu}\}}{\partial x} + \frac{\partial\{\bar{\rho}\widetilde{uw}\}}{\partial z} = - \frac{1}{h}\int_0^h \frac{\partial\bar{\rho}\widetilde{uv}}{\partial y}dy - \frac{1}{h}\int_0^h \frac{\partial\bar{p}}{\partial x}dy + \frac{1}{h}\int_0^h \tilde{\mu}\frac{\partial^2\tilde{u}}{\partial y^2}dy + \frac{1}{h}\int_0^h \tilde{\mu}\frac{\partial^2\tilde{v}}{\partial x\partial y}dy + \frac{1}{h}\int_0^h \frac{\partial\tilde{u}}{\partial y}\frac{\partial\tilde{\mu}}{\partial y}dy + \frac{1}{h}\int_0^h \frac{\partial\tilde{v}}{\partial x}\frac{\partial\tilde{\mu}}{\partial y}dy. \quad (2.45)$$

As in Chung and Pullin, 2009 [1], it will be assumed that the streamwise pressure gradient is approximately constant through this near-wall layer, and therefore equal to $(\partial\bar{p}/\partial x)\,|_h$. Dynamic viscosity is a function of temperature only, and the temperature variation in the wall-adjacent layer $0 \le y \le h$ will not be resolved. For channels with isothermal walls, $\tilde{\mu}$ is known at $y = 0$ and at $y = h$. The mean temperature varies

[1] Chung and Pullin [1] specifically define their averaging operator, denoted with $\langle\cdot\rangle$, as being applied to a single filtered quantity, and then drop the tilde notation in the resulting averaged equation. Here, the averaging operator, denoted with $\{\cdot\}$, may be applied to products of filtered and Favre-filtered quantities; for clarity, the tilde/overbar notation is retained in the resulting averaged equation. Additionally, use of $\{\cdot\}$ avoids confusion with the ensemble average $\langle\cdot\rangle$ used to report turbulent statistics.

approximately linearly in the near wall region for $y/\delta \lesssim 0.04$, as shown in Fig. 4 of Huang, Coleman and Bradshaw, 1995 [31]—reproduced here as Fig. 2.2—and Fig. 7 of Coleman, Kim and Moser, 1995 [32]. Assuming a linear temperature profile and using $\mu/\mu_w = (T/T_w)^{0.76}$, the average viscosity in the near-wall layer is

$$\hat{\mu} \equiv \frac{1}{T|_h - T|_0} \int_{T|_0}^{T|_h} \tilde{\mu}(T) dT$$
$$= \frac{\tilde{\mu}|_0}{1.76 \tilde{T}\Big|_0^{0.76} \left(\tilde{T}\Big|_h - \tilde{T}\Big|_0 \right)} \left(\tilde{T}\Big|_h^{1.76} - \tilde{T}\Big|_0^{1.76} \right). \quad (2.46)$$

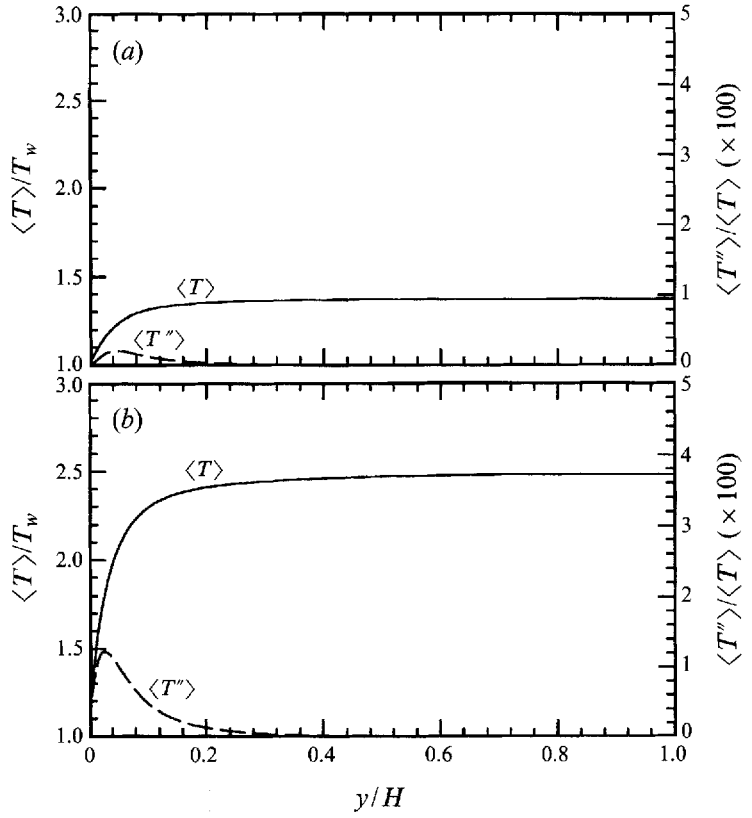

Figure 2.2: Temperature profiles, mean (—) and fluctuating (– –) components: (a) $M = 1.5$, (b) $M = 3$. (Reproduced from Fig. 4 in Huang, Coleman and Bradshaw, 1995 [31].)

Replacing $\tilde{\mu}(y)$ with the local average viscosity $\hat{\mu}$, Eq. 2.45 becomes

$$\frac{\partial\{\bar{\rho}\tilde{u}\}}{\partial t}+\frac{\partial\{\bar{\rho}\widetilde{uu}\}}{\partial x}+\frac{\partial\{\bar{\rho}\widetilde{uw}\}}{\partial z}= \\ -\frac{1}{h}\bar{\rho}\widetilde{uv}|_h-\left.\frac{\partial\bar{p}}{\partial x}\right|_h+\frac{\hat{\mu}}{h}\left[\frac{\partial\tilde{u}}{\partial y}\right]_0^h-\frac{1}{h}\int_0^h\frac{\partial\tilde{\mu}}{\partial y}\frac{\partial\tilde{u}}{\partial y}dy+ \\ \frac{\hat{\mu}}{h}\left[\frac{\partial\tilde{v}}{\partial x}\right]_0^h-\frac{1}{h}\int_0^h\frac{\partial\tilde{\mu}}{\partial y}\frac{\partial\tilde{v}}{\partial x}dy+\frac{1}{h}\int_0^h\frac{\partial\tilde{u}}{\partial y}\frac{\partial\tilde{\mu}}{\partial y}dy+\frac{1}{h}\int_0^h\frac{\partial\tilde{v}}{\partial x}\frac{\partial\tilde{\mu}}{\partial y}dy. \quad (2.47)$$

Applying the no-slip and no-penetration conditions at the wall and using integration by parts, Eq. 2.47 can be written as

$$\frac{\partial\{\bar{\rho}\tilde{u}\}}{\partial t}+\frac{\partial\{\bar{\rho}\widetilde{uu}\}}{\partial x}+\frac{\partial\{\bar{\rho}\widetilde{uw}\}}{\partial z}= \\ -\frac{1}{h}\bar{\rho}\widetilde{uv}|_h-\left.\frac{\partial\bar{p}}{\partial x}\right|_h+\left.\frac{\hat{\mu}}{h}\frac{\partial\tilde{u}}{\partial y}\right|_h-\frac{\hat{\mu}}{h}\eta_0+\left.\frac{\hat{\mu}}{h}\frac{\partial\tilde{v}}{\partial x}\right|_h \quad (2.48)$$

where $\eta_0\equiv\left(\partial\tilde{u}/\partial y\right)|_0$, as defined in Eq. 2.31.

On the basis of dimensional analysis, assume that

$$\bar{\rho}\tilde{u}=\bar{\rho}_w{\nu_w}^{1/2}{\eta_0}^{1/2}F\left(y^+\right), \quad (2.49)$$

where ρ_w and ν_w are values at the wall. Differentiating Eq. 2.49 with respect to η_0 gives

$$\frac{\partial\bar{\rho}\tilde{u}}{\partial\eta_0}=\frac{1}{2}\bar{\rho}_w{\nu_w}^{1/2}{\eta_0}^{-1/2}F+\bar{\rho}_w{\nu_w}^{1/2}{\eta_0}^{1/2}F'\frac{\partial y^+}{\partial\eta_0}, \quad (2.50)$$

with $F'\equiv\partial F/\partial y^+$, or

$$\frac{\partial\bar{\rho}\tilde{u}}{\partial\eta_0}=\frac{1}{2}\bar{\rho}_w\frac{{\nu_w}^{1/2}}{{\eta_0}^{1/2}}F+\bar{\rho}_w{\nu_w}^{1/2}{\eta_0}^{1/2}F'\frac{1}{2}\frac{y}{{\eta_0}^{1/2}{\nu_w}^{1/2}}=\frac{1}{2}\bar{\rho}_w\frac{{\nu_w}^{1/2}}{{\eta_0}^{1/2}}F+\frac{1}{2}\bar{\rho}_wF'y \quad (2.51)$$

$$=\frac{1}{2}\bar{\rho}_w\frac{{\nu_w}^{1/2}}{{\eta_0}^{1/2}}\left[F+F'y\frac{{\eta_0}^{1/2}}{{\nu_w}^{1/2}}\right]=\frac{\bar{\rho}_w}{2}\left(\frac{\nu_w}{\eta_0}\right)^{1/2}\left[F+F'y\right].$$

Applying the average in the wall-adjacent layer (Eq. 2.44) gives

$$\frac{\partial\{\bar{\rho}\tilde{u}\}}{\partial\eta_0}=\frac{\bar{\rho}_w}{2h}\left(\frac{\nu_w}{\eta_0}\right)^{1/2}\left[\int_0^h F\left(y^+\right)dy+\int_0^h y^+F'\left(y^+\right)dy\right]$$

$$=\frac{\bar{\rho}_w}{2h^+}\frac{{\nu_w}^{1/2}}{{\eta_0}^{1/2}}\left[\int_0^{h^+}F\left(y^+\right)dy^++y^+F\left(y^+\right)\Big|_0^{h^+}-\int_0^{h^+}F\left(y^+\right)dy^+\right]$$

$$= \frac{\bar{\rho}_w}{2h^+} \frac{{\nu_w}^{1/2}}{{\eta_0}^{1/2}} h^+ F\left(h^+\right) \frac{{\eta_0}^{1/2}}{{\eta_0}^{1/2}}$$

$$= \frac{\bar{\rho}\tilde{u}|_h}{2\eta_0}. \tag{2.52}$$

Finally,

$$\frac{\partial\left\{\bar{\rho}\tilde{u}\right\}}{\partial t} = \frac{\partial\left\{\bar{\rho}\tilde{u}\right\}}{\partial \eta_0}\frac{\partial \eta_0}{\partial t} = \frac{\bar{\rho}\tilde{u}|_h}{2\eta_0}\frac{\partial \eta_0}{\partial t}, \tag{2.53}$$

and Eq. 2.48 becomes

$$\frac{\bar{\rho}\tilde{u}|_h}{2\eta_0}\frac{\partial \eta_0}{\partial t} + \frac{\partial\left\{\bar{\rho}\widetilde{uu}\right\}}{\partial x} + \frac{\partial\left\{\bar{\rho}\widetilde{uw}\right\}}{\partial z} = - \frac{1}{h}\,\bar{\rho}\widetilde{uv}|_h - \left.\frac{\partial \bar{p}}{\partial x}\right|_h + \left.\frac{\bar{\mu}}{h}\frac{\partial \tilde{u}}{\partial y}\right|_h - \frac{\bar{\mu}}{h}\eta_0 + \left.\frac{\bar{\mu}}{h}\frac{\partial \tilde{v}}{\partial x}\right|_h. \tag{2.54}$$

As in Chung and Pullin, 2009 [1], the lateral gradients of $\bar{\rho}\widetilde{uu}$ and $\bar{\rho}\widetilde{uw}$ will be approximated as

$$\frac{\partial\left\{\bar{\rho}\widetilde{uu}\right\}}{\partial x} \approx \frac{\partial\,\bar{\rho}\widetilde{uu}|_h}{\partial x} \quad \text{and} \quad \frac{\partial\left\{\bar{\rho}\widetilde{uw}\right\}}{\partial z} \approx \frac{\partial\,\bar{\rho}\widetilde{uw}|_h}{\partial z},$$

such that

$$\frac{\partial \eta_0}{\partial t} = \frac{2\eta_0}{\bar{\rho}\tilde{u}|_h}\left[-\frac{1}{h}\,\bar{\rho}\widetilde{uv}|_h - \frac{\partial\,\bar{\rho}\widetilde{uu}|_h}{\partial x} - \frac{\partial\,\bar{\rho}\widetilde{uw}|_h}{\partial z} - \left.\frac{\partial \bar{p}}{\partial x}\right|_h + \frac{\hat{\mu}}{h}\left(\left.\frac{\partial \tilde{u}}{\partial y}\right|_h + \left.\frac{\partial \tilde{v}}{\partial x}\right|_h - \eta_0\right)\right]. \tag{2.55}$$

The stretched-vortex subgrid-scale model provides $\widetilde{uu}$, $\widetilde{uv}$ and $\widetilde{uw}$. As in the incompressible wall model of Chung and Pullin [1], this differential equation describes the time evolution of the local wall velocity gradient, from which $\tau_w = \mu_w \eta_0$ can be calculated and applied as a momentum boundary condition. Note that, when Eq. 2.55 is implemented at the top wall, the sign is reversed on the terms $\widetilde{uv}|_h$, $\partial\tilde{u}/\partial y|_h$ and $\partial\tilde{v}/\partial x|_h$; this accounts for the change in direction of wall-normal gradients, etc. at the top wall versus the bottom wall.

Energy Equation

Equation 2.14 in section 2.1 is

$$c_v \frac{\partial\left(\bar{\rho}\tilde{T}\right)}{\partial t} + c_v \frac{\partial\left(\bar{\rho}\tilde{u}_k\tilde{T}\right)}{\partial x_k} = -\bar{p}\frac{\partial \tilde{u}_k}{\partial x_k} + \tilde{\sigma}_{ik}\frac{\partial \tilde{u}_k}{\partial x_i} + \frac{\partial}{\partial x_k}\left(\tilde{\kappa}\frac{\partial \tilde{T}}{\partial x_k}\right) - c_v\frac{\partial q_k}{\partial x_k}$$

or, equivalently,

$$c_v \frac{\partial\left(\bar{\rho}\tilde{T}\right)}{\partial t} + c_v \frac{\partial\left(\widetilde{\bar{\rho}u_k T}\right)}{\partial x_k} = -\bar{p}\frac{\partial \tilde{u}_k}{\partial x_k} + \tilde{\sigma}_{ik}\frac{\partial \tilde{u}_k}{\partial x_i} + \frac{\partial}{\partial x_k}\left(\tilde{\kappa}\frac{\partial \tilde{T}}{\partial x_k}\right). \tag{2.56}$$

Expanding all the terms gives

$$\begin{aligned} c_v \frac{\partial\left(\bar{\rho}\tilde{T}\right)}{\partial t} + c_v \left[\frac{\partial\left(\widetilde{\bar{\rho}u T}\right)}{\partial x} + \frac{\partial\left(\widetilde{\bar{\rho}v T}\right)}{\partial y} + \frac{\partial\left(\widetilde{\bar{\rho}w T}\right)}{\partial z}\right] &= -\bar{p}\frac{\partial \tilde{u}}{\partial x} - \bar{p}\frac{\partial \tilde{v}}{\partial y} - \bar{p}\frac{\partial \tilde{w}}{\partial z} \\ &+ \frac{4}{3}\tilde{\mu}\frac{\partial \tilde{u}}{\partial x}\frac{\partial \tilde{u}}{\partial x} + \tilde{\mu}\frac{\partial \tilde{u}}{\partial y}\frac{\partial \tilde{v}}{\partial x} + \tilde{\mu}\frac{\partial \tilde{v}}{\partial x}\frac{\partial \tilde{v}}{\partial x} + \tilde{\mu}\frac{\partial \tilde{u}}{\partial z}\frac{\partial \tilde{w}}{\partial x} + \tilde{\mu}\frac{\partial \tilde{w}}{\partial x}\frac{\partial \tilde{w}}{\partial x} \\ &+ \tilde{\mu}\frac{\partial \tilde{v}}{\partial x}\frac{\partial \tilde{u}}{\partial y} + \tilde{\mu}\frac{\partial \tilde{u}}{\partial y}\frac{\partial \tilde{u}}{\partial y} + \frac{4}{3}\tilde{\mu}\frac{\partial \tilde{v}}{\partial y}\frac{\partial \tilde{v}}{\partial y} + \tilde{\mu}\frac{\partial \tilde{v}}{\partial z}\frac{\partial \tilde{w}}{\partial y} + \tilde{\mu}\frac{\partial \tilde{w}}{\partial y}\frac{\partial \tilde{w}}{\partial y} \\ &+ \tilde{\mu}\frac{\partial \tilde{w}}{\partial x}\frac{\partial \tilde{u}}{\partial z} + \tilde{\mu}\frac{\partial \tilde{u}}{\partial z}\frac{\partial \tilde{u}}{\partial z} + \tilde{\mu}\frac{\partial \tilde{w}}{\partial y}\frac{\partial \tilde{v}}{\partial z} + \tilde{\mu}\frac{\partial \tilde{v}}{\partial z}\frac{\partial \tilde{v}}{\partial z} + \frac{4}{3}\tilde{\mu}\frac{\partial \tilde{w}}{\partial z}\frac{\partial \tilde{w}}{\partial z} \\ &+ \frac{\partial}{\partial x}\left(\tilde{\kappa}\frac{\partial \tilde{T}}{\partial x}\right) + \frac{\partial}{\partial y}\left(\tilde{\kappa}\frac{\partial \tilde{T}}{\partial y}\right) + \frac{\partial}{\partial z}\left(\tilde{\kappa}\frac{\partial \tilde{T}}{\partial z}\right). \end{aligned} \tag{2.57}$$

In an analogy to Chung and Pullin, 2009 [1], the lateral heat diffusion,

$$\frac{\partial}{\partial x}\left(\tilde{\kappa}\frac{\partial \tilde{T}}{\partial x}\right) \text{ and } \frac{\partial}{\partial z}\left(\tilde{\kappa}\frac{\partial \tilde{T}}{\partial z}\right),$$

will be neglected. Additionally, using the reasoning in the subsection "Momentum Equation" above, products of in-plane velocity gradients are negligible, and the terms

$$\frac{4}{3}\tilde{\mu}\frac{\partial \tilde{u}}{\partial x}\frac{\partial \tilde{u}}{\partial x},\quad \tilde{\mu}\frac{\partial \tilde{v}}{\partial x}\frac{\partial \tilde{v}}{\partial x},\quad \tilde{\mu}\frac{\partial \tilde{u}}{\partial z}\frac{\partial \tilde{w}}{\partial x},\quad \tilde{\mu}\frac{\partial \tilde{w}}{\partial x}\frac{\partial \tilde{w}}{\partial x},$$

$$\tilde{\mu}\frac{\partial \tilde{w}}{\partial x}\frac{\partial \tilde{u}}{\partial z},\quad \tilde{\mu}\frac{\partial \tilde{u}}{\partial z}\frac{\partial \tilde{u}}{\partial z},\quad \tilde{\mu}\frac{\partial \tilde{v}}{\partial z}\frac{\partial \tilde{v}}{\partial z},\quad \frac{4}{3}\tilde{\mu}\frac{\partial \tilde{w}}{\partial z}\frac{\partial \tilde{w}}{\partial z}$$

will be neglected. Applying these simplifications, Eq. 2.57 becomes

$$c_v \frac{\partial\left(\bar{\rho}\tilde{T}\right)}{\partial t} + c_v\left[\frac{\partial\left(\bar{\rho}\widetilde{u}\widetilde{T}\right)}{\partial x} + \frac{\partial\left(\bar{\rho}\widetilde{v}\widetilde{T}\right)}{\partial y} + \frac{\partial\left(\bar{\rho}\widetilde{w}\widetilde{T}\right)}{\partial z}\right] = -\bar{p}\frac{\partial\tilde{u}}{\partial x} - \bar{p}\frac{\partial\tilde{v}}{\partial y} - \bar{p}\frac{\partial\tilde{w}}{\partial z}$$
$$+ \tilde{\mu}\frac{\partial\tilde{u}}{\partial y}\frac{\partial\tilde{u}}{\partial y} + 2\tilde{\mu}\frac{\partial\tilde{u}}{\partial y}\frac{\partial\tilde{v}}{\partial x} + \frac{4}{3}\tilde{\mu}\frac{\partial\tilde{v}}{\partial y}\frac{\partial\tilde{v}}{\partial y} + 2\tilde{\mu}\frac{\partial\tilde{v}}{\partial z}\frac{\partial\tilde{w}}{\partial y} + \tilde{\mu}\frac{\partial\tilde{w}}{\partial y}\frac{\partial\tilde{w}}{\partial y} + \frac{\partial}{\partial y}\left(\tilde{\kappa}\frac{\partial\tilde{T}}{\partial y}\right). \quad (2.58)$$

Applying the averaging filter (Eq. 2.44) in the wall-adjacent layer to Eq. 2.58 gives

$$c_v \frac{\partial\left\{\bar{\rho}\tilde{T}\right\}}{\partial t} + c_v\left(\frac{\partial\left\{\bar{\rho}\widetilde{u}\widetilde{T}\right\}}{\partial x} + \frac{\partial\left\{\bar{\rho}\widetilde{w}\widetilde{T}\right\}}{\partial z}\right) =$$
$$-\frac{c_v}{h}\int_0^h \frac{\partial\bar{\rho}\widetilde{v}\widetilde{T}}{\partial y}dy - \frac{1}{h}\int_0^h \bar{p}\frac{\partial\tilde{u}}{\partial x}dy - \frac{1}{h}\int_0^h \bar{p}\frac{\partial\tilde{v}}{\partial y}dy - \frac{1}{h}\int_0^h \bar{p}\frac{\partial\tilde{w}}{\partial z}dy$$
$$+\frac{1}{h}\int_0^h \tilde{\mu}\frac{\partial\tilde{u}}{\partial y}\frac{\partial\tilde{u}}{\partial y}dy + \frac{2}{h}\int_0^h \tilde{\mu}\frac{\partial\tilde{v}}{\partial x}\frac{\partial\tilde{u}}{\partial y}dy + \frac{4}{3h}\int_0^h \tilde{\mu}\frac{\partial\tilde{v}}{\partial y}\frac{\partial\tilde{v}}{\partial y}dy$$
$$+\frac{2}{h}\int_0^h \tilde{\mu}\frac{\partial\tilde{v}}{\partial z}\frac{\partial\tilde{w}}{\partial y}dy + \frac{1}{h}\int_0^h \tilde{\mu}\frac{\partial\tilde{w}}{\partial y}\frac{\partial\tilde{w}}{\partial y}dy + \frac{\tilde{\kappa}}{h}\left.\frac{\partial\tilde{T}}{\partial y}\right|_h - \frac{\tilde{\kappa}}{h}\left.\frac{\partial\tilde{T}}{\partial y}\right|_0. \quad (2.59)$$

Evaluating the first term on the right-hand side of Eq. 2.59 and applying the no-penetration condition at the wall (i.e., $\tilde{v}|_0 = 0$) gives

$$\frac{c_v}{h}\int_0^h \frac{\partial\bar{\rho}\widetilde{v}\widetilde{T}}{\partial y}dy = \frac{c_v}{h}\left.\bar{\rho}\widetilde{v}\widetilde{T}\right|_h,$$

with $\left.\widetilde{v}\widetilde{T}\right|_h$ provided by the stretched-vortex subgrid-scale model.

As in Chung and Pullin, 2009 [1], it will be assumed that in-plane (i.e., streamwise and spanwise) gradients of averaged quantities can be approximated by values at $y = h$—that is, the wall-normal variation of $\partial\tilde{u}/\partial x$ and $\partial\tilde{w}/\partial z$ is assumed to be small within the wall-adjacent layer. Additionally, the DNS of fully developed compressible channel flows by Coleman et al. [32] shows that "[t]he mean flow is approximately isobaric, and the mean wall-normal pressure gradient is everywhere very small....[T]he magnitude of fluctuations of total temperature and especially pressure are much less

than their mean values." Therefore, $\bar{p}\,(y)$ can justifiably be replaced with $\bar{p}|_h$. The second and fourth r.h.s. terms of Eq. 2.59 thus become

$$\frac{1}{h}\int_0^h \bar{p}\frac{\partial\tilde{u}}{\partial x}dy \approx \bar{p}\frac{\partial\tilde{u}}{\partial x}\bigg|_h$$

and

$$\frac{1}{h}\int_0^h \bar{p}\frac{\partial\tilde{w}}{\partial z}dy \approx \bar{p}\frac{\partial\tilde{w}}{\partial z}\bigg|_h .$$

Applying integration by parts and the no-penetration condition, and since the DNS shows that $\partial p/\partial y \approx 0$, the third r.h.s. term of Eq. 2.59 becomes

$$\frac{1}{h}\int_0^h \bar{p}\frac{\partial\tilde{v}}{\partial y}dy = \frac{\bar{p}\tilde{v}}{h}\bigg|_h - \frac{1}{h}\int_0^h \tilde{v}\frac{\partial\bar{p}}{\partial y}dy \approx \frac{\bar{p}\tilde{v}}{h}\bigg|_h .$$

In the mean, $\partial u/\partial y$ is large near the wall, while $\partial v/\partial y$ and $\partial w/\partial y$ are everywhere small in comparison (although it is acknowledged that $\partial v/\partial y$ reaches a peak compression value at $y/\delta \approx 0.03$—see [32]). Therefore, even accounting for turbulent fluctuations, it can reasonably be assumed that

$$\left(\frac{\partial\tilde{u}}{\partial y}\right)^2 >> \left(\frac{\partial\tilde{v}}{\partial y}\right)^2,$$

$$\left(\frac{\partial\tilde{u}}{\partial y}\right)^2 >> \left(\frac{\partial\tilde{w}}{\partial y}\right)^2,$$

so the fifth r.h.s. term of Eq. 2.59 will be retained, while the seventh and ninth will be neglected. As in Eq. 2.55 for η_0, $\tilde{\mu}\,(y)$ will be replaced with the approximate mean value $\hat{\mu}$—see Eq. 2.46—in the fifth, sixth and eighth r.h.s. terms of Eq. 2.59. The fifth term is therefore simplified to

$$\frac{1}{h}\int_0^h \tilde{\mu}\frac{\partial\tilde{u}}{\partial y}\frac{\partial\tilde{u}}{\partial y}dy \approx \frac{\hat{\mu}}{h}\int_0^h \left(\frac{\partial\tilde{u}}{\partial y}\right)^2 dy.$$

Unfortunately, $\int(\partial\tilde{u}/\partial y)^2\,dy$ cannot be evaluated exactly for an arbitrary velocity gradient. A brief study was performed in which an instantaneous DNS streamwise velocity field [33] was box filtered, using the LES grid spacing as the filter width.

$\int_0^h \left(\partial\tilde{u}/\partial y\right)^2 dy$ was numerically integrated for seven arbitrarily selected, instantaneous, local, filtered profiles; compared to $\int_0^h \left(\partial\tilde{u}/\partial y\right)^2 dy$ for the mean profile, these instantaneous, local profiles showed differences ranging from 3% to 54%. With no better alternative available, however, this term will be approximated by integrating $\int_0^h \left(\partial\langle U\rangle/\partial y\right)^2 dy$ for the compressible law-of-the-wall mean profile (i.e., Van Driest transformation of Eq. 2.61 below), providing a contribution of the correct order of magnitude.

The calculation uses

$$\mathcal{K}_1 = -\frac{0.45K^{1/2}}{2\tau_{12}/u_\tau} \tag{2.60}$$

(Eq. 3.16 in Chung and Pullin, 2009 [1], where K is the subgrid kinetic energy and τ_{12} is a subgrid stress component) to compute dynamically a local Kármán constant $\mathcal{K}_1$ (rather than an empirically derived value), keeping the new wall model parameter-free.

This integration ignores the smooth transition from the linear profile to the logarithmic profile in the buffer layer. That is, the following incompressible, mean profile is assumed:

$$\langle U\rangle_{M=0} = \begin{cases} u_\tau y^+, & y^+ \leq 11 \\ \frac{u_\tau}{\kappa}\ln y^+ + u_\tau F, & y^+ > 11, \end{cases} \tag{2.61}$$

("F" here used in place of the more common "B" to avoid confusion immediately below), to which the Van Driest transformation is applied.

The Van Driest transformation is [16, 34]

$$\frac{A}{U_c}\langle U\rangle_{M=0} = \sin^{-1}\left(\frac{2A^2\langle U\rangle/U_c - B}{\sqrt{B^2+4A^2}}\right) + \sin^{-1}\left(\frac{B}{\sqrt{B^2+4A^2}}\right) \tag{2.62}$$

where

$$A = \sqrt{\frac{\gamma-1}{2}Pr_t M_c^2 \frac{T_c}{T_w}}, \tag{2.63}$$

$$B = \left[1 + Pr_t^{1/2}\frac{\gamma-1}{2}M_c^2\right]\frac{T_c}{T_w} - 1, \tag{2.64}$$

U_c is the channel centerline velocity, M_c is the centerline Mach number, T_c is the centerline temperature, T_w is the isothermal wall temperature, and $Pr_t \approx 0.89$ [34] is the mean turbulent Prandtl number. To calculate $\int_0^h \left(\partial\langle U\rangle/\partial y\right)^2 dy$ for the compressible mean velocity profile, Eq. 2.62 must be inverted to solve for $\langle U\rangle$ in terms of $\langle U\rangle_{M=0}$, which can be approximated by Eq. 2.61.

Rearranging Eq. 2.62 gives

$$\frac{A}{U_c}\langle U\rangle_{M=0} - \sin^{-1}\left(\frac{B}{\sqrt{B^2+4A^2}}\right) = \sin^{-1}\left(\frac{2A^2\langle U\rangle/U_c - B}{\sqrt{B^2+4A^2}}\right) \tag{2.65}$$

or

$$\sin\left[\frac{A}{U_c}\langle U\rangle_{M=0} - \sin^{-1}\left(\frac{B}{\sqrt{B^2+4A^2}}\right)\right] = \frac{2A^2\langle U\rangle/U_c - B}{\sqrt{B^2+4A^2}}. \tag{2.66}$$

Using $\sin(x-y) = \sin x\cos y - \cos x\sin y$ and $\cos\left(\sin^{-1} y\right) = \left(1-y^2\right)^{1/2}$,

$$\sin\left(\frac{A}{U_c}\langle U\rangle_{M=0}\right)\left(1-\frac{B^2}{B^2+4A^2}\right)^{1/2} - \cos\left(\frac{A}{U_c}\langle U\rangle_{M=0}\rangle\right)\left(\frac{B}{\sqrt{B^2+4A^2}}\right) = \frac{2A^2\langle U\rangle/U_c - B}{\sqrt{B^2+4A^2}}, \tag{2.67}$$

or

$$\sin\left(\frac{A}{U_c}\langle U\rangle_{M=0}\right)\left(1-\frac{B^2}{B^2+4A^2}\right)^{1/2}\left(B^2+4A^2\right)^{1/2} - B\cos\left(\frac{A}{U_c}\langle U\rangle_{M=0}\rangle\right) = 2A^2\frac{\langle U\rangle}{U_c} - B. \tag{2.68}$$

Since

$$\left(1-\frac{B^2}{B^2+4A^2}\right)^{1/2}\left(B^2+4A^2\right)^{1/2} = \left(B^2+4A^2-B^2\right)^{1/2} = 2A,$$

Eq. 2.68 becomes

$$2A\sin\left(\frac{A}{U_c}\langle U\rangle_{M=0}\right) - B\cos\left(\frac{A}{U_c}\langle U\rangle_{M=0}\right) + B = 2A^2\frac{\langle U\rangle}{U_c}. \tag{2.69}$$

Finally,

$$\langle U\rangle = \frac{U_c}{A}\sin\left(\frac{A}{U_c}\langle U\rangle_{M=0}\right) - \frac{BU_c}{2A^2}\cos\left(\frac{A}{U_c}\langle U\rangle_{M=0}\right) + \frac{BU_c}{2A^2}. \tag{2.70}$$

For the linear part of the mean profile, therefore,

$$\frac{\partial\langle U\rangle}{\partial y} = \frac{{u_\tau}^2}{\nu}\cos\left(\frac{A{u_\tau}^2 y}{U_c\nu}\right) + \frac{B{u_\tau}^2}{2A\nu}\sin\left(\frac{A{u_\tau}^2 y}{U_c\nu}\right), \tag{2.71}$$

and

$$\begin{aligned}\int_0^{\frac{11\nu}{u_\tau}}\left(\frac{\partial\langle U\rangle}{\partial y}\right)^2 dy &= \int_0^{\frac{11\nu}{u_\tau}}\frac{{u_\tau}^4}{\nu^2}\cos^2\left(\frac{A{u_\tau}^2 y}{U_c\nu}\right)dy + \\ &\quad 2\int_0^{\frac{11\nu}{u_\tau}}\frac{B{u_\tau}^4}{2A\nu^2}\sin\left(\frac{A{u_\tau}^2 y}{U_c\nu}\right)\cos\left(\frac{A{u_\tau}^2 y}{U_c\nu}\right)dy + \\ &\quad \int_0^{\frac{11\nu}{u_\tau}}\frac{B^2{u_\tau}^4}{4A^2\nu^2}\sin^2\left(\frac{A{u_\tau}^2 y}{U_c\nu}\right)dy\end{aligned}$$

$$\begin{aligned}&= \frac{{u_\tau}^4}{\nu^2}\left[\frac{y}{2} + \frac{U_c\nu\sin\left(\frac{2A{u_\tau}^2}{U_c\nu}y\right)}{4A{u_\tau}^2}\right]_0^{\frac{11\nu}{u_\tau}} - \\ &\quad \frac{B{u_\tau}^4}{A\nu^2}\frac{U_c\nu\cos^2\left(\frac{2A{u_\tau}^2}{U_c\nu}y\right)}{2A{u_\tau}^2}\Bigg|_0^{\frac{11\nu}{u_\tau}} + \\ &\quad \frac{B^2{u_\tau}^4}{4A^2\nu^2}\left[\frac{y}{2} - \frac{U_c\nu\sin\left(\frac{2A{u_\tau}^2}{U_c\nu}y\right)}{4A{u_\tau}^2}\right]_0^{\frac{11\nu}{u_\tau}}\end{aligned}$$

$$\begin{aligned}&= \frac{11{u_\tau}^3}{2\nu} + \frac{U_c{u_\tau}^2\sin\left(\frac{22Au_\tau}{U_c}\right)}{4A\nu} - \\ &\quad \frac{BU_c{u_\tau}^2\cos^2\left(\frac{11Au_\tau}{U_c}\right)}{2A^2\nu} + \frac{BU_c{u_\tau}^2}{2A^2\nu} + \\ &\quad \frac{11B^2{u_\tau}^3}{8A^2\nu} - \frac{B^2U_c{u_\tau}^2\sin\left(\frac{22Au_\tau}{U_c}\right)}{16A^3\nu}.\end{aligned} \tag{2.72}$$

For the logarithmic portion of the mean profile,

$$\begin{aligned}\frac{\partial\langle U\rangle}{\partial y} &= \frac{u_\tau}{\kappa y}\cos\left[\frac{A}{U_c}\left(\frac{u_\tau}{\kappa}\ln\frac{yu_\tau}{\nu} + u_\tau F\right)\right] + \\ &\quad \frac{Bu_\tau}{2A\kappa y}\sin\left[\frac{A}{U_c}\left(\frac{u_\tau}{\kappa}\ln\frac{yu_\tau}{\nu} + u_\tau F\right)\right],\end{aligned} \tag{2.73}$$

and

$$\int_{\frac{11\nu}{u_\tau}}^{h}\left(\frac{\partial\langle U\rangle}{\partial y}\right)^2 dy = \frac{{u_\tau}^2}{\kappa^2}\int_{\frac{11\nu}{u_\tau}}^{h}\frac{1}{y^2}\cos^2\left[\frac{A}{U_c}\left(\frac{u_\tau}{\kappa}\ln\frac{yu_\tau}{\nu}+u_\tau F\right)\right]dy + \frac{B{u_\tau}^2}{A\kappa^2}\int_{\frac{11\nu}{u_\tau}}^{h}\frac{1}{y^2}\sin^2\left[\frac{A}{U_c}\left(\frac{u_\tau}{\kappa}\ln\frac{yu_\tau}{\nu}+u_\tau F\right)\right]\cos^2\left[\frac{A}{U_c}\left(\frac{u_\tau}{\kappa}\ln\frac{yu_\tau}{\nu}+u_\tau F\right)\right]dy + \frac{B^2{u_\tau}^2}{4A^2\kappa^2}\int_{\frac{11\nu}{u_\tau}}^{h}\frac{1}{y^2}\sin^2\left[\frac{A}{U_c}\left(\frac{u_\tau}{\kappa}\ln\frac{yu_\tau}{\nu}+u_\tau F\right)\right]dy; \quad (2.74)$$

making use of the identities $\cos^2(x+y) = {}^1\!/_2\left[\cos(2x+2y)+1\right]$ and $\sin^2(x+y) = {}^1\!/_2\left[1-\cos(2x+2y)\right]$ gives

$$\int_{\frac{11\nu}{u_\tau}}^{h}\left(\frac{\partial\langle U\rangle}{\partial y}\right)^2 dy = \frac{{u_\tau}^2}{2\kappa^2}\int_{\frac{11\nu}{u_\tau}}^{h}\frac{1}{y^2}\left[\cos\left(\frac{2Au_\tau}{U_c\kappa}\ln\frac{yu_\tau}{\nu}+\frac{2Au_\tau F}{U_c}\right)+1\right]dy + \frac{B{u_\tau}^2}{A\kappa^2}\int_{\frac{11\nu}{u_\tau}}^{h}\frac{1}{y^2}\sin^2\left[\frac{A}{U_c}\left(\frac{u_\tau}{\kappa}\ln\frac{yu_\tau}{\nu}+u_\tau F\right)\right]\cos^2\left[\frac{A}{U_c}\left(\frac{u_\tau}{\kappa}\ln\frac{yu_\tau}{\nu}+u_\tau F\right)\right]dy + \frac{B^2{u_\tau}^2}{4A^2\kappa^2}\int_{\frac{11\nu}{u_\tau}}^{h}\frac{1}{y^2}\left[1-\cos\left(\frac{2Au_\tau}{U_c\kappa}\ln\frac{yu_\tau}{\nu}+\frac{2Au_\tau F}{U_c}\right)\right]dy \quad (2.75)$$

$$= \frac{2Au_\tau{}^3}{U_c\kappa}\frac{\sin\left(\frac{2Au_\tau}{U_c\kappa}\ln\frac{yu_\tau}{\nu}+\frac{2Au_\tau F}{U_c}\right)}{\frac{8A^2u_\tau{}^2y}{U_c{}^2}+2\kappa^2y}\Bigg|_{\frac{11\nu}{u_\tau}}^{h} -$$

$$\frac{u_\tau{}^2\cos\left(\frac{2Au_\tau}{U_c\kappa}\ln\frac{yu_\tau}{\nu}+\frac{2Au_\tau F}{U_c}\right)}{\frac{8A^2u_\tau{}^2y}{U_c{}^2}+2\kappa^2y}\Bigg|_{\frac{11\nu}{u_\tau}}^{h} - \frac{u_\tau{}^2}{2\kappa^2y}\Bigg|_{\frac{11\nu}{u_\tau}}^{h} -$$

$$\frac{Bu_\tau{}^2}{A\kappa^2}\frac{\sin\left(\frac{2Au_\tau}{U_c\kappa}\ln\frac{yu_\tau}{\nu}+\frac{2Au_\tau F}{U_c}\right)}{8A^2y+2y}\Bigg|_{\frac{11\nu}{u_\tau}}^{h} -$$

$$\frac{Bu_\tau{}^2}{A\kappa^2}\frac{2Au_\tau}{U_c\kappa}\frac{\cos\left(\frac{2Au_\tau}{U_c\kappa}\ln\frac{yu_\tau}{\nu}+\frac{2Au_\tau F}{U_c}\right)}{8A^2y+2y}\Bigg|_{\frac{11\nu}{u_\tau}}^{h} -$$

$$\frac{B^2u_\tau{}^2}{4A^2\kappa^2y}\Bigg|_{\frac{11\nu}{u_\tau}}^{h} - \frac{2AB^2u_\tau{}^3}{U_c\kappa}\frac{\sin\left(\frac{2Au_\tau}{U_c\kappa}\ln\frac{yu_\tau}{\nu}+\frac{2Au_\tau F}{U_c}\right)}{\frac{16A^4u_\tau{}^2y}{U_c{}^2}+4A^2\kappa^2y}\Bigg|_{\frac{11\nu}{u_\tau}}^{h} +$$

$$\frac{B^2u_\tau{}^2\cos\left(\frac{2Au_\tau}{U_c\kappa}\ln\frac{yu_\tau}{\nu}+\frac{2Au_\tau F}{U_c}\right)}{\frac{16A^4u_\tau{}^2y}{U_c{}^2}+4A^2\kappa^2y}\Bigg|_{\frac{11\nu}{u_\tau}}^{h}. \quad (2.76)$$

As discussed previously, the sixth and eighth r.h.s. terms of Eq. 2.59 can be simplified by assuming the in-plane gradients $\partial\tilde{v}/\partial x \neq f(y)$ and $\partial\tilde{v}/\partial z \neq f(y)$ in the wall-adjacent layer, and replacing $\tilde{\mu}(y)$ with $\hat{\mu}$. Thus,

$$\frac{2}{h}\int_0^h \tilde{\mu}\frac{\partial\tilde{v}}{\partial x}\frac{\partial\tilde{u}}{\partial y}dy \approx \frac{2\hat{\mu}}{h}\left.\frac{\partial\tilde{v}}{\partial x}\right|_h\int_0^h\frac{\partial\tilde{u}}{\partial y}dy = \frac{2\hat{\mu}}{h}\frac{\partial\tilde{v}|_h}{\partial x}\,\tilde{u}|_h \quad (2.77)$$

and

$$\frac{2}{h}\int_0^h \tilde{\mu}\frac{\partial\tilde{v}}{\partial z}\frac{\partial\tilde{w}}{\partial y}dy \approx \frac{2\hat{\mu}}{h}\left.\frac{\partial\tilde{v}}{\partial z}\right|_h\int_0^h\frac{\partial\tilde{w}}{\partial y}dy = \frac{2\hat{\mu}}{h}\frac{\partial\tilde{v}|_h}{\partial z}\,\tilde{w}|_h \quad (2.78)$$

with $\tilde{u}|_0 = \tilde{w}|_0 = 0$ due to the no-slip condition.

In the final two r.h.s. terms of Eq. 2.59, $\tilde{\kappa} = c_p\tilde{\mu}/Pr$ is known at $y = 0$ and $y = h$; c_p is the specific heat at constant volume, Pr the Prandtl number. $(\partial\tilde{T}/\partial y)|_h$ is provided by the LES. $(\partial\tilde{T}/\partial y)|_0$ will be addressed in the following.

The unsteady term—i.e., the first term on the left-hand side of Eq. 2.59—will be addressed by following a procedure inspired by that of Chung and Pullin [1], as

summarized in section 2.3.2 above. Defining

$$\theta_0\left(x,z,t\right) \equiv \left.\frac{\partial \tilde{T}}{\partial y}\right|_0, \tag{2.79}$$

and noting that η_0 (Eq. 2.31) and θ_0 are related via the velocity-temperature relation for compressible flows (e.g., the Walz Eq. [17]), it will be assumed, on the basis of dimensional analysis, that

$$\bar{\rho}\tilde{T} = \frac{\tau_w \delta_\nu \theta_0}{{u_\tau}^2} G\left(\theta_0, y^+\right) = \frac{\rho \nu^{1/2} \theta_0}{{\eta_0}^{1/2}} G\left(\theta_0, \frac{y {\eta_0}^{1/2}}{\nu^{1/2}}\right), \tag{2.80}$$

with ρ and ν specified to be the values at the wall. Differentiating 2.80 with respect to θ_0 gives

$$\frac{\partial \bar{\rho}\tilde{T}}{\partial \theta_0} = \frac{\rho \nu^{1/2} \theta_0}{{\eta_0}^{1/2}} \frac{\partial G}{\partial \theta_0} + \frac{\rho \nu^{1/2}}{{\eta_0}^{1/2}} G + \frac{1}{2} \rho \nu^{1/2} \theta_0 G {\eta_0}^{-3/2} \frac{\partial \eta_0}{\partial \theta_0}.$$

Defining $G' \equiv \partial G / \partial y^+$, then,

$$\begin{aligned} \frac{\partial \bar{\rho}\tilde{T}}{\partial \theta_0} &= \frac{\rho \nu^{1/2} \theta_0}{{\eta_0}^{1/2}} G' \frac{\partial y^+}{\partial \eta_0} \frac{\partial \eta_0}{\partial \theta_0} + \frac{\rho \nu^{1/2}}{{\eta_0}^{1/2}} G + \frac{\rho \nu^{1/2} \theta_0}{2{\eta_0}^{3/2}} \frac{\partial \eta_0}{\partial \theta_0} G \\ &= \frac{\rho \nu^{1/2} \theta_0 G' y^+}{2{\eta_0}^{3/2}} \frac{\partial \eta_0}{\partial \theta_0} + \left(\frac{\rho \nu^{1/2}}{{\eta_0}^{1/2}} + \frac{\rho \nu^{1/2} \theta_0}{2{\eta_0}^{3/2}} \frac{\partial \eta_0}{\partial \theta_0} \right) G. \end{aligned} \tag{2.81}$$

Applying the average (Eq. 2.44) in the wall-adjacent layer to Eq. 2.81 gives

$$\frac{\partial \left\{ \bar{\rho}\tilde{T} \right\}}{\partial \theta_0} = \frac{1}{h} \left(\frac{\rho \nu^{1/2}}{{\eta_0}^{1/2}} + \frac{\rho \nu^{1/2} \theta_0}{2{\eta_0}^{3/2}} \frac{\partial \eta_0}{\partial \theta_0} \right) \int_0^h G \, dy + \frac{\rho \nu^{1/2} \theta_0}{2{\eta_0}^{3/2} h} \frac{\partial \eta_0}{\partial \theta_0} \int_0^h y^+ G' dy \tag{2.82}$$

(again, using $\rho = \rho_w$ and $\nu = \nu_w$), or

$$\frac{\partial \left\{ \bar{\rho}\tilde{T} \right\}}{\partial \theta_0} = \frac{\rho}{h^+} \left(\frac{\nu^{1/2}}{{\eta_0}^{1/2}} + \frac{\nu^{1/2} \theta_0}{2{\eta_0}^{3/2}} \frac{\partial \eta_0}{\partial \theta_0} \right) \int_0^{h^+} G \, dy^+ + \frac{\rho \nu^{1/2} \theta_0}{2{\eta_0}^{3/2} h^+} \frac{\partial \eta_0}{\partial \theta_0} \int_0^{h^+} y^+ G' dy^+. \tag{2.83}$$

Using integration by parts,

$$\begin{aligned} \frac{\partial \left\{ \bar{\rho}\tilde{T} \right\}}{\partial \theta_0} = \frac{\rho}{h^+} \left(\frac{\nu^{1/2}}{{\eta_0}^{1/2}} + \frac{\nu^{1/2} \theta_0}{2{\eta_0}^{3/2}} \frac{\partial \eta_0}{\partial \theta_0} \right) \int_0^{h^+} G \, dy^+ + \\ \frac{\rho \nu^{1/2} \theta_0}{2{\eta_0}^{3/2} h^+} \frac{\partial \eta_0}{\partial \theta_0} \left[y^+ G \Big|_0^{h^+} - \int_0^{h^+} G \, dy^+ \right] \end{aligned} \tag{2.84}$$

$$= \frac{\rho\nu^{1/2}}{h^+{\eta_0}^{1/2}} \int_0^{h^+} G \; dy^+ + \frac{\rho\nu^{1/2}\theta_0}{2{\eta_0}^{3/2}h^+} \frac{\partial\eta_0}{\partial\theta_0} h^+ G\left(\theta_0, h^+\right) \tag{2.85}$$

$$= \frac{\rho\nu^{1/2}}{h^+{\eta_0}^{1/2}} \int_0^{h^+} G \; dy^+ + \frac{1}{2\eta_0} \frac{\partial\eta_0}{\partial\theta_0} \left.\bar{\rho}\tilde{T}\right|_h \tag{2.86}$$

since (from Eq. 2.80)

$$\left.\bar{\rho}\tilde{T}\right|_h = \frac{\rho\nu^{1/2}\theta_0}{{\eta_0}^{1/2}} G\left(\theta_0, h^+\right).$$

Thus, a term containing $\int G\, dy$ remains, but the shape function G is unknown, so this term cannot be evaluated exactly. Since it is seen that $\langle T\rangle$ (and, therefore, $\langle\rho\rangle$) varies approximately linearly from $y = 0$ to $y = h$, the mean shape of G must also be approximately linear. The fluctuations of a local, instantaneous G profile can be expected to be unbiased in direction (i.e., neither predominantly positive nor predominantly negative), so integrating should approximately produce the mean "linear" G profile. $\int_0^{h^+} G\, dy^+$ can therefore be approximated as $\left[G\left(\theta_0, 0\right) + G\left(\theta_0, h^+\right)\right]\left[h^+/2\right]$, giving

$$\frac{\partial\left\{\bar{\rho}\tilde{T}\right\}}{\partial\theta_0} \approx \frac{\rho\nu^{1/2}}{2{\eta_0}^{1/2}} \left[G\left(\theta_0, 0\right) + G\left(\theta_0, h^+\right)\right] + \frac{1}{2\eta_0} \frac{\partial\eta_0}{\partial\theta_0} \left.\bar{\rho}\tilde{T}\right|_h$$

$$= \frac{1}{2\theta_0}\left(\left.\bar{\rho}\tilde{T}\right|_0 + \left.\bar{\rho}\tilde{T}\right|_h\right) + \frac{1}{2\eta_0} \frac{\partial\eta_0}{\partial\theta_0} \left.\bar{\rho}\tilde{T}\right|_h. \tag{2.87}$$

To examine $\partial\eta_0/\partial\theta_0$, consider mean flow properties. Near the wall in the viscous sublayer, for incompressible or compressible flows [17],

$$\langle U\rangle = \frac{\tau_w}{\mu} y \tag{2.88}$$

(that is, $\langle U\rangle^+ = y^+$). Using $\mu/\mu_w \approx \left(\langle T\rangle/T_w\right)^{0.76}$ for the variation of viscosity with temperature,

$$\frac{\partial\langle U\rangle}{\partial y} = \frac{\tau_w}{\mu_w}\left(\frac{T_w}{\langle T\rangle}\right)^{0.76}.$$

Thus,

$$\langle\eta_0\rangle \equiv \left.\frac{\partial\langle U\rangle}{\partial y}\right|_0 = \frac{\tau_w}{\mu_w}, \tag{2.89}$$

since $\langle T\rangle = T_w$ at $y = 0$.

Walz's equation for the temperature-velocity relationship in compressible, turbulent flows is

$$\langle T \rangle = T_w + (T_r - T_w)\frac{\langle U \rangle}{U_c} - T_c r \frac{\gamma - 1}{2}\frac{{M_c}^2}{{U_c}^2}\langle U \rangle^2 \tag{2.90}$$

where the recovery temperature is

$$T_r = T_c\left(1 + r\frac{\gamma - 1}{2}{M_c}^2\right) \tag{2.91}$$

and r is the flow-specific recovery factor [17]. Then, using (2.88),

$$\langle \theta_0 \rangle \equiv \left.\frac{\partial \langle T \rangle}{\partial y}\right|_0 = (T_r - T_w)\frac{\tau_w}{\mu_w U_c}. \tag{2.92}$$

Rewriting Eq. (2.88) as

$$\langle \eta_0 \rangle = \frac{\tau_w}{\mu_w}\frac{(T_r - T_w)}{U_c}\frac{U_c}{(T_r - T_w)} = \frac{U_c}{T_r - T_w}\langle \theta_0 \rangle, \tag{2.93}$$

then

$$\frac{\partial \langle \eta_0 \rangle}{\partial \langle \theta_0 \rangle} = \frac{U_c}{T_r - T_w}. \tag{2.94}$$

$\partial \eta_0 / \partial \theta_0$ can therefore be approximated as

$$\frac{\partial \eta_0}{\partial \theta_0} \approx \frac{U_c(x,z,t)}{T_r(x,z,t) - T_w}. \tag{2.95}$$

Finally,

$$\frac{\partial\left\{\bar{\rho}\tilde{T}\right\}}{\partial t} = \frac{\partial\left\{\bar{\rho}\tilde{T}\right\}}{\partial \theta_0}\frac{\partial \theta_0}{\partial t} = \left[\frac{1}{2\theta_0}\left(\left.\bar{\rho}\tilde{T}\right|_0 + \left.\bar{\rho}\tilde{T}\right|_h\right) + \frac{1}{2\eta_0}\frac{\partial \eta_0}{\partial \theta_0}\left.\bar{\rho}\tilde{T}\right|_h\right]\frac{\partial \theta_0}{\partial t}. \tag{2.96}$$

The final l.h.s. terms of Eq. 2.59 will be approximated as

$$\frac{\partial\left\{\bar{\rho}\widetilde{uT}\right\}}{\partial x} \approx \left.\frac{\partial\,\bar{\rho}\widetilde{uT}}{\partial x}\right|_h \quad \text{and} \quad \frac{\partial\left\{\bar{\rho}\widetilde{wT}\right\}}{\partial z} \approx \left.\frac{\partial\,\bar{\rho}\widetilde{wT}}{\partial z}\right|_h,$$

analogous to the corresponding terms in Chung and Pullin, 2009 [1], with $\widetilde{uT}$ and $\widetilde{wT}$ provided by the stretched-vortex subgrid-scale model.

The resulting averaged LES energy equation thus provides an ODE for the time evolution of θ_0:

$$c_v \left[\frac{1}{2\theta_0} \left(\bar{\rho}\tilde{T}|_0 + \bar{\rho}\tilde{T}|_h \right) + \frac{1}{2\eta_0} \frac{U_\infty}{T_r - T_w} \bar{\rho}\tilde{T}|_h \right] \frac{\partial \theta_0}{\partial t} + c_v \left(\frac{\partial \bar{\rho}\widetilde{uT}|_h}{\partial x} + \frac{\partial \bar{\rho}\widetilde{wT}|_h}{\partial z} \right) =$$
$$- \frac{c_v}{h} \bar{\rho}\widetilde{vT}\Big|_h - \bar{p}\,\frac{\partial \tilde{u}}{\partial x}\Big|_h - \frac{\bar{p}\tilde{v}}{h}\Big|_h - \bar{p}\,\frac{\partial \tilde{w}}{\partial z}\Big|_h +$$
$$\frac{\hat{\mu}}{h} \left[\int_0^{\frac{11\nu}{u_\tau}} \left(\frac{\partial \langle U \rangle}{\partial y} \right)^2 dy + \int_{\frac{11\nu}{u_\tau}}^{h} \left(\frac{\partial \langle U \rangle}{\partial y} \right)^2 dy \right] +$$
$$\frac{2\hat{\mu}}{h} \left(\frac{\partial \tilde{v}|_h}{\partial x} \tilde{u}|_h + \frac{\partial \tilde{v}|_h}{\partial z} \tilde{w}|_h \right) + \frac{c_p \tilde{\mu}}{h\,Pr} \frac{\partial \tilde{T}}{\partial y}\Big|_h - \frac{c_p \tilde{\mu}|_0}{h\,Pr} \theta_0 \quad (2.97)$$

with the r.h.s. terms in square brackets calculated as in Eq. 2.72 and Eq. 2.76. As with the η_0 model, the opposite sign must be used for the terms $\partial\tilde{v}/\partial x|_h$, $\partial\tilde{v}/\partial z|_h$, $\partial\tilde{T}/\partial y\Big|_h$ and $\tilde{v}|_h$ when solving Eq. 2.97 at the top wall.

The relative orders of magnitude of the r.h.s. terms—keeping their original designations as terms 1, 2, 3, 4, 5, 6, 8, 10 and 11—were briefly examined for a compressible simulation. Calculating long time averages (tens of flow-throughs) of one bottom-wall and one top-wall location, for a particular channel height and set of flow conditions, gave the magnitudes indicated in Table 2.1. The absolute orders of magnitude would change with run conditions (Mach number, Reynolds number, channel height, etc.), but their relative orders of magnitude would be expected to remain unchanged. Thus, for the sake of computational efficiency, there could be value in evaluating the ability to neglect terms 6, 8, and possibly 10; such an evaluation has not been performed to date.

The three-stage Runge-Kutta time integration algorithm used in the flow solver was also used to dynamically calculate the local, instantaneous θ_0 at each time step in each wall-adjacent cell in the computational grid, and

$$\kappa\,\theta_0 = \kappa\,\frac{\partial \tilde{T}}{\partial y}\Big|_0 \quad (2.98)$$

is the heat flux boundary condition at the wall.

Table 2.1: Orders of magnitude of right-hand side terms in Eq. 2.97

Term	1	2	3	4	5	6	8	10	11
Magnitude	10^{-3}	10^{-3}	10^{-3}	10^{-2}	10^{-2}	10^{-7}	10^{-6}	10^{-4}	10^{-2}

2.4 Numerical Method

The research presented here utilized a version of AMROC [35], a compressible, finite-difference flow solver with adaptive mesh refinement (AMR) on uniform grids. This code has been adapted for LES via incorporation of the compressible, stretched vortex-based subgrid-scale model of Kosović, Pullin and Samtaney [26], as described briefly in section 2.2.3. This was an updated version of AMROC from that used in Pantano et al., 2008 [21], incorporating into the flow solver the high-order-accuracy, second-order-derivative finite-difference approximations developed in [36]. The flow solver specifies all variables at the grid cell centers; a wall-adjacent cell "rests" on the wall, such that the first cell center (i.e., grid point $j = 1$) is at a height $y = \Delta y/2$. Three-stage Runge-Kutta time integration was employed; no AMR was used.

For low-Mach number simulations, a flow with a centerline mean Mach number $M = 0.15$ was considered low enough to minimize the effects of compressibility, allowing comparison to the incompressible DNS of Hoyas and Jiménez at $Re_\tau = 2003$ [9]. Compressible-flow simulations were performed at $M = 0.7$ for comparison to the DNS of Wei and Pollard at $Re_\tau = 186$ [37].

2.4.1 Initial Conditions

For a specified friction Reynolds number Re_τ, bulk Mach number M, bulk density ρ, wall viscosity μ_w (with initial wall kinematic viscosity $\nu_w = \mu_w/\rho$), and channel half-height δ, the simulation initial conditions (ICs) were generated via the following

procedure. The mean centerline velocity U_c is estimated by iteratively solving Eq. 2.70 at $y = \delta$. At each grid point, the mean streamwise velocity is then set via Eq. 2.70, with randomized sinusoidal perturbations superimposed. The spanwise and vertical velocity ICs specify a zero-mean profile across the channel height with similar local perturbations. These initial mean profiles, with minimum and maximum perturbations, are shown in Fig. 2.3; a representative IC contour plot (for a sample $64 \times N_y \times 64$-cell grid) in a horizontal plane is displayed in Fig. 2.4.

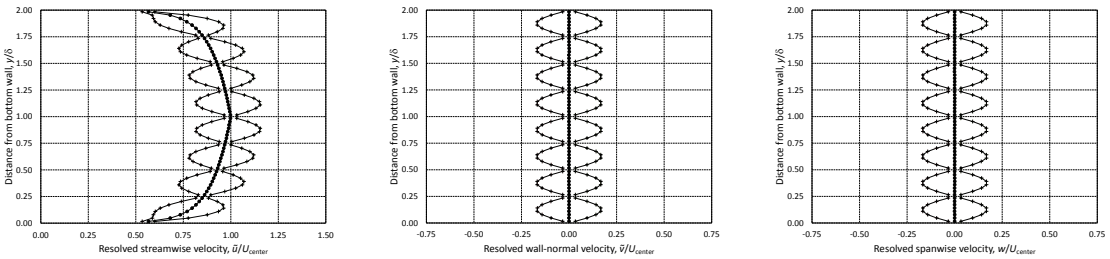

Figure 2.3: Initial conditions: mean profiles (•) with minimum and maximum perturbations (+), for $\tilde{u}$, $\tilde{v}$ and $\tilde{w}$

The bulk velocity $\bar{U}$ is estimated by numerically integrating the Van Driest-transformed log-law. The wall sound speed is then $c_w = \bar{U}/M$, as in [32, 37]. The constant pressure IC is $p = c^2\rho/\gamma$, and the fixed wall temperature for the simulation is $T_w = p/\rho R$, also used as the constant temperature IC.

The initial condition in the bottom half of the channel was reflected to the top half of the channel. This IC would initially produce bottom-top symmetry in the flow-field, but after a few flow-throughs, the bottom-wall η_0 and θ_0 would naturally diverge from the top-wall η_0 and θ_0 (due to numerical round-off error), resulting in a genuinely chaotic turbulent flowfield throughout the channel.

The characteristic friction velocity of the flow is $u_{\tau,0} = Re_\tau \nu_w/\delta$, and the nominal wall shear stress is $\tau_{w,0} = \rho {u_{\tau,0}}^2$. The mean streamwise pressure gradient used to drive

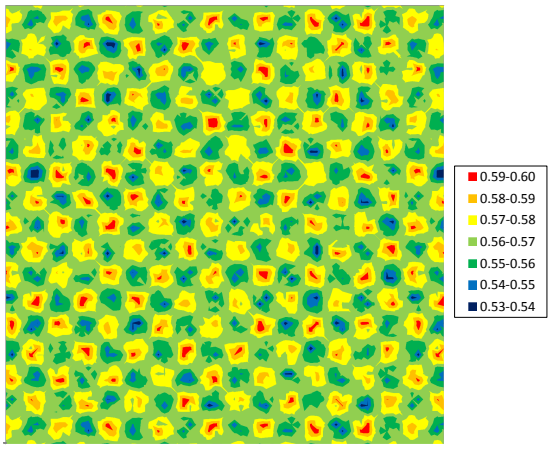

Figure 2.4: Initial condition: contours of resolved streamwise velocity $\tilde{u}/U_{center}$ in the horizontal plane $y = \Delta y/2$

the channel flow is then $dp/dx = -\tau_w/\delta$—i.e., the shear stress–pressure gradient relation for an incompressible, laminar Poiseuille flow [6]. This constant pressure gradient does not produce a strictly constant bulk velocity in the channel, but for low-Mach number LES, the variation in $\bar{U}$ was within $\pm 0.014\%$ and considered negligible.

The local η_0 initial condition is set by solving Eq. 2.70 for u_τ based on the local $\tilde{u}$ IC at the first grid point, and then $\eta_0 = {u_\tau}^2/\nu$. The local θ_0 IC is then set by using Eq. 2.93.

2.4.2 Boundary Conditions

Periodic boundary conditions (BCs) were enforced in the streamwise and spanwise directions in order to simulate a fully developed channel. The local, instantaneous wall shear stress $\tau_w = \mu_w \eta_0$ predicted by the wall model was used in the same method as in Pantano et al., 2008 [21]: for relatively high Reynolds number flows and coarse grids, where "the majority of flow features associated with near-wall structures" are contained within a thin sublayer of the first (wall-adjacent) grid cell, $\bar{\rho}\tilde{u}\tilde{v} - \bar{\sigma}_{12} + \tau_{12} \approx$

$-\tau_w$ at the wall—refer to Eq. 2.8.

The flow solver applies boundary conditions for the conserved variables via use of "ghost cells" outside the boundaries of the computational domain. The values of the streamwise velocity $\tilde{u}$ in the ghost cells across the walls were set by extrapolating from $\tilde{u}$ values inside the domain, as described in [21]; this is necessary to allow computation of the resolved strain rate tensor (used by the subgrid-scale model to compute τ_{ij}) without modifying the finite difference operators when approaching the walls.

Ghost-cell $\tilde{v}$ and $\tilde{w}$ values were set by reflecting and reversing values across the wall, such that spanwise no-slip and no-penetration conditions resulted at the wall.

For comparing the two wall models of sections 2.3.1 and 2.3.2 in low-Mach number ("incompressible") simulations, an adiabatic wall condition was enforced for the energy equation by reflecting the temperature—and thus internal energy—from the computational cells into the corresponding ghost cells. Even at $M = 0.15$, the adiabatic-wall condition resulted in a steady temperature rise in the channel, as seen in Fig. 2.5; admittedly, this temperature rise was very slow—0.05% per flow-through—and essentially stationary flow statistics could be computed for such simulations. But the rate of temperature rise would increase with increasing Mach numbers, as described in section 1.3.2, and the channel would never converge to a statistically stationary state. Thus, for simulations employing the present wall model, isothermal walls were modeled by setting all ghost-cell temperatures to the constant T_w and replacing the numerical calculation of $\kappa\,(\partial T/\partial y)$ at the wall with $\kappa_w\theta_0$; correct implementation is verified, as near-wall temperatures fluctuate about a constant mean value over time—see Fig. 2.6.

From the finding in [32] that mean wall-normal pressure gradients remain small in compressible channel flows, ghost-cell densities were set such that the resulting ghost-cell pressures $p = \rho R T_w$ would mirror the pressures in the computational domain, producing a local $\partial p/\partial y = 0$ condition. These ghost-cell specifications are depicted in Fig. 2.7.

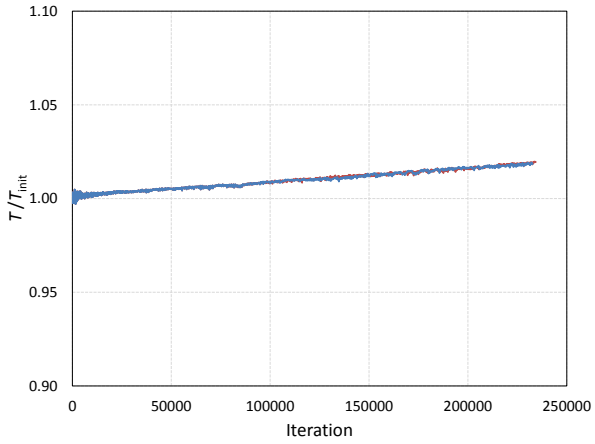

Figure 2.5: Temperature histories over 40 flow-throughs: one bottom wall-adjacent cell (red) and one top wall-adjacent cell (blue), $M = 0.15$, adiabatic-wall boundary condition

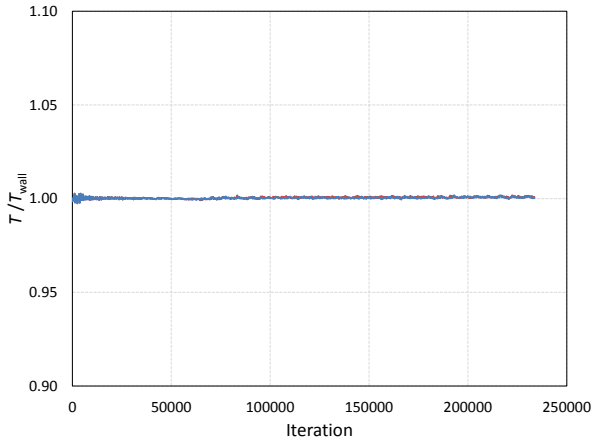

Figure 2.6: Temperature histories over 40 flow-throughs: one bottom wall-adjacent cell (red) and one top wall-adjacent cell (blue), $M = 0.15$, isothermal-wall boundary condition

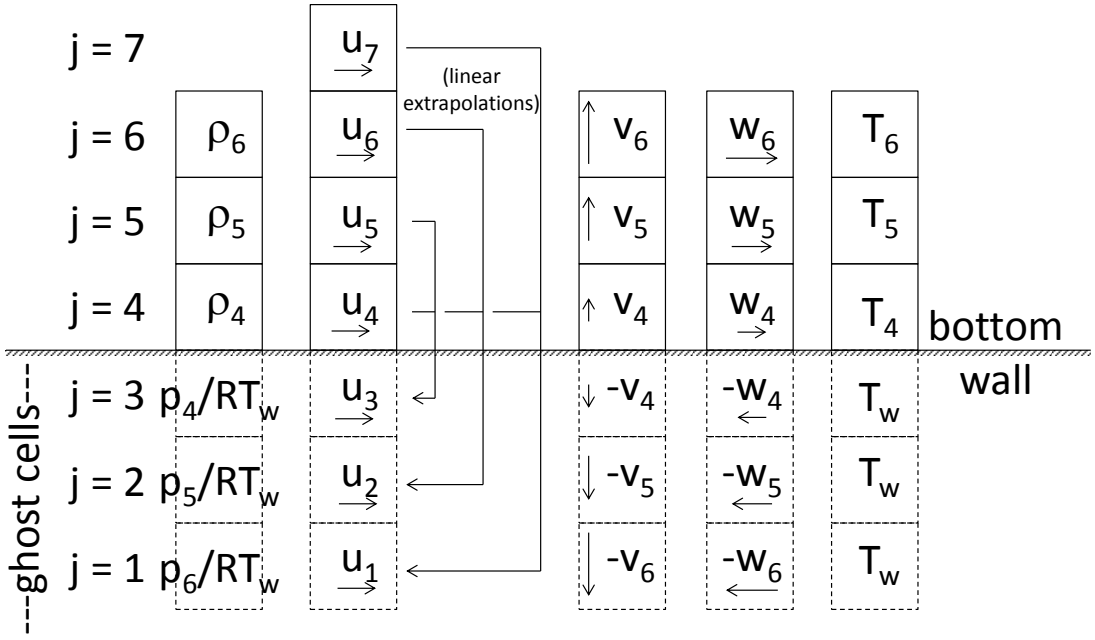

Figure 2.7: Specification of ghost-cell properties to apply boundary conditions

2.4.3 Simulation Conditions

Large-eddy simulations of turbulent channel flow, using the incompressible wall models of Pantano et al. [21] and of Chung and Pullin [1] and the present compressible wall model, were performed at Mach number $M = 0.15$ and friction Reynolds numbers $Re_\tau = 2003$, 2×10^4, 2×10^5, and 2×10^6, for comparison with the incompressible DNS of Hoyas and Jiménez at $Re_\tau = 2003$ [9]; and with the compressible model at $M = 0.7$, $Re_\tau = 186$, 2×10^3, 2×10^4, and 2×10^5, for comparison to the $M = 0.7$, $Re_\tau = 186$ DNS of Wei and Pollard [37]. AMROC is not a non-dimensionalized code, so channel height was varied with Reynolds number such that bulk densities, ini-

tial pressures, and wall temperatures approximately matched sea-level, standard-day conditions—primarily for the purpose of allowing use of Sutherland's law or the 0.76 power law to relate viscosities and temperatures. (Note, however, that calculations of non-dimensionalized turbulent flow statistics such as mean velocity $\langle\tilde{u}\rangle^+$, turbulent intensity u'^+, Reynolds shear stress $\langle uv\rangle^+$ and turbulence kinetic energy k/u_τ^2 are insensitive to selection of channel height.)

Uniform cartesian grids (i.e., $\Delta x = \Delta y = \Delta z$) were used; AMROC does not permit variations in grid point spacing or clustering of grid points near walls. Therefore, the recommendation of Kawai and Larsson [38] could not be followed: to fix the location (height above the wall) at which the wall model receives input from the LES, and refine the near-wall mesh until modeling errors in the first few grid points are minimized [38]. At the large Reynolds numbers simulated on fixed-resolution grids, where the first grid point can be hundreds or thousands of wall units off the wall, the ability of the wall model to predict inner-layer effects based on outer properties is therefore significantly taxed.

Computational domain sizes utilized were $8\pi\delta \times 2\delta \times 3\pi\delta$ (streamwise $\times$ wall-normal $\times$ spanwise), matching that of Hoyas and Jiménez [9], and a somewhat truncated $16\delta \times 2\delta \times 8\delta$, as will be described in the following chapter. Grids used 32 grid points (or, in one study, 46) across the channel height. Simulations were carried out through 40 flow-throughs, based on bulk velocity and channel length, with solutions confirmed to be converged with respect to time.

Chapter 3

RESULTS

3.1 LES of Low-Mach Number Channel Flow Using Pantano et al. Wall Model

The law of the wall-based wall treatment described in section 2.3.1 ($\kappa = 0.4$, $B = 5.0$) was used in AMROC to perform a baseline large-eddy simulation of a turbulent channel flow. The computational domain was $8\pi\delta \times 2\delta \times 3\pi\delta$ (streamwise $\times$ wall-normal $\times$ spanwise dimensions), matching the DNS domain size used by Hoyas and Jiménez [9], with a grid of $402 \times 32 \times 150$ equally spaced grid points centered in cubical cells. The friction Reynolds number was $Re_\tau = 2003$, as in the DNS of [9], to which the LES results were compared.

Because turbulent fields are non-repeatable, analysis of turbulence involves calculation of ensemble averages. Such averages were calculated over each 402×150-cell horizontal plane, and over nine instantaneous time-output "snapshots" once stationary flow was achieved. The simulations performed throughout this study converged to a statistically stationary state within 12-20 flow-throughs, and a total of 40 flow-throughs were typically performed. For low-Mach number turbulent channel flows, the turbulence statistics of interest include the mean (streamwise) velocity profile; the turbulent intensities, u', v' and w'; and the Reynolds shear stress $\langle uv \rangle$. Recall that $u \equiv U - \langle U \rangle$; then $u' \equiv \langle u^2 \rangle^{1/2}$ (i.e., the root-mean-square of the velocity fluctuations in a horizontal plane). The turbulent intensities were normalized by the friction velocity, e.g. $u'^+ \equiv u'/u_\tau$; the Reynolds shear stress was normalized as $\langle uv \rangle^+ \equiv \langle uv \rangle / {u_\tau}^2$.

The results of this baseline LES are compared with DNS [9] in Figures 3.1 and 3.2. As in Pantano et al., 2008 [21], the results match the DNS well, but with some

improvement in the mean velocity profile near the center of the channel. The simulation somewhat underpredicts the wall-normal and spanwise turbulent intensities, but the results are quite good considering the large grid spacing employed; a simulation using the finer $578 \times 46 \times 216$-cell grid of [21] produces turbulent intensity predictions similar to the predictions reported there, but at a 328% computational penalty over this coarse-grid simulation.

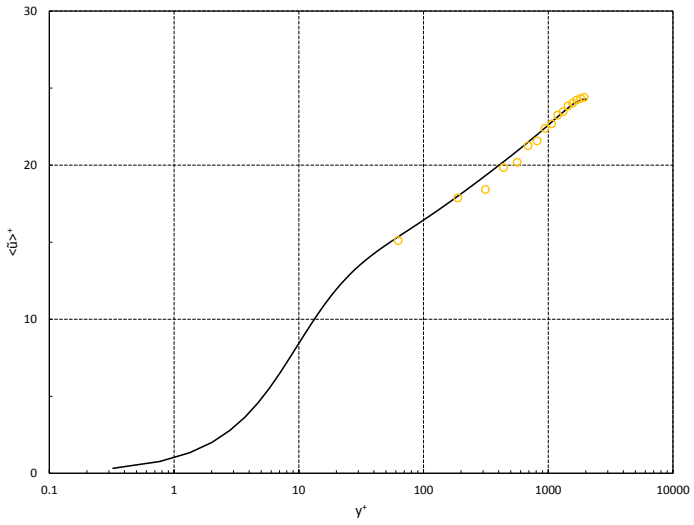

Figure 3.1: $M = 0.15$, $Re_\tau = 2003$ mean velocity profile of the baseline LES using the wall model of Pantano et al., 2008 [21], described in Sec. 2.3.1 ($\circ$), compared with the incompressible DNS results of Hoyas and Jiménez, 2006 [9] (—)

The LES turbulence kinetic energy $k \equiv \langle u_i u_i \rangle / 2$ calculation is compared to the DNS result in Fig. 3.3. The match is very good. Even on this coarse grid, this $Re_\tau = 2003$ simulation resolves 79% of the calculated total turbulence kinetic energy.

The $8\pi\delta \times 2\delta \times 3\pi\delta$ computational domain matched that used by Hoyas and Jiménez [9] for their pseudo-spectral DNS code. For the finite-difference code employed in the present research, it was expected that a smaller, $16\delta \times 2\delta \times 8\delta$ domain could work

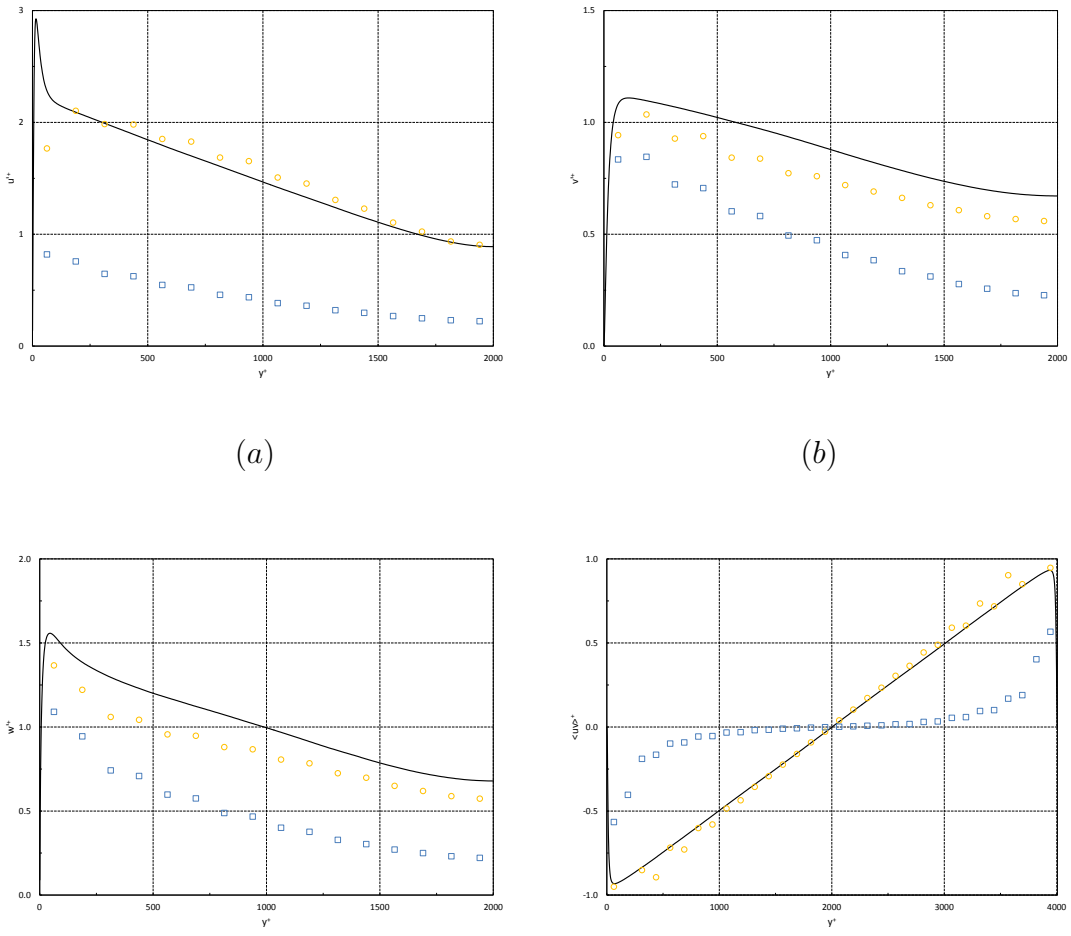

(a) (b)

(c) (d)

Figure 3.2: $M = 0.15$, $Re_\tau = 2003$ turbulent statistics of the baseline LES using the wall model of Pantano et al., 2008 [21], described in Sec. 2.3.1, compared with the incompressible DNS results of Hoyas and Jiménez, 2006 [9]: (a) streamwise intensity; (b) wall-normal intensity; (c) spanwise intensity; (d) Reynolds shear stress (∘ total, □ subgrid, — DNS)

well. The simulation described above was therefore repeated on a $256 \times 32 \times 128$-cell grid to 40 flow-throughs, and results were essentially indistinguishable visually from

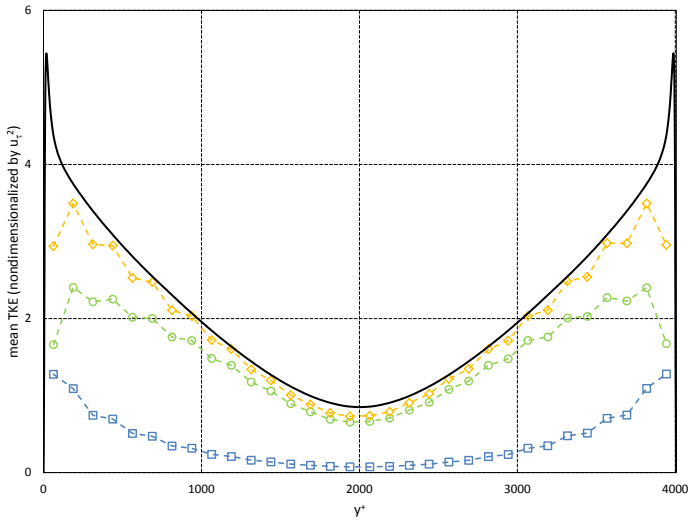

Figure 3.3: $M = 0.15$, $Re_\tau = 2003$ turbulence kinetic energy profile of the baseline LES using the wall model of Pantano et al., 2008 [21], described in Sec. 2.3.1, compared with the incompressible DNS results of Hoyas and Jiménez, 2006 [9] ($\circ$ resolved, $\square$ subgrid, $\diamond$ total, — DNS)

those in Fig. 3.1, Fig. 3.2 and Fig. 3.3. Because of the smaller cell count (1.05 million versus 1.93 million) and the 36.3% shorter channel spanwise length, simulations on this grid require only about 35% of the computational time to complete one flow-through than on the coarse grid described above. For this reason, this more efficient $256 \times 32 \times 128$-cell grid was used for all remaining simulations in the present research.

3.2 LES of Low-Mach Number Channel Flow Using Chung and Pullin Wall Model

3.2.1 Computational Details

The parameter-free wall model of Chung and Pullin [1], described in Sec. 2.3.2, was implemented in AMROC and tested in simulations of low-Mach number channel

flows. Equation 2.40 was solved numerically via the same three-stage Runge-Kutta time integration scheme used by the AMROC flow solver. h was taken to be the height of the first grid point, $h = \Delta y/2$. The stretched-vortex subgrid-scale model provided $\widetilde{uu}$, $\widetilde{uv}$ and $\widetilde{uw}$. Lateral (x and z) gradients were computed via second-order central differences; wall-normal (y) gradients were computed via second-order one-sided differences. Top-wall η_0 calculations were modified such that the same wall shear stress would be predicted at both walls if the flow in the top half of the channel mirrored that in the bottom half. That is, the sign was changed for the terms $\widetilde{uv}|_h$ and $(\partial\tilde{u}/\partial y)|_h$ in Eq. 2.40 for top-wall calculations.

The η_0 initial condition (IC) was $\eta_0 = {u_\tau}^2/\nu$, with u_τ the local value that solves $\tilde{u}^+ = \ln(y^+)/\kappa + B$ for the $\tilde{u}$ IC at each wall-adjacent grid point. It was typically seen that, in this implementation, η_0 would remain well behaved, fluctuating about expected values, for many thousands of iterations, and then, at an apparently random location in the computational domain, diverge rapidly, quickly causing non-physical flow conditions (e.g., negative pressures) in a localized area. To prevent this η_0 divergence, the following procedure was developed.

As AMROC is a parallelized code, a multi-processor run divides the computational mesh into "patches," each assigned to a different processor. Each patch spans the channel from bottom to top wall. In each patch, a single η_0 value near the patch center was set dynamically via the law of the wall-based approach of the baseline code, as described in section 2.3.1; at all other grid points, η_0 was set via numerical solution of Eq. 2.40. Then, the η_0 value at each grid point was replaced by the average value of the nine grid points in the local 3×3-grid-point square. (This same approach, employing the Van Driest-transformed log law, was utilized with the new, compressible wall model.)

After each Runge-Kutta update, this locally averaged η_0 value was used to calculate $\tau_w = \mu\eta_0$, which was then used as the boundary condition in place of the law of the wall-based τ_w employed by the baseline code. For calculations on the

$256 \times 32 \times 128$-cell grid using 128 processors, this means that $< 0.4\%$ of η_0 values were set by the law of the wall-based calculation—a small enough percentage to justifiably assume that the replacement calculation had little influence on the overall behavior of the Chung and Pullin wall model, beyond improving its robustness in the present implementation.

3.2.2 Results

Channel flow simulations were performed at $Re_\tau = 2003$, $Re_\tau = 2\times10^4$, $Re_\tau = 2\times10^5$ and $Re_\tau = 2 \times 10^6$ on the fixed-resolution $256 \times 32 \times 128$-cell coarse grid. The $Re_\tau = 2003$ results are again compared with the DNS of Hoyas and Jiménez [9] in Fig. 3.4, Fig. 3.5 and Fig. 3.6. Results are generally comparable to the baseline results of the previous section, with the mean velocity profile somewhat better near the wall and somewhat worse near the middle of the channel than the baseline; with slight improvements to u', v' and w'; and with a very good match to the turbulence kinetic energy profile (with 78% of the calculated total k resolved by the LES). Again, accounting for the use of only 32 grid points across the channel height—compared to 633 in the direct simulation—these results are excellent.

At the higher friction Reynolds numbers, progressively more of the turbulence scales are modeled in the LES, and the quality of the subgrid-scale and wall models becomes ever more critical to the quality of the simulation results. Fig. 3.7, comparing the mean velocity profiles to the log-law profile, indicates the effectiveness of the stretched-vortex sgs model and the wall model developed by Chung and Pullin. At $Re_\tau = 2\times10^6$, only 44% of the calculated total k is resolved, with 56% being calculated by the sgs model; this speaks further to the quality of the model employed.

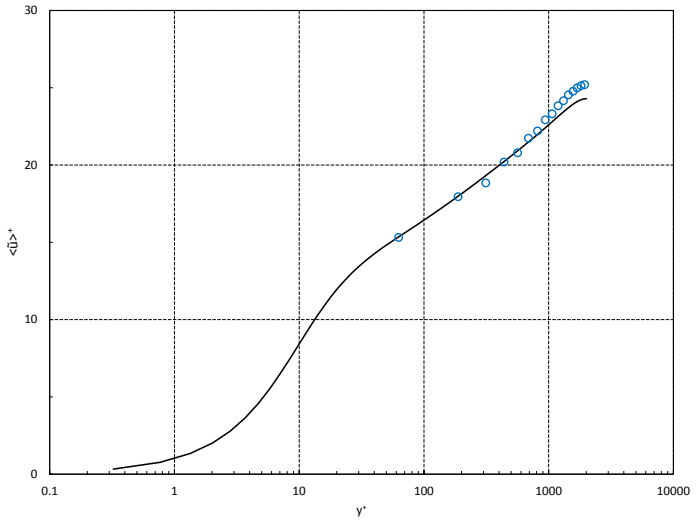

Figure 3.4: $M = 0.15$, $Re_\tau = 2003$ mean velocity profile of the LES using the wall model of Chung and Pullin, 2009 [1], described in Sec. 2.3.2 (∘), compared with the incompressible DNS results of Hoyas and Jiménez, 2006 [9] (—)

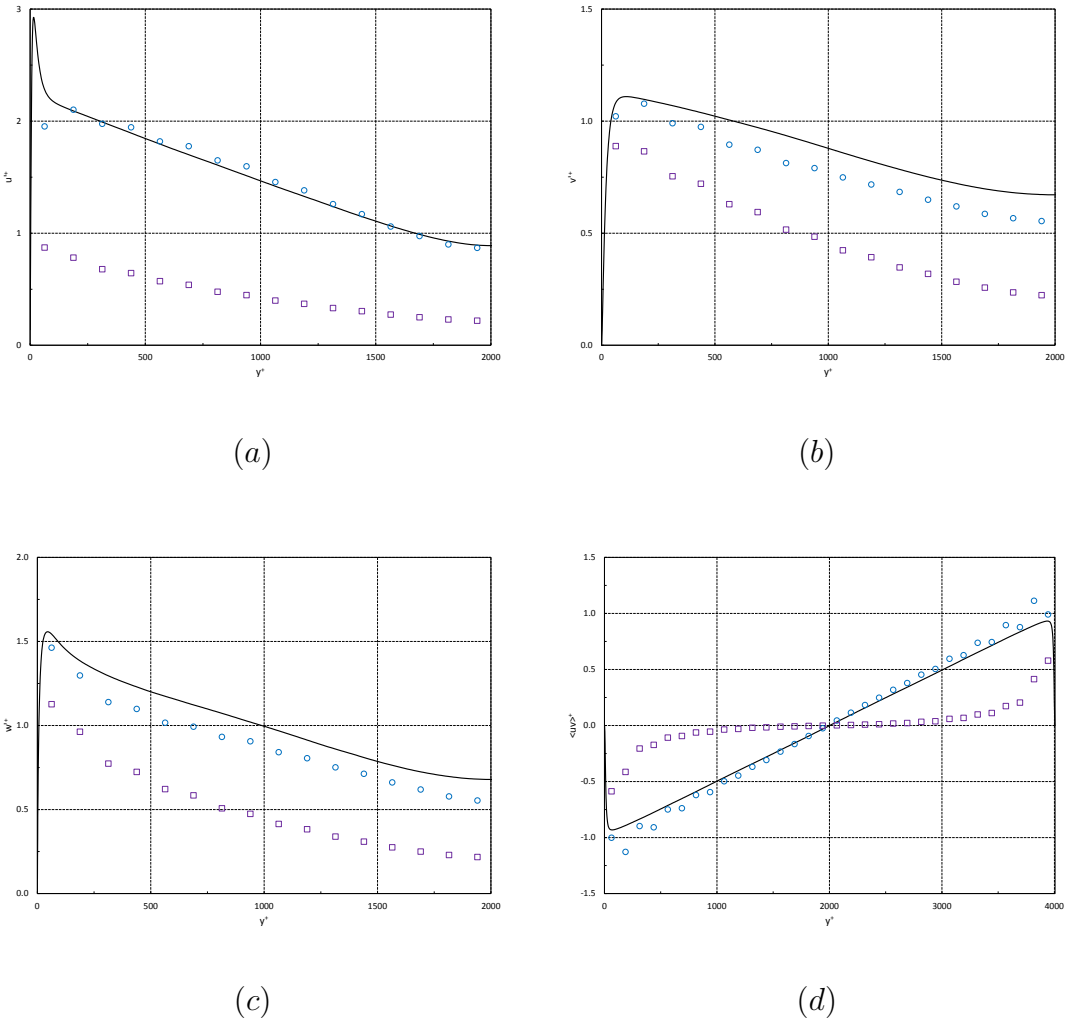

(a) (b)

(c) (d)

Figure 3.5: $M = 0.15$, $Re_\tau = 2003$ turbulent statistics of the LES using the wall model of Chung and Pullin, 2009 [1], described in Sec. 2.3.2, compared with the incompressible DNS results of Hoyas and Jiménez, 2006 [9]: (a) streamwise intensity; (b) wall-normal intensity; (c) spanwise intensity; (d) Reynolds shear stress (∘ total, □ subgrid, — DNS)

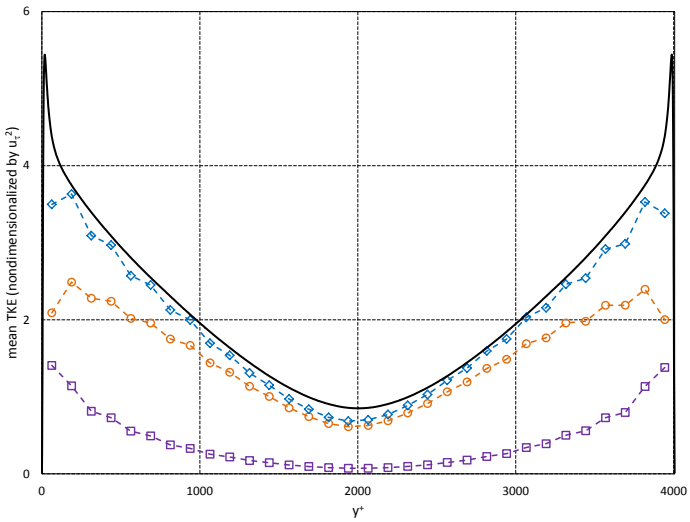

Figure 3.6: $M = 0.15$, $Re_\tau = 2003$ turbulence kinetic energy profile of the LES using the wall model of Chung and Pullin, 2009 [1], described in Sec. 2.3.2, compared with the incompressible DNS results of Hoyas and Jiménez, 2006 [9] ($\circ$ resolved, $\square$ subgrid, $\diamond$ total, — DNS)

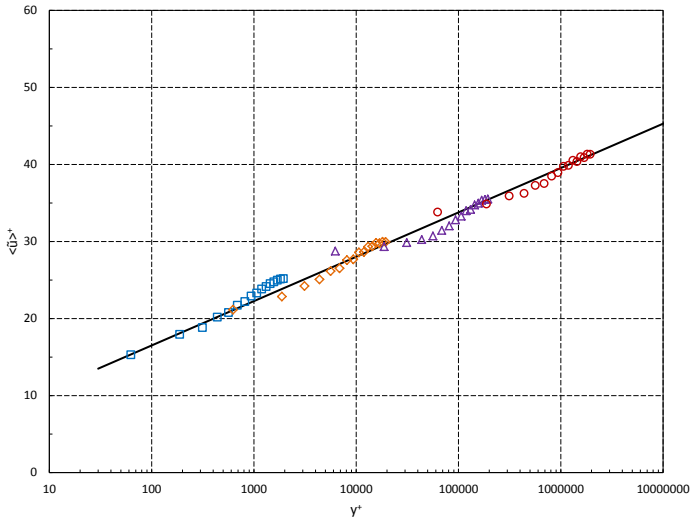

Figure 3.7: Mean velocity profiles for LES using the wall model of Chung and Pullin [1] in AMROC, Re_τ spanning three orders of magnitude

3.3 LES of Low-Mach Number Channel Flow Using the Present Wall Model

Large-eddy simulations of $M = 0.15$ turbulent channel flows using the present wall model (section 2.3.3) were performed over a three-order-of-magnitude range of friction Reynolds numbers on a fixed, 256×32×128-cell, uniform mesh (computational domain size $16\delta \times 2\delta \times 8\delta$, where δ is the channel half-height). $Re_\tau = 2003$ results were compared to the incompressible direct numerical simulation of Hoyas and Jiménez at the same friction Reynolds number [9]. Table 3.1 lists run parameters for the four $M = 0.15$ large-eddy simulations, including friction Reynolds number, Re_τ; channel half-height, δ; friction velocity, u_τ; location of the first grid point, y_1^+; wall temperature, T_w; and pressure initial condition, p_{init}. The percentage of turbulence kinetic energy k resolved in each simulation is also listed. For all simulations, the bulk velocity was $\rho = 1.225$ kg/m^3 and the wall viscosity was $\mu = 1.73 \times 10^{-5}$ kg/m $\cdot$ s.

Fig. 3.8 compares the mean velocity profile of the $Re_\tau = 2003$ simulation, using the compressible wall model, to the LES of Chung and Pullin [1] and the DNS of Hoyas and Jiménez [9]. The mean profile matches the DNS reasonably well; the compressible wall model (using 32 grid points across the channel height) slightly outperforms the Chung and Pullin result (48 grid points) near the wall, but does not predict the mean

Table 3.1: Run parameters of the $M = 0.15$ LES

Re_τ	δ (m)	u_τ (m/s)	y_1^+	T_w (K)	p_{init} (kPa)	$k_{resolved}/k$
2003	0.0136	2.08	63	223	78	78%
2×10^4	0.16	1.77	625	257	90	55%
2×10^5	2.0	1.41	6250	241	85	53%
2×10^6	23.0	1.23	62,500	252	88	53%

velocity as well near the middle of the channel. Still, considering the extremely coarse grid used here—particularly in light of the fact that the DNS used 633 points across the channel height, with clustering near the wall—this result is quite good, and as in other simulations using the stretched-vortex subgrid-scale model [21, 1], an expected, non-logarithmic mid-channel wake (or velocity defect) region is predicted.

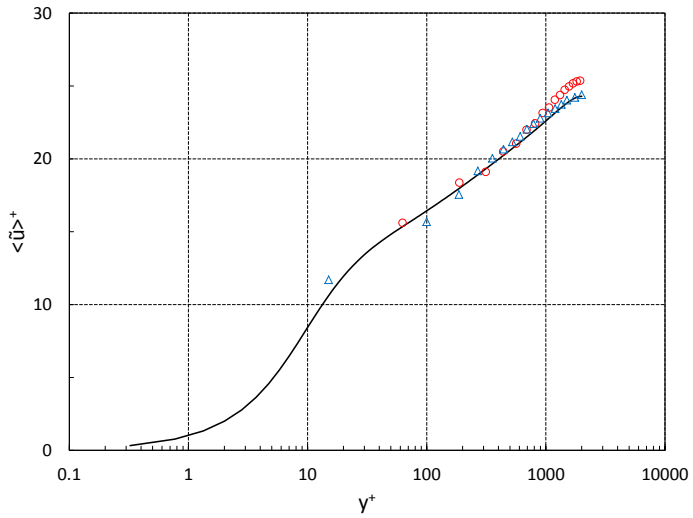

Figure 3.8: $M = 0.15$, $Re_\tau = 2003$ mean velocity profile using the compressible wall model ($\circ$), compared with the LES of Chung and Pullin [1] ($\triangle$) and the DNS of Hoyas and Jiménez [9] (—)

In Fig. 3.9, the turbulent intensities and Reynolds shear stress profiles of the present LES are presented. All results match the DNS quite well, especially considering the large mesh spacing employed. Compared with the LES of Chung and Pullin [1], the compressible wall model improves the u' and $\langle uv \rangle$ profiles slightly, and significantly improves the v' prediction; this latter result is likely due to the wall-normal velocity boundary condition used by Chung and Pullin: $\tilde{v} = 0$ at a lifted "virtual" wall rather than at the physical wall [1]. In the present implementation, this is avoided

by applying the no-penetration boundary condition at the wall. The quality of the w' predictions of the two wall models is similar.

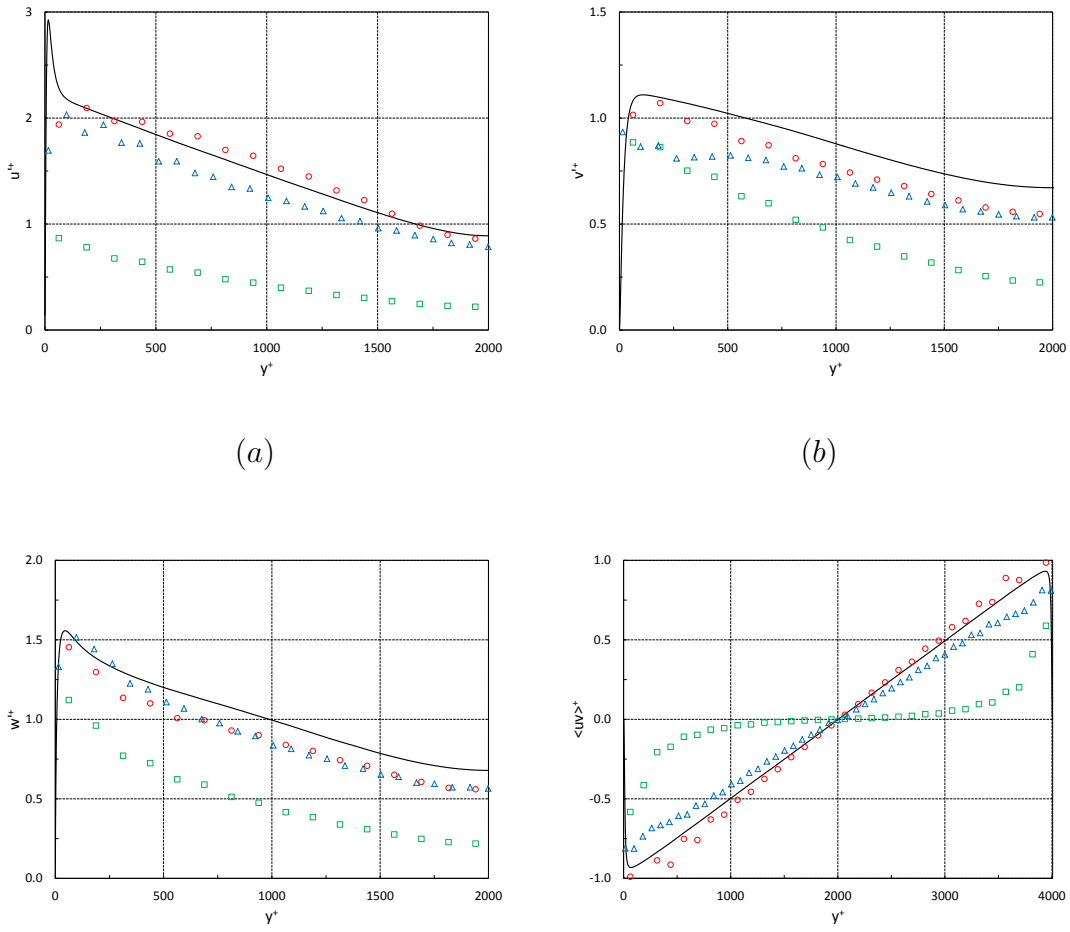

Figure 3.9: $M = 0.15$, $Re_\tau = 2003$ turbulent statistics using the compressible wall model, compared with the LES of Chung and Pullin [1] and the incompressible DNS of Hoyas and Jiménez [9]: (a) streamwise intensity; (b) wall-normal intensity; (c) spanwise intensity; (d) Reynolds shear stress (∘ total, □ subgrid, △ Chung and Pullin, — DNS)

Fig. 3.10 shows the mean turbulence kinetic energy profile predicted by the simulation for $Re_\tau = 2003$ with the new wall model, and Fig. 3.11 shows the mean rates of production and dissipation of k; as expected, most production and dissipation occurs near the walls [3], and most of the dissipation occurs at subgrid scales. All results match the DNS quite successfully.

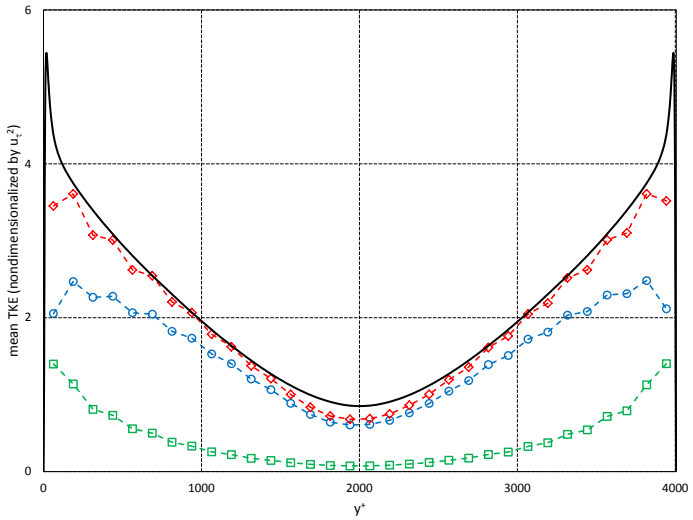

Figure 3.10: $M = 0.15$, $Re_\tau = 2003$ mean turbulence kinetic energy profile using the compressible wall model, compared with the incompressible DNS results of Hoyas and Jiménez [9] ($\circ$ resolved, $\square$ subgrid, $\diamond$ total, — DNS)

The results of the simulations at $Re_\tau = 2003$, 2×10^4, 2×10^5 and 2×10^6 are shown in Fig. 3.12, Fig. 3.13, and Fig. 3.14. All four mean velocity profiles lie closely atop the log law ($\kappa = 0.4$, $B = 5.0$); the turbulent intensities and Reynolds shear stress profiles display spreads similar to those seen in the incompressible results of Chung and Pullin [1], with profile shapes as expected. Several of the results show the near-wall spatial oscillations also observed in [21] and [1], concluded by Chung and Pullin to be Gibbs oscillations resulting from the no-penetration boundary con-

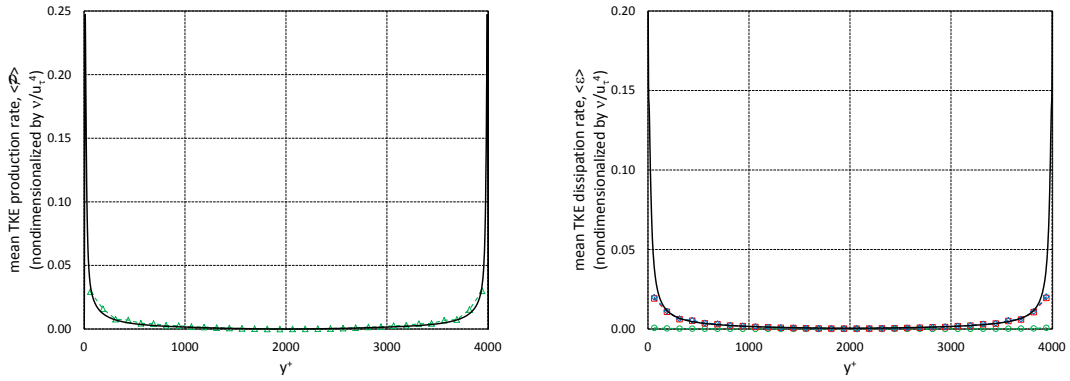

(a) (b)

Figure 3.11: $M = 0.15$, $Re_\tau = 2003$ mean rates of (a) production and (b) dissipation of turbulence kinetic energy using the compressible wall model, compared with the incompressible DNS results of Hoyas and Jiménez [9] ($\triangle$ production, $\circ$ resolved dissipation, $\square$ subgrid dissipation, $\diamond$ total dissipation, — DNS)

dition [1]. It is also observed, as in [1], that the expected (slight) increase in the u' peak with increasing Reynolds number is not captured, due to the integration of the momentum equation across the near-wall layer performed during the development of the compressible wall model. The approximate "step change" in the percentage of resolved turbulence kinetic energy, $k_{resolved}/k$, from $Re_\tau = 2003$ to the higher friction Reynolds numbers (see Table 3.1) is curious; certainly, though, as the y^+ value of the first grid point (from which the wall model receives input from the LES) increases with Reynolds number, the bottom-top symmetry and "smoothness" of the k profiles degrades, likely impacting the overall accuracy of the simulation. In addition, the increasing importance of the subgrid-scale model at higher Reynolds numbers requires significantly more of the turbulence kinetic energy to be predicted via modeling versus simulation. Finally, it is noted that k is here the total turbulence kinetic energy of the LES, which is itself only an estimate of the true k (i.e., as would be computed by

a direct numerical simulation), and $k_{resolved}/k$ reported here is therefore a somewhat rough approximation.

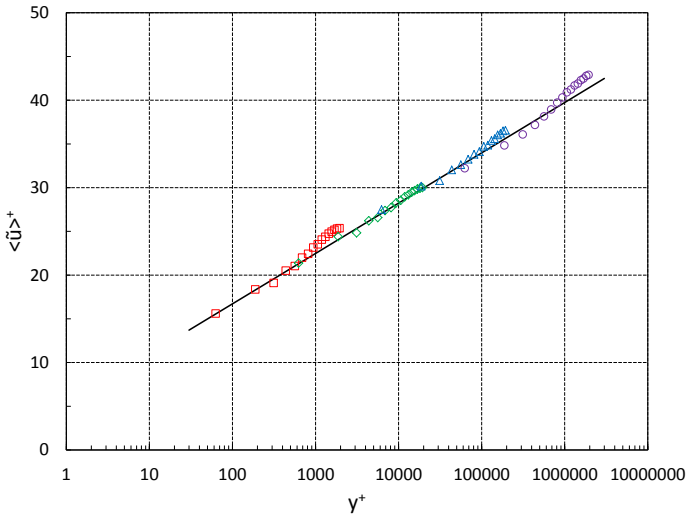

Figure 3.12: $M = 0.15$ mean velocity profiles using the compressible wall model ($\square$ $Re_\tau = 2003$, $\diamond$ $Re_\tau = 2 \times 10^4$, $\triangle$ $Re_\tau = 2 \times 10^5$, $\circ$ $Re_\tau = 2 \times 10^6$, — log law, $\kappa = 0.4$, $B = 5$)

The favorable comparisons to the DNS of these low-Mach number results, over a range of Reynolds numbers on a fixed-resolution, coarse mesh, serve to partially validate the new, compressible wall model. The strict mesh resolution requirements of large-eddy simulation with near-wall resolution (LES-NWR) have been avoided through use of this new model.

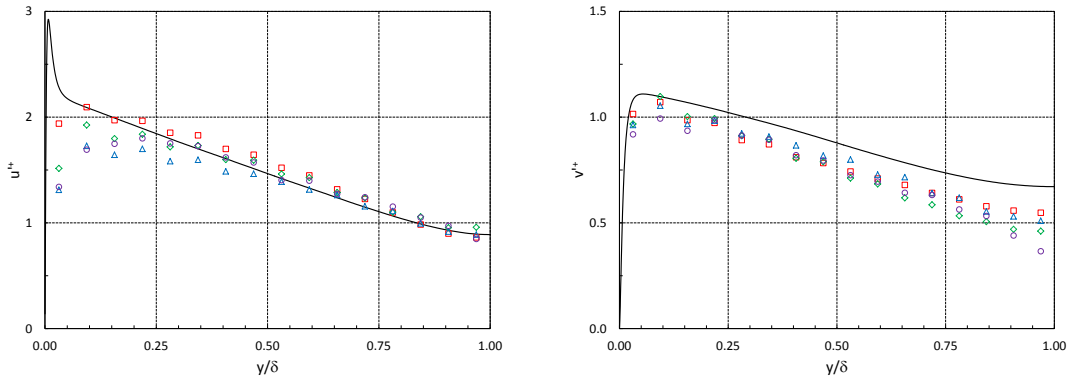

(a) (b)

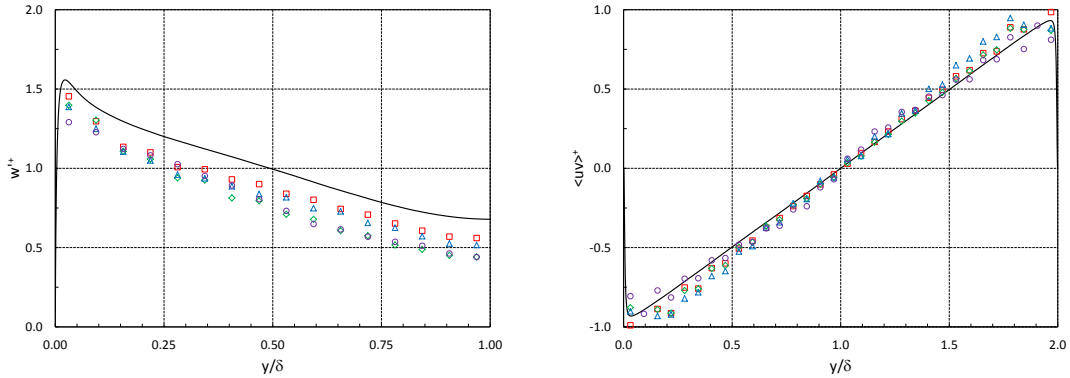

(c) (d)

Figure 3.13: $M = 0.15$ turbulent statistics using the compressible wall model: (a) streamwise intensity; (b) wall-normal intensity; (c) spanwise intensity; (d) Reynolds shear stress ($\square$ $Re_\tau = 2003$, $\diamond$ $Re_\tau = 2 \times 10^4$, $\triangle$ $Re_\tau = 2 \times 10^5$, $\circ$ $Re_\tau = 2 \times 10^6$, — incompressible DNS $Re_\tau = 2003$ [9])

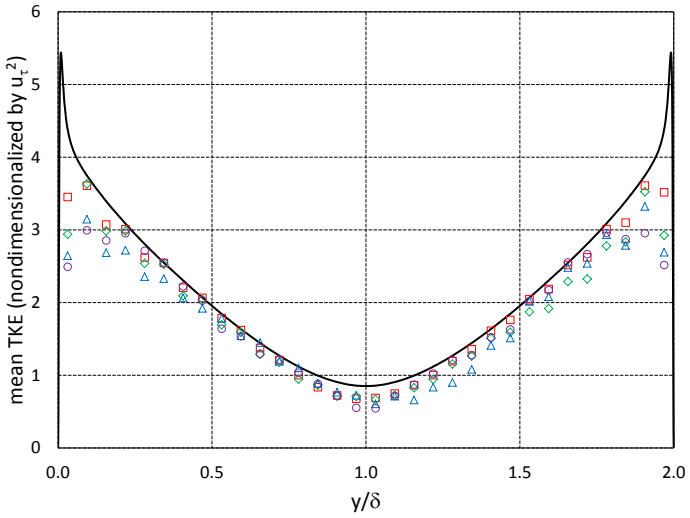

Figure 3.14: $M = 0.15$ mean turbulence kinetic energy profiles using the compressible wall model ($\square$ $Re_\tau = 2003$, $\diamond$ $Re_\tau = 2 \times 10^4$, $\triangle$ $Re_\tau = 2 \times 10^5$, $\circ$ $Re_\tau = 2 \times 10^6$, — incompressible DNS $Re_\tau = 2003$ [9])

3.4 LES of Compressible Channel Flow at M = 0.7 Using the New Wall Model

Large-eddy simulations with near-wall modeling (LES-NWM) of incompressible or low-Mach number flows have been successfully performed by others, as in [1], [21] and [39]. Conversely, LES-NWM of compressible flows have apparently not been attempted previously. LES of $M = 0.7$ turbulent channel flows were here performed over a three-order-of-magnitude range of friction Reynolds numbers on the same $256 \times 32 \times 128$-cell mesh used for $M = 0.15$ simulations. Results at $Re_\tau = 186$ were compared with the direct simulation of Wei and Pollard [37]. Run parameters for the four $M = 0.7$ simulations are summarized in Table 3.2.

Table 3.2: Run parameters of the $M = 0.7$ LES

Re_τ	δ (m)	u_τ (m/s)	y_1^+	T_w (K)	p_{init} (kPa)	$k_{resolved}/k$
186	0.0002	13.13	5.8	217	76	93%
2×10^3	0.003	9.41	62.5	213	75	74%
2×10^4	0.036	7.85	625	237	83	55%
2×10^5	0.42	6.72	6250	256	90	58%

Development of the compressible wall model made use of the observation in [32] that, in the mean, compressible flows (up to $M = 3.0$) are essentially isobaric, and that the magnitude of pressure fluctuations is much smaller than the mean. Fig. 3.15 plots mean pressure and pressure fluctuation profiles (non-dimensionalized by the pressure initial condition) at $M = 0.7$, $Re_\tau = 186$, confirming the validity of these assumptions.

The compressible wall model and isothermal-wall boundary condition implementation successfully control temperatures in the channel, removing heat through the

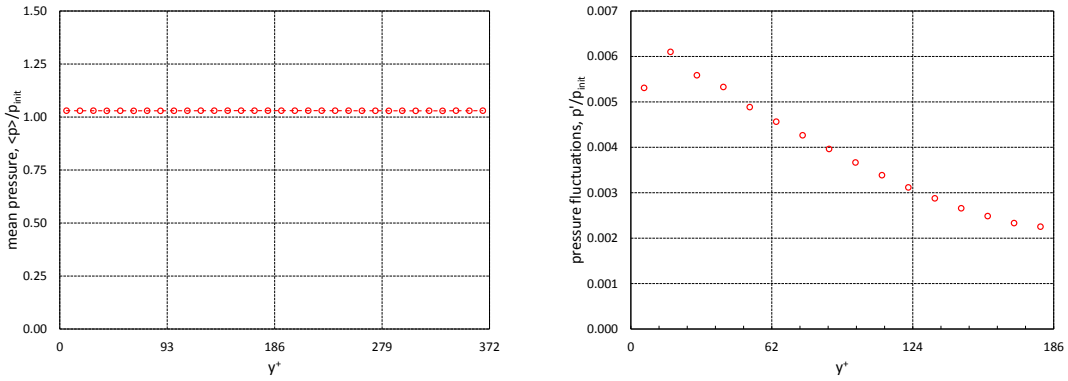

(a) (b)

Figure 3.15: (a) Mean pressure and (b) pressure fluctuation profiles of the LES at $M = 0.7$, $Re_\tau = 186$

walls to prevent a temperature rise over time. In Fig. 3.16, the time histories of temperature at one bottom wall-adjacent grid point and one top wall-adjacent point are shown. After an initial startup transient, temperatures at these two near-wall locations are seen to fluctuate about a constant value some 2% higher than T_w. For compressible flows with isothermal walls, the mean temperature is everywhere higher than the wall temperature, so this result is as expected.

In Fig. 3.17, the mean velocity profile of the $Re_\tau = 186$ simulation is compared to the DNS of Wei and Pollard [37, 40]. The match to the DNS is reasonable, with the velocity about 3% too slow in the log layer. This is due, at least in part, to the *a priori* prediction of bulk velocity, used to set the isothermal T_w boundary condition; the $\bar{U}$ prediction from applying the Van Driest transformation to the incompressible log law (see section 2.4.2) is about 7% lower than the steady-state bulk velocity of the DNS, and so there is some error in the T_w specification.

The $\langle \tilde{u} \rangle$ match at the first grid point, however, is poor. This is due to the use of the wall shear stress (τ_w) boundary condition discussed briefly in section 2.4.2, and

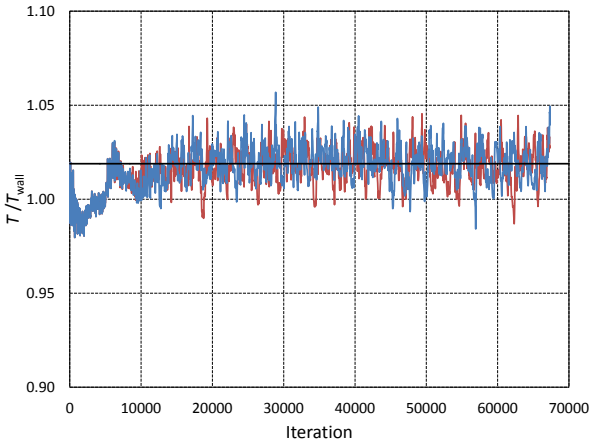

Figure 3.16: Temperature histories over 40 flow-throughs: one bottom wall-adjacent cell (red) and one top wall-adjacent cell (blue), $M = 0.7$, $Re_\tau = 186$, isothermal wall boundary condition

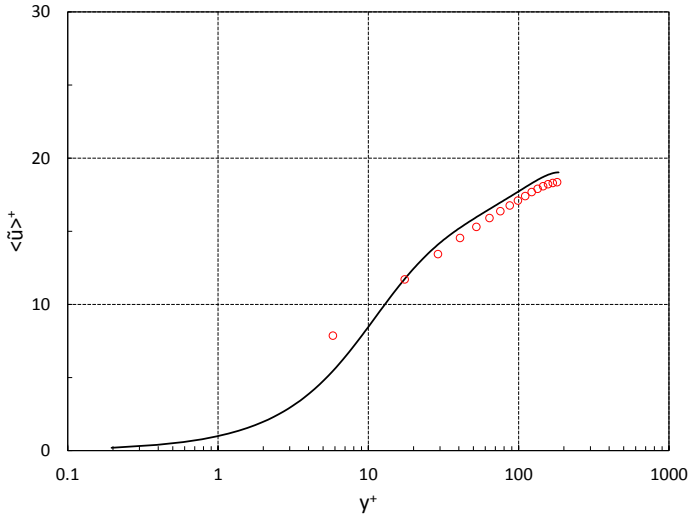

Figure 3.17: $M = 0.7$, $Re_\tau = 186$ mean velocity profile using the compressible wall model (∘), compared with the DNS results of Wei and Pollard, 2011 [37] (—)

described in detail in Pantano et al., 2008 [21]. The development of this boundary condition assumes the near-wall flow features are confined to a thin sublayer of the first computational cell; at a low $Re_\tau = 186$, the first grid point is at $y^+ = 5.8$—i.e., nearly inside the viscous sublayer—and so this assumption fails. Refining the grid would not improve the $\langle \tilde{u} \rangle$ calculation at the first point; only selection of an alternative τ_w BC would address this shortcoming. For the higher Reynolds numbers simulated, this boundary condition was seen to work well. As before, the prediction can be claimed successful considering the use of only 32 uniformly spaced points across the height of the channel, compared to the 286 points (with clustering) used in the DNS.

Fig. 3.18 plots the mean Mach number, streamwise turbulent intensity, Reynolds shear stress, and turbulence kinetic energy profiles, and Fig. 3.19 plots the mean pressure, density and temperature profiles, of the $M = 0.7$, $Re_\tau = 186$ LES for comparison with the DNS. (The unpublished u', $\langle uv \rangle$ and k DNS results were provided by the authors of that study [40].) The LES results compare well with the DNS (the poor $\langle \rho \rangle$ and $\langle T \rangle$ matches at the first grid point due, again, to the use of the τ_w boundary condition at this low Reynolds number). The new wall model is thus successfully validated for subsonic, compressible, fully developed turbulent channel flow simulations.

Simulations were then performed at $M = 0.7$, $Re_\tau = 2 \times 10^3$, 2×10^4 and 2×10^5; results are plotted in Fig. 3.20. Again, the profile shapes are correct; the expected mild increase in peak u' is not seen, due to the near-wall integration performed by the wall model. The $\langle uv \rangle$ peak moves closer to the wall with increasing Reynolds number. The near-wall, spatial Gibbs oscillations become somewhat more pronounced with increasing Re_τ, as more of the turbulence kinetic energy is modeled rather than resolved. In sum, the performance of the LES and the wall model is quite remarkable for such a coarse, fixed grid over this large range of Reynolds numbers.

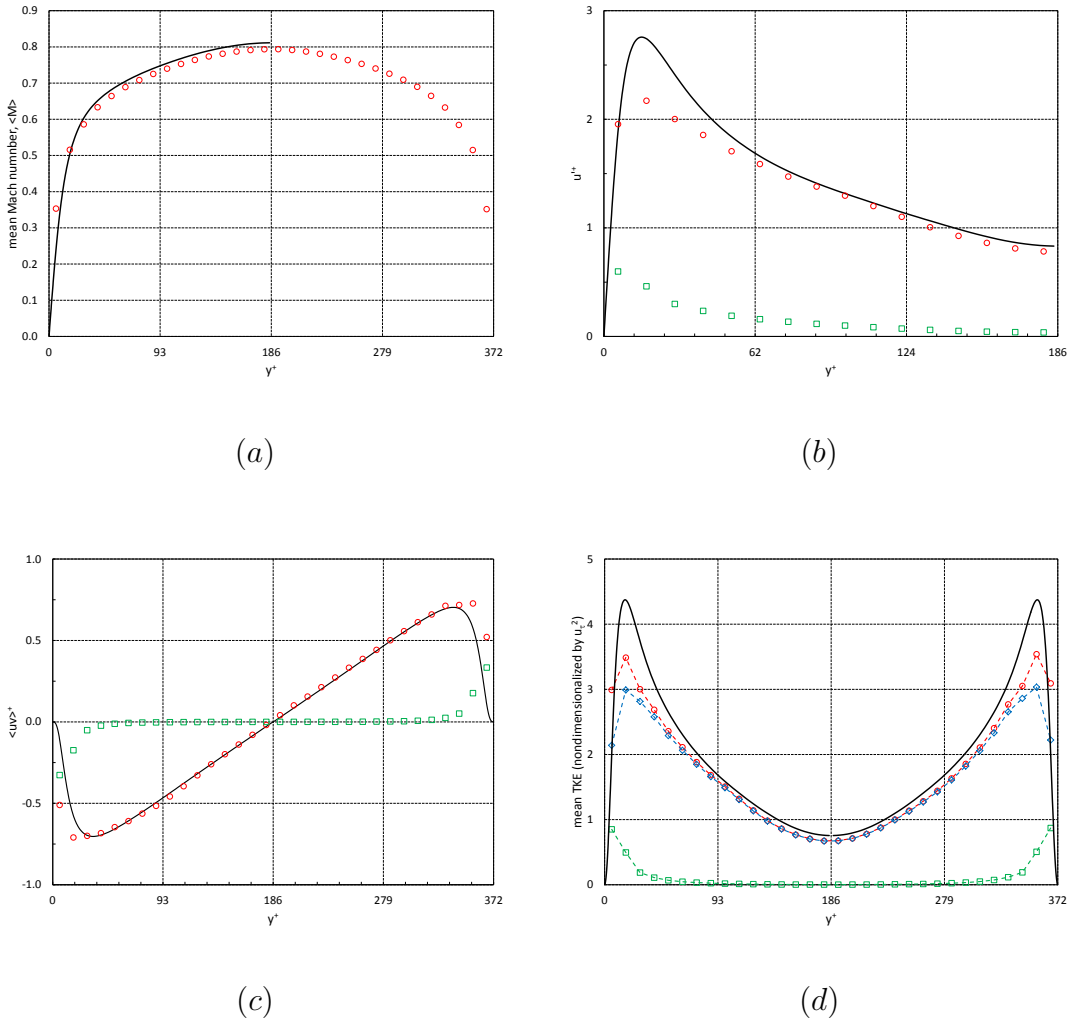

(a) (b)

(c) (d)

Figure 3.18: $M = 0.7$, $Re_\tau = 186$ turbulent statistics using the compressible wall model, compared with the DNS results of Wei and Pollard, 2011 [37]: (a) mean Mach number (∘ LES, — DNS); (b) streamwise turbulent intensity (∘ total, □ subgrid, — DNS); (c) Reynolds shear stress (∘ total, □ subgrid, — DNS); (d) turbulence kinetic energy (◇ resolved, □ subgrid, ∘ total, — DNS)

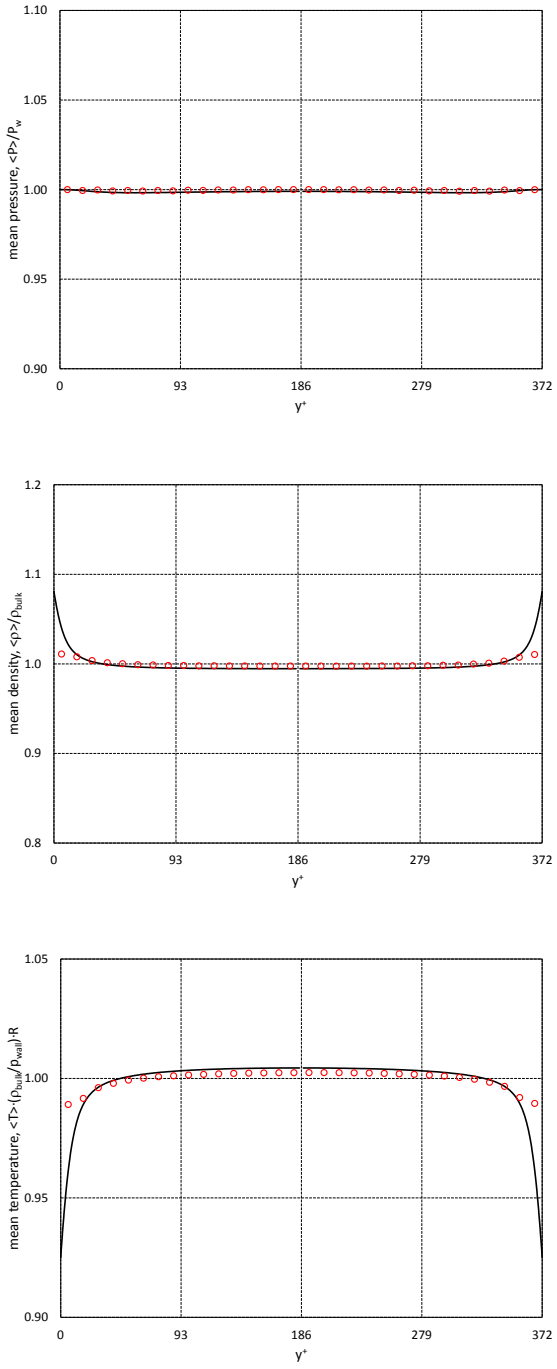

Figure 3.19: $M = 0.7$, $Re_\tau = 186$ mean profiles of pressure (top), density (middle) and temperature (bottom), LES using the compressible wall model ($\circ$) compared with the DNS results of Wei and Pollard, 2011 [37] (—)

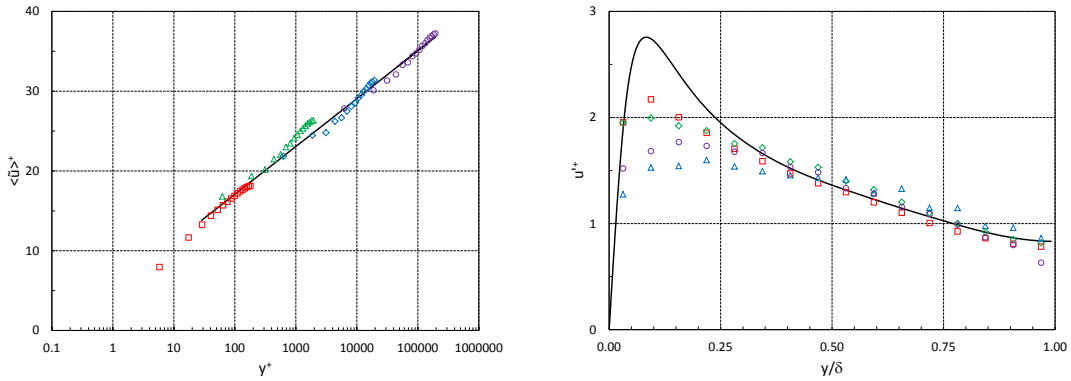

(a) (b)

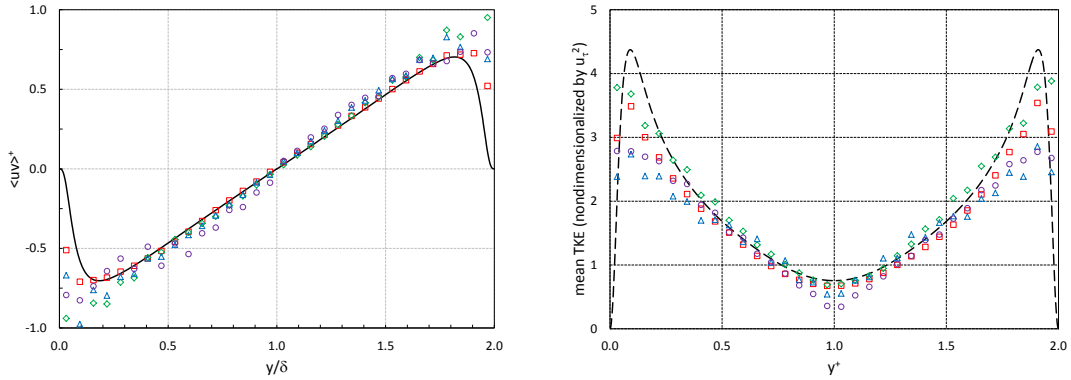

(c) (d)

Figure 3.20: $M = 0.7$ turbulent statistics using the compressible wall model: (a) mean velocity profiles; (b) streamwise turbulent intensity; (c) Reynolds shear stress; (d) turbulence kinetic energy ($\square$ $Re_\tau = 186$, $\diamond$ $Re_\tau = 2 \times 10^3$, $\triangle$ $Re_\tau = 2 \times 10^4$, $\circ$ $Re_\tau = 2 \times 10^5$, — compressible log law, - - - DNS $Re_\tau = 186$ [37])

Chapter 4

CONCLUSIONS AND RECOMMENDATIONS FOR FUTURE RESEARCH

4.1 Summary of Research

Continued advancements in both computational hardware development and numerical algorithms have combined to make large-eddy simulation (LES) an ever more promising and effective method for analyzing turbulent flows in practical engineering applications. LES significantly improves on Reynolds-averaged Navier-Stokes (RANS) methods by offering insight into the large-scale motions of turbulent eddies that is not available from RANS simulations, while avoiding the steep computational cost of resolving the wide range of turbulence scales—especially at the high Reynolds numbers of practical interest—imposed by direct numerical simulation (DNS). By resolving only the large, energy-containing scales of turbulence and applying a universal model to account for subgrid-scale effects, LES can efficiently simulate the most important turbulent phenomena [3]. For these reasons, LES is an active field of research in the field of modern computational fluid mechanics.

Unfortunately, the fundamental assumption of LES—that only large-scale turbulence, which contains the majority of the turbulence kinetic energy of the flow and is responsible for most of the convection of mass and momentum, is affected by flow geometry, while small-scale turbulence is essentially universal and can be modeled effectively—fails near the surface of a wall-bounded flow. In such flows, there are no "large eddies" in the near-wall region, and small turbulence scales carry the turbulence kinetic energy and are responsible for mass and momentum transfer [18]. To then use a near-wall computational mesh fine enough to resolve most of the turbu-

lence kinetic energy is nearly as computationally expensive as DNS: mesh size would increase as $Re^{13/7}$ at high Reynolds numbers [8].

To preserve the computational advantage of LES, then, the Reynolds number-dependent near-wall mesh refinement requirement must be avoided. If an effective wall model can be employed that takes as inputs the flowfield parameters of the running simulation to accurately model the near-wall physics, it may be possible to use LES meshes with size only weakly dependent on, or even independent of, Reynolds number. This is the goal of large-eddy simulation with near-wall modeling (LES-NWM).

Recent large-eddy simulations by Pantano et al. [21], Chung and Pullin [1], and others show that the promise of LES-NWM has been essentially realized for incompressible flows at friction Reynolds numbers of $O(10^6)$ or higher. The challenge addressed in the present research is to extend this progress into the compressible flow regime, where to date, no LES-NWM has been reported, with all previous simulations relying on computationally expensive grid-point clustering in order to resolve nearly fully the near-wall turbulence.

This challenge has been here addressed via the development of a novel, parameter-free wall model for the LES of compressible, isothermal-wall channel flows, which was inspired by the incompressible model of Chung and Pullin [1]. In this model, ordinary differential equations (ODEs) are obtained by integrating the LES momentum and internal energy equations in the wall-normal direction from the wall to the first grid point in the log layer, avoiding the need to resolve the steep near-wall gradients; these ODEs compute the local, instantaneous wall shear stress and heat flux, which are then applied as wall boundary conditions. The subgrid-scale (sgs) stresses and heat fluxes in the wall model ODEs are provided by the stretched-vortex sgs model developed by Kosović, Pullin and Samtaney [26] based on the fine turbulence model of Lundgren [2]. The wall model does not rely on any empirically derived, "tunable" parameters, such as a von Kármán constant, and thus need not be "dialed in" before use.

This research program compared the incompressible wall models of Pantano et al. [21] and Chung and Pullin [1] and the present compressible wall model with the incompressible DNS of Hoyas and Jiménez at $Re_\tau = 2003$ [9]. On a fixed, coarse $256 \times 32 \times 128$-cell mesh, LES employing the present wall model matched the DNS results well, and simulations at friction Reynolds numbers up to $Re_\tau = 2 \times 10^6$ were performed succesfully.

The wall model was then applied to LES of compressible channels at $M = 0.7$ and $Re_\tau = 186$, on the same coarse grid, with results compared to the DNS of Wei and Pollard [37, 40]. The wall model successfully prevented heating of the channel over time by removing excess heat through the isothermal walls. Such turbulent flowfield paramters as the mean velocity and local Mach number profiles, the streamwise turbulent intensity, the Reynolds shear stress, and the mean turbulence kinetic energy profile compared well to the DNS results. Simulations were then performed at Reynolds numbers up to $Re_\tau = 2 \times 10^5$ and, considering the large grid point spacing used, the results were quite satisfactory.

4.2 Recommendations

Large-eddy simulation (LES) research today generally focuses on improving the ability to simulate accurately ever higher Reynolds number flows. However, such efforts must not neglect potential low-Re applications of new methodologies. In the present research, the local, instantaneous wall shear stress τ_w, predicted by the selected wall model, was applied as a momentum boundary condition (BC) at the wall. The assumptions made to apply this BC do not hold at very low friction Reynolds numbers, such as the $Re_\tau = 186$ condition simulated here; the result was a poor prediction of the mean velocity $\langle \tilde{u} \rangle$ at the first grid point. To allow more general application of this or any wall model at low Reynolds numbers, a different τ_w BC implementation would need to be employed.

Although the present compressible wall model performed admirably on a fixed,

coarse $256 \times 32 \times 128$-cell mesh over a wide range of Reynolds numbers, the fact is that mild near-wall clustering of grid points might have improved the quality of the high-Re results (e.g., reducing spatial oscillations, capturing the rise in the u' peak with Reynolds number) by increasing the percentage of turbulence kinetic energy resolved in the near-wall region. In fact, the wall-modeling recommendation of Kawai and Larsson is to fix the height above the wall from which flow properties feed the wall model, and then to refine the near-wall grid until errors are reduced at the first few grid points [38]. AMROC's requirement to use uniform grid spacing prevents evaluation of the potential effectiveness of mild near-wall grid refinement with the new wall model. Chung and Pullin, applying the incompressible wall model which inspired the new model reported here, successfully used long, wide cells—$\Delta x = \Delta z = 4\Delta y$—in their simulations; such an approach should also work with the present compressible wall model to allow use of more points across the channel height without incurring a significant computational cost. In other words, further evaluation of the compressible wall model in a flow solver permitting more flexibility in grid configuration would be insightful.

The compressible wall model was formulated for general compressible flows; applicability was not limited to subsonic flows, and use of the model in LES of supersonic flows is intended. In the present implementation, some early attempts at simulating $M = 1.5$ flows proved unsuccessful, with temperatures rising in the channel and bulk velocities decreasing steadily over time. It is likely that, as Mach number increases, inaccuracies in the initial bulk velocity prediction worsen, such that an incorrect isothermal wall temperature T_w is prescribed for the desired bulk Mach number and imposed (constant) mean streamwise pressure gradient. A better prediction of the steady-state bulk velocity—perhaps informed by the direct simulations of supersonic flows by Wei and Pollard [37], Coleman, Kim and Moser [32] and others—could be expected to provide a more accurate T_w boundary condition, feeding the θ_0 model and producing the correct heat flux through the walls and out of the channel to prevent

a temperature rise and allow convergence on the specified bulk Mach number.

Or more probably, since the mean pressure gradient required to drive a turbulent channel flow is not known *a priori* [3], implementation of an unsteady pressure gradient that varies in time to preserve a specified constant bulk velocity may be necessary. Such an approach is used, for example, in the direct and large-eddy simulations of Coleman, Kim and Moser [32], Salinas Vázquez and Métais [29], Lenormand, Sagaut and Ta Phuoc [27], and others. In these simulations, variations in the pressure gradient become small once the flow reaches statistically stationary conditions [32]. A similar implementation might be required to use the present wall model successfully in supersonic channel simulations.

Finally, there would be interest in using the compressible wall model to simulate not only fully developed internal flows, but also such external flows as the spatially developing turbulent boundary layer (SDTBL). SDTBL simulations generally apply an adiabatic-wall boundary condition, rather than the isothermal-wall condition used throughout the present research. Evaluation of some terms in the development of the θ_0 model made use of the fact that T_w is known for isothermal-wall channel flows; some minor implementation changes would be required to extrapolate temperatures from near-wall locations down to the adiabatic wall surface or to otherwise determine the local, instantaneous adiabatic wall temperature (and the corresponding wall viscosity μ_w) in order to apply the new wall model to SDTBL or other compressible flows with adiabatic walls.

The present parameter-free, compressible wall model has been successfully validated for large-eddy simulations of compressible channel flows, with grid-size independence from Reynolds number demonstrated. Implementation in a flow solver with better grid configuration flexibility could further improve its performance simulating high-Re flows. Applicability to LES of supersonic flows is intended, although changes to the specification of the isothermal wall temperature and/or the mean pressure gradient driving the flow in the channel would likely be necessary. Only minor im-

plementation changes would be required to apply the model to such external flows as the SDTBL with adiabatic walls.

BIBLIOGRAPHY

[1] D. Chung and D. I. Pullin, "Large-eddy simulation and wall modeling of turbulent channel flow," *Journal of Fluid Mechanics*, vol. 631, pp. 281–309, 2009.

[2] T. S. Lundgren, "Strained spiral vortex model for turbulent fine structure," *Physics of Fluids*, vol. 25, no. 12, pp. 2193–2203, 1982.

[3] S. B. Pope, *Turbulent Flows*. Cambridge: Cambridge University Press, 2000.

[4] L. F. Richardson, *Weather Prediction by Numerical Process*. London: Cambridge University Press, 1922.

[5] F. M. White, *Viscous Fluid Flow*. New York: McGraw-Hill, second ed., 1991.

[6] J. J. Bertin, *Aerodynamics for Engineers*. Upper Saddle River, NJ: Prentice Hall, fourth ed., 2002.

[7] D. R. Chapman, "Computational aerodynamics development and outlook," *AIAA Journal*, vol. 17, no. 12, pp. 1293–1313, 1979.

[8] H. Choi and P. Moin, "Grid-point requirements for large eddy simulation: Chapman's estimates revisited," *Physics of Fluids*, vol. 24, no. 1, 2012.

[9] S. Hoyas and J. Jiménez, "Scaling of the velocity fluctuations in turbulent channels up to $Re_\tau = 2003$," *Physics of Fluids*, vol. 18, no. 1, pp. 1–4, 2006.

[10] E. Tinoco, March 2013. Lecture to undergraduate students in aeronautics and astronautics at the University of Washington, Seattle.

[11] J. Smagorinsky, "General circulation experiments with the primitive equations," *Monthly Weather Review*, vol. 91, no. 3, pp. 99–164, 1963.

[12] J. W. Deardorff, "A numerical study of three-dimensional turbulent channel flow at large Reynolds numbers," *Journal of Fluid Mechanics*, vol. 41, no. 2, pp. 453–480, 1970.

[13] T. von Kármán, "Mechanische ahnlichkeit und turbulenz," in *Proceedings of the Third International Congress, Applied Mechanics*, pp. 85–105, 1930.

[14] P. Hill and C. Peterson, *Mechanics and Thermodynamics of Propulsion*. Reading, Massachusetts: Addison-Wesley, second ed., 1992.

[15] Y. Morinishi, S. Tamano, and K. Nakabayashi, "Direct numerical simulation of a compressible turbulent channel flow between adiabatic and isothermal walls," *Journal of Fluid Mechanics*, vol. 502, pp. 273–308, 2004.

[16] E. R. Van Driest, "Turbulent boundary layer in compressible fluids," *Journal of the Aeronautical Sciences*, vol. 18, no. 3, pp. 145–160 & 216, 1951.

[17] A. J. Smits and J.-P. Dussauge, *Turbulent Shear Layers in Supersonic Flow*. Woodbury, NY: AIP Press, 1996.

[18] S. B. Pope, "Ten questions concerning the large-eddy simulation of turbulent flows," *New Journal of Physics*, vol. 6, no. 35, pp. 1–24, 2004.

[19] A. Misra and D. I. Pullin, "A vortex-based subgrid stress model for large-eddy simulation," *Physics of Fluids*, vol. 9, no. 8, pp. 2443–2454, 1997.

[20] D. I. Pullin, "A vortex-based model for the subgrid flux of a passive scalar," *Physics of Fluids*, vol. 12, no. 9, pp. 2311–2319, 2000.

[21] C. Pantano, D. I. Pullin, P. E. Dimotakis, and G. Matheou, "LES approach for high Reynolds number wall-bounded flows with application to turbulent channel flow," *Journal of Computational Physics*, vol. 227, pp. 9271–9291, 2008.

[22] P. Moin, K. Squires, W. Cabot, and S. Lee, "A dynamic subgrid-scale model for compressible turbulence and scalar transport," *Physics of Fluids A*, vol. 3, no. 11, pp. 2746–2757, 1991.

[23] C. Hirsch, *Numerical Computation of Internal and External Flows*. Amsterdam: Elsevier, 2007.

[24] D. I. Pullin and P. G. Saffman, "Reynolds stresses and one-dimensional spectra for a vortex model of homogeneous anisotropic turbulence," *Physics of Fluids*, vol. 6, no. 5, pp. 1787–1796, 1994.

[25] T. Voelkl, D. I. Pullin, and D. C. Chan, "A physical-space version of the stretched-vortex subgrid-stress model for large-eddy simulation," *Physics of Fluids*, vol. 12, no. 7, pp. 1810–1825, 2000.

[26] B. Kosović, D. I. Pullin, and R. Samtaney, "Subgrid-scale modeling for large-eddy simulations of compressible turbulence," *Physics of Fluids*, vol. 14, no. 4, pp. 1511–1522, 2002.

[27] E. Lenormand, P. Sagaut, and L. Ta Phuoc, "Large eddy simulation of subsonic and supersonic channel flow at moderate Reynolds number," *International Journal for Numerical Methods in Fluids*, vol. 32, pp. 369–406, 2000.

[28] E. Lenormand, P. Sagaut, L. Ta Phuoc, and P. Comte, "Subgrid-scale models for large-eddy simulations of compressible wall bounded flows," *AIAA Journal*, vol. 38, pp. 1340–1350, 2000.

[29] M. Salinas Vázquez and O. Métais, "Large-eddy simulation of the turbulent flow through a heated square duct," *Journal of Fluid Mechanics*, vol. 453, pp. 201–238, 2002.

[30] C. Brun, M. P. Boiarciuc, M. Haberkorn, and P. Comte, "Large eddy simulation of compressible channel flow," *Theoretical and Computational Fluid Dynamics*, vol. 22, pp. 189–212, 2008.

[31] P. G. Huang, G. N. Coleman, and P. Bradshaw, "Compressible turbulent channel flows: DNS results and modelling," *Journal of Fluid Mechanics*, vol. 305, pp. 185–218, 1995.

[32] G. N. Coleman, J. Kim, and R. D. Moser, "A numerical study of turbulent supersonic isothermal-wall channel flow," *Journal of Fluid Mechanics*, vol. 305, pp. 159–183, 1995.

[33] K. Webster, September 2013. Personal communication.

[34] D. D. Knight, "AIAA paper 2006-498, Inflow boundary conditions for DNS and LES of compressible turbulent boundary layers," in *AIAA 44th Aerospace Sciences Meeting*, (Reno, NV), 2006.

[35] R. Deiterding, *Parallel adaptive simulation of multi-dimensional detonation structures*. PhD thesis, Brandenburgische Technische Universitat Cottbus, September 2003.

[36] R. Kamakoti and C. Pantano, "High-order narrow stencil finite-difference approximations of second-order derivatives involving variable coefficients," *SIAM Journal of Scientific Computing*, vol. 31, no. 6, pp. 4222–4243, 2009.

[37] L. Wei and A. Pollard, "Direct numerical simulation of compressible turbulent channel flows using the discontinuous Galerkin method," *Computers & Fluids*, vol. 47, pp. 85–100, 2011.

[38] S. Kawai and J. Larrson, "Wall-modeling in large eddy simulation: Length scales, grid resolution, and accuracy," *Physics of Fluids*, vol. 24, 015105, 2012.

[39] M. Inoue and D. I. Pullin, "Large-eddy simulation of the zero-pressure-gradient turbulent boundary layer up to $Re_\theta = O(10^{12})$," *Journal of Fluid Mechanics*, vol. 686, pp. 507–533, 2011.

[40] A. Pollard, September 2014. Personal communication.